Static equilibria and transient dynamics of rigid bodies with unilateral contacts

Péter L. Várkonyi

Dissertation for the Title Doctor of the Hungarian Academy of Sciences

October 2016

TABLE OF CONTENTS

CHAPTER 1:

INTRODUCTION

CLASSICAL mechanics is one of the oldest fields of natural sciences. Motivated by the goal of building man-made structures and machines, humans tried to understand the interaction of solid objects via contact forces; to understand gravitational effects; to explain how certain objects move and why others stay in rest, and whether or not they collapse under certain loads.

For long time, our knowledge in the field of mechanics was dominated by experimental evidence as well as by qualitative models and theories. Nevertheless philosophers and scientists of the ancient Greek culture were already surprisingly successful in creating mathematical models of physical phenomena. To mention two examples, Archimedes set up the laws of flotation, and he also combined this with his rich knowledge of geometry to determine asymmetric equilibria of a rotational paraboloid floating in a liquid – a problem that appears to our eyes hardly solvable without the concept of integrals. Another example is how Aristotle proposed a plausible semi-quantitative mathematical model explaining the rounded shapes of pebbles: using the kinematics of rotational motion as a basis, he argued that points of a pebble being far from its center exhibit more intensive impacts, resulting in fast erosion and thus round-off of the overall shape.

The birth of modern physics is most often associated with Newton's laws of motion, and Newton's famous theory lead to a quick development of rigid body dynamics in the 18th century, and to the dynamics of deformable solids in the 18th-20th centuries.

Today, the classical theory of rigid bodies appears to be completely understood and no more subject to intensive research efforts. The present thesis addresses the "old-fashioned" topic of static equilibrium of rigid objects. Together with the authors of the paper [49] the reader may ask the question: *"Static equilibria of rigid bodies: is there anything new?"* Of course, this thesis will give an affirmative answer. Despite the fact that the laws of equilibrium have been established for centuries, interesting problems arise, when mechanical behavior becomes strongly dependent on other mathematical properties of a system, or if questions about static equilibrium require the analysis of more complex physical phenomena, such as the dynamics of the system. These two types of problems will be the subject of the subsequent two chapters.

In Chapter 2, we investigate examples of the interplay between geometry and statics. As we will show, the static equilibria of a rigid body on a horizontal surface can be found easily by examination of the associated distance function r, which will be defined formally in the sequel. The distance function represents the distance of each boundary point from the *center of mass*. We will focus on objects made of homogenous material, for which the shape of the object determines the position of the center of mass uniquely. Thus, a naively chosen function will typically not correspond to a real physical object. The geometric constraint outlined above is at the root of the questions discussed in Section 2.2-4, and a related geometric constraint emerges in Sec. 2.5. We will ask questions like:

- How many equilibria do solids made of homogeneous material may have in theory?
- How can we influence the number of equilibria by modifying the shape of the object or the shape of the underlying support surface?
- Does natural selection prefer some of these shapes over others in the case of hard-shelled animals?

The research efforts of the author in this field were initiated by [49] who proved a nontrivial lower bound of the number of equilibria in the case of 2-dimensional objects on a horizontal support. Further inspiration came from the Russian mathematician V. I. Arnold, who asked if an analogous lower bound exists in three dimensions [50]; and by the Polish mathematician S. Ulam (most famous for his pivotal role in the development of the thermonuclear weapon) who asked 80 years ago a puzzling question about objects floating on the horizontal surface of a liquid: *are spheres the only shapes, which can float in equilibrium in any orientation?* In Chapter 2 we answer Arnold's question together with several generalizations and some related problems. We investigate the equilibria of objects resting on a horizontal surface; or inside a hollow sphere, as well as of ones floating in a liquid. Among others, we also find an affirmative answer to Ulam's question for a specific value of the liquid's density.

Arnold's and Ulam's original questions were motivated by mathematicians' curiosity, but the results of the thesis are complemented by several applications. The answer to Arnold's question is expanded into a classification of object shapes based on the number of equilibria, and we explore the preferences of natural selection, by discussing the morphology of turtle shells and their relations to self-righting behavior of the animals. Another application in geology is also reviewed briefly. Our results related to the number of static equilibria of

objects in a sphere are also discussed from the viewpoint of potential applications in the field of manufacturing automation.

The methodology of Chapter 2 remains mostly geometric. It does not require the understanding of physical laws governing the behavior of mechanical systems except for the laws of equilibrium. More involved physical problems are addressed in Chapter 3, where we identify intriguing problems related to the dynamics of a system in the neighborhood of an equilibrium state and/or before reaching an equilibrium. The primary aim of Chapter 3 is to explore the stability and the attractivity of equilibria using different definitions and methodologies. We ask questions like:

- How do systems reach an equilibrium state?
- If they rest in equilibrium, how do they respond to various types of perturbations?

Both questions are inspired by engineering applications.

Similarly to statics, the laws of motion have been established long ago by people like Newton and Euler. The actuality of this topic is given by the fact that static equilibria under gravity require contact, and contact-related phenomena such as impacts and friction give rise to many open questions.

The emerging difficulties are twofold. The first difficulty is the lack of reliable models due to the complexity of the underlying physical processes: for example an impact is a phenomenological description of a multi-scale dynamical process including shock waves, vibrations and viscoelastic material response. This tough situation is nicely illustrated by the fact the most popular simple impact law (based on kinematic coefficients of restitution) was developed by Newton, but the failure of his model to predict the outcome of any impact based on a limited number of measurements, and its apparent

inconsistency with energy conservation in certain situations (oblique impact with friction) still inspires researchers to develop newer and newer impact models [31] [37]. Modeling dry friction also has a rich history and it suffers from the same difficulties. Basic laws of friction were documentedly explored by Leonardo da Vinci; the most popular model by Amontons and Coulomb was developed in the 18th century, and improved friction models are still being developed [13] [81]. Even worse than unreliability, it has been known since the 19th century [92] [129] that the combination of rigid body theory with friction models tends to generate self-inconsistency or indeterminate answers even in simple situations [36]. It has become an established view that a "breakthrough" in modeling friction and impact modeling, i.e. finding a simple yet accurate model, or a complete and self-consistent theory within the framework of rigid body theory are hopeless [152].

The second difficulty of understanding contact-related phenomena is complexity: even idealized models of impact and friction turn our dynamic models into non-smooth, hybrid dynamical systems, which are subject to intensive research and do not have a complete theory at this time [16].

In the first part of Chapter 3, we study the transient behavior of objects before they come to rest in equilibrium: we seek to predict the probability distribution of the final resting aspects of objects after they have been dropped onto a horizontal surface. This question has been investigated mostly because of its role in the development of efficient part feeders (i.e. those machines which process a flow of unordered parts of identical shape and size at the entrance of an automated assembly line) [26]. In this part of the thesis, the difficulties of complexity and physical modeling are avoided by using a phenomenological model of the motion and by arguing that the results derived from the model are robust against the applied

simplifications. Nevertheless, the predictions of the phenomenological model are verified against computer simulation, which requires the modeling of many aspects of contact dynamics.

In the second part of Chapter 3, we investigate objects which have already reached a static equilibrium. The local stability of the equilibria is studied according to two distinct definitions. The results of the stability analysis fit into and extend a large body of work in robotics, where numerous notions of stability have been developed, see e.g. [89] [131]. As we will point out, traditional methods of the robotics community often do not comply with dynamical systems theory, which gives us space for improvement. Our theoretical results are motivated by simple applications in robotic grasping and locomotion.

This part of the thesis attempts to overcome the difficulties of contact mechanics discussed above. The complexity of contact motion is addressed by using Lyapunov-type approaches, which are not sensitive to fine details of the dynamics. The limitations and paradoxes of the rigid body approach are tackled by considering the quasi-rigid limit of compliant models. The unreliability of friction and impact model remains a partially unsolved issue. Nevertheless, we make as few assumptions about friction and impacts as possible, to maximize the significance of the results.

The research work summarized in this thesis was conducted between 2005 and 2015. Some results have been improved or used by others since then. The last parts of most sections contain brief summaries of ongoing related works by the author (mostly unpublished or under review) and by others.

In order to improve the readability of the thesis, some technical details are presented in appendices (Chapter 5).

Some results of the thesis have been developed in collaboration with others. These include the work reported in Section

2.2-3 (with Gábor Domokos) and in Sec. 3.4 (with David Gontier and Joel W. Burdick). The main text is everywhere written in first person plural without distinction between independent work of the author and joint work. Nevertheless, the principal results of the thesis at the end of Chapter 4 have been stated in singular or plural in accordance with the number of contributors.

CHAPTER 2:

STATIC EQUILIBRIA OF RIGID BODIES: THE INTERPLAY BETWEEN GEOMETRY AND MECHANICS

S TATIC equilibria of rigid bodies have always played a role in the technical development of humanity. In particular, determining the number of stable equilibria of an object on a flat horizontal surface becomes important in countless situations. Archimedes provided the first rigorous method to construct ships with *one* stable equilibrium [123], and the development of "monostatic" shapes has become a common approach to avoid the unexpected toppling of tools in various fields from sailing to robotics and astronautics. Throwing dice for making decisions as in gambling relies on the existence of *several,* stable equilibria with disjoint basins of attraction. While classical (cubic) dice have 6 stable equilibria, an astonishing diversity of other dice exists as well: dice with 2, 3, 4, 6, 8, 10, 12, 16, 20, 24, 30 and 100 stable equilibria appear in various games [190]. The invention of the wheel was essentially equivalent to the realization that a continuum of equilibria can exist. Modifying the number and the stability of equilibria such as stabilizing unstable equilibria is also a classical problem, ever since Christopher Columbus balanced his famous egg.

Chapter 2 addresses a family of mathematical problems related to the static equilibria of rigid bodies, in which the main challenges are geometric by nature, and the necessary ingredients of physical modeling remain very sparse and simple. Nevertheless, being mathematical is not the equivalent of being purely theoretical, as some of these problems have straightforward biological and engineering applications, also discussed here.

The first part of the chapter deals with methods and possibilities of constructing objects with a minimum number of stable and/or unstable equilibria. After introducing some basic concepts, and a classification scheme of objects based on the number of equilibria in Sec. 2.1, we discuss a mathematical problem coined by the recently deceased eminent Russian scientist Vladimir I. Arnold about the minimum number of equilibria of a convex, homogeneous rigid body on a horizontal, flat plane. We prove that this number is as low as 2, and also point out that shapes with only 2 equilibria appear to be extremely rare in our physical environment. We are inspired primarily by our curiosity to uncover how and to what extent the difficulty of achieving shapes with low number of equilibria is overridden by evolutionary selection. To this end, we investigate the shell shapes of turtles and tortoises. The idealized model of a parametric rigid body is fitted to the shells, and we show how the equilibrium classes of turtle models relate to the lifestyles and self-righting strategies of real animals.

We then examine a different approach of achieving monostatic behavior: instead of varying object shapes, we seek to find a geometric environment in which a given object becomes monostatic. In particular we investigate the number of equilibria of an

object enclosed in a frictionless sphere of given radius α. This problem is a natural generalization of the original one, given that the α→∞ limit of a spherical surface is a flat plane. We point out why monostatic behavior becomes more common in this environment, and outline a potential application of our new findings in the field of automated manufacturing.

Chapter 2 is closed by another mathematical generalization of our first problem: identifying the equilibria of rigid bodies floating on the surface of a liquid. Clearly, floating is a more complex phenomenon than resting on a rigid surface, in which the mean density ρ of the object relative to the liquid appears as an extra parameter. Nevertheless the two problems become identical in the limits of ρ→0 (where the object rests on top of the liquid surface without dipping into it) and ρ→1 (in which the object touches the liquid surface from below without rising above it). We address a question proposed by the Polish scientist Stanislav Ulam, which appears to be the exact opposite of Arnold's problem: are there objects other than spheres, for which all attitudes correspond to static equilibrium? Interestingly, this problem remained unsolved for over 70 years, despite being published in the *Scottish Book* [106], a widely known collection of mathematical problems with a long and intriguing history. By investigating the case of ρ=1/2, we give an affirmative answer with an exact proof for the first time.

2.1 BASIC CONCEPTS

2.1.1 Characterizing the state of a rigid body

The behavior of a dynamical system is usually characterized by its time-dependent *state*, which contains all necessary information about the system. For mechanical systems, such as a collection of moving rigid bodies, the state consists of the positions and velocities the components of the system, and it is usually represented by a set of (generalized) position coordinates and their time derivatives (generalized velocities). *State space* is the space spanned by these variables, in which each point corresponds to a state of the system. The investigation of equilibria is often possible without considering generalized velocities at all. The subspace of state space spanned by generalized coordinates is usually called *configuration space*. Each point of configuration space corresponds to a configuration of the system, i.e. it determines where the individual components of the system are located in physical space. It may seem plausible that the notion of "static equilibria" in the title of Chapter 2 refers to *configurations* corresponding to static equilibrium. Nevertheless, if one investigates equilibria of planar or spatial objects on a horizontal support surface (line in 2D or plane in 3D), the translational symmetry of the support surface implies that configurations of equilibrium are not isolated, and thus they are never finite in number. It is often convenient to treat the continuous sets of configurations induced by all translations as equivalent, which motivates

Definition 2.1.1*: an orientation of a rigid object is the set of configurations generated from one single configuration by all possible translations.*

In other words, orientation determines the attitude of the body, but it does not determine the location of its center of mass in physical space. In the presence of uniform gravity, having a horizontal
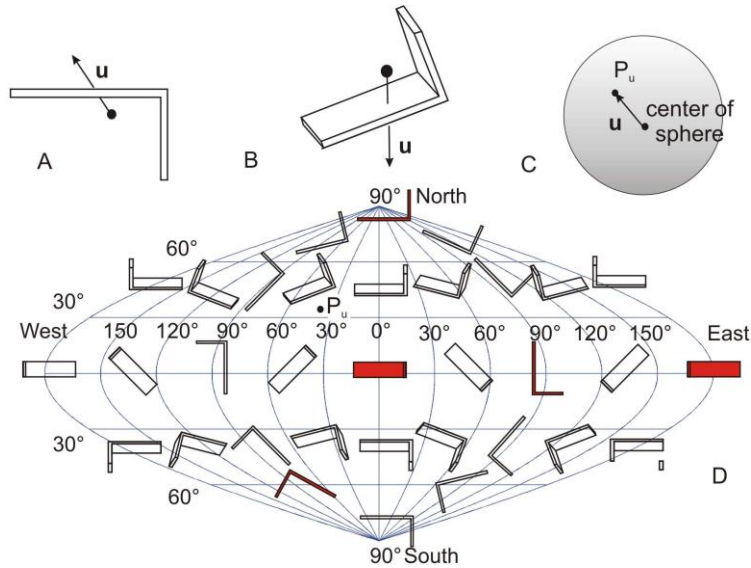
Fig. 1.A: reference configuration of an L-shaped object and a unit vector u. B: an element of the set of configurations (i.e. the pose) in which u points downwards; C: the corresponding point of a unit sphere. D: sinusoidal projection of the sphere with small figures illustrating poses corresponding to individual points. Filled figures indicate stable equilibria on a horizontal surface, which will be discussed in more depth in Sec. 2.4.

support plane in 3 dimensions also means that the system possesses rotational symmetry about a vertical axis, which motivates

***Definition 2.1.2** [71]: a pose of a rigid object in three dimensions is the set of configurations, generated from one single configuration by all possible combinations rotations about a vertical axis. and of translations.*

In simple words, pose determines, which side of the object faces down, but it does not determine, which side faces north or south.

Throughout this work, we will represent orientations of a planar body or poses of a spatial body in 3 different ways. The first representation is a unit vector **u** in 2 or 3 dimensions with the following meaning: a reference configuration of the object is considered together with the unit vector **u** (Fig. 1.A). There is a unique orientation/pose of the object, which includes those transformed images of the reference configuration, for which the transformed image of **u** points vertically *downwards* (Fig. 1.B). This particular pose is represented by **u**. As a second alternative, we can also represent the same

pose/orientation of the object by the point P_u of a unit sphere (3D) or circle (2D) determined by **u** (Fig. 1.C). For example, the 'South Pole' of the sphere represents the pose of the reference configuration and the 'North Pole' represents the pose, which is obtained by turning the reference configuration upside down. Fig. 1.D shows a standard sinusoidal projection of the sphere representation of pose space (a popular way to draw maps of the globe) with small pictures illustrating the poses of an object identified with specific points. The last representation of the pose **u** is by the unique point along the boundary of the object's convex hull, which is vertically below its center of mass in that pose. An example will be shown in Fig. 5 where poses of equilibrium are represented this way.

2.1.2 Functions representing object shape

Consider now a convex object with a reference frame whose origin is at the center of mass G of the object, and an arbitrary unit vector **u**. The following distance function $r(\mathbf{u})$ (Fig. 2) determines the shape of the object uniquely:

11
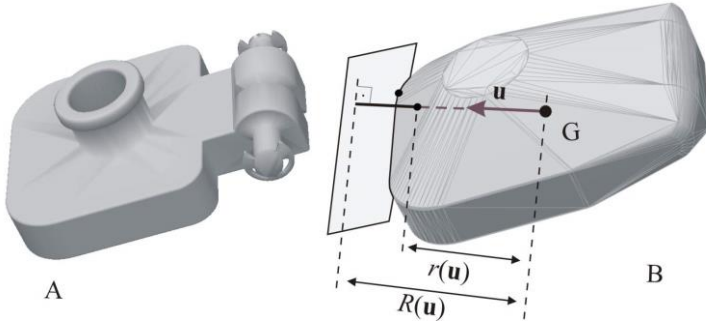
Fig. 2.A: example of a concave object (the body of a clamp) B: polyhedral approximation of its convex hull with definitions of the functions r(u) and R(u). The light grey plane is tangential to the surface of the object and it is perpendicular to u.

Definition 2.1.3: the distance function r($\mathbf{u}$) is the unique positive scalar such that r($\mathbf{u}$)$\mathbf{u}$ belongs to the boundary of the object for all $\mathbf{u}$.

It is also true that each object has a unique distance function due to the constraint that the distances are measured from the center of mass.

We will also use a second related function defined for convex and non-convex objects.

First, we introduce the concept of "tangentiality":

Definition 2.1.4: two objects are called tangential if their boundaries have nonempty intersection, but their interiors are disjoint

Importantly, this definition allows the objects to be non-smooth. The concept of tangential object is used in

Definition 2.1.5: the support function R($\mathbf{u}$) is the unique positive scalar such that R($\mathbf{u}$)$\mathbf{u}$ belongs to a plane tangential to the object and perpendicular to $\mathbf{u}$.

The support function (Fig. 2.B) determines the shape of convex objects uniquely moreover the support function of a concave object and that of its convex hull $\mathbb{H}$ are identical. The distance and support functions associated with the L-shaped object of Fig. 1 are depicted in Fig. 3.
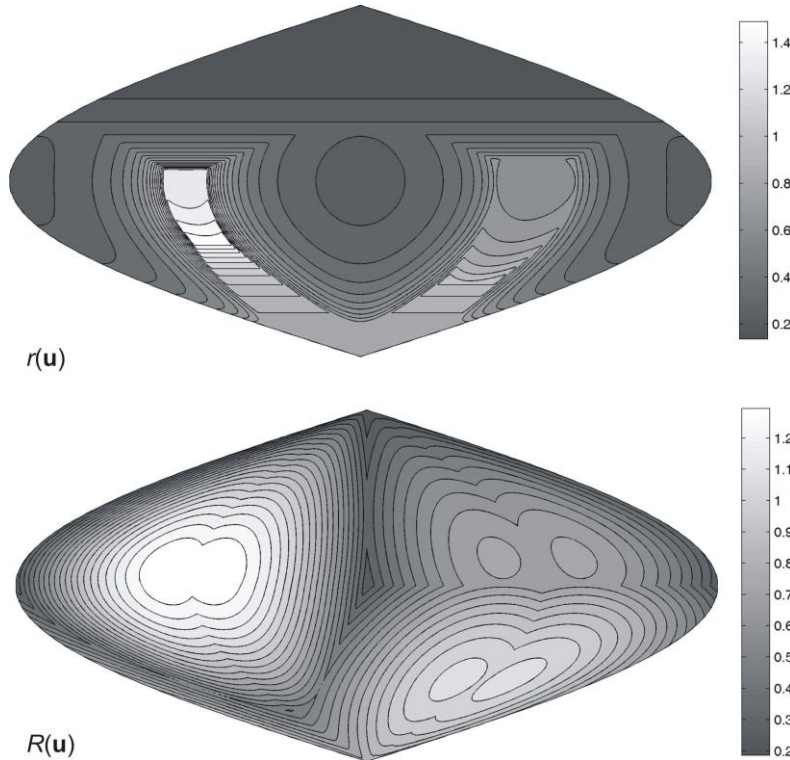
Fig. 3. Sinusoidal projections of the sphere representing pose space with countour plots of *r*($\mathbf{u}$) (top) and *R*($\mathbf{u}$) (bottom) associate with the L-shaped object of Fig. 1. Light colors indicate high values.
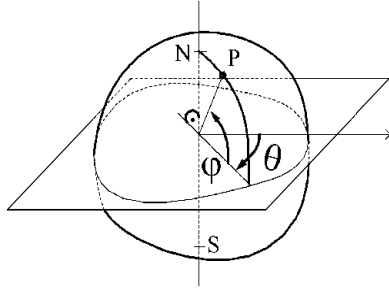
The support function is very useful if one aims to identify poses of equilibrium over a horizontal support. Objects are driven by gravity towards local minimum points of the potential energy function E_p. If we fix the pose **u** of the object, the lowest value of the potential energy corresponds to those configurations, in which the object is in contact with the support. The corresponding value of the potential energy is $E_p(\mathbf{u})=mgR(\mathbf{u})$ where m is the mass of the object and g is the constant of gravity. Such a pose corresponds to equilibrium if E_p has a singular (i.e. stationary) point at **u**. Hence, a vanishing gradient of $R(\mathbf{u})$ implies that pose **u** is an equilibrium and vice versa. It can be shown using elementary geometry that the gradients of $r(\mathbf{u})$ and $R(\mathbf{u})$ vanish at the same values of **u**; furthermore $r(\mathbf{u}) \leq R(\mathbf{u})$ with equality at equilibrium poses.

In some parts of the thesis we will use a polar angle φ or a pair of spherical angles (θ, φ) instead of **u** as independent variables of the distance function and the support function (Fig. 4). With a slight abuse of notation, we will use the same letters to refer to the two functions in the new variable, i.e. $R(\theta, \varphi)$, and $r(\theta, \varphi)$ in the 3D case; $R(\varphi)$ and $r(\varphi)$ in the planar case.

2.1.3 Algebraic approach to finding static equilibria and equilibrium classes

A planar, rigid body over a horizontal support line has typically isolated points of equilibrium in the space of orientations. A spatial rigid body has typically isolated points of equilibrium in pose space. These are what we refer to in Chapter 2 as "equilibria". We have found that the equilibria of a rigid body on a horizontal line (2D) or plane (3D) can be identified by inspection of the distance function or the support function associated with the convex hull ⊞ of the object. Namely, singular points of R (or equivalently, those of r) correspond to equilibria. For planar objects, there are two generic types of singular points: local minima and local maxima of R. In spatial systems, a third type of equilibrium associated with saddle points of R also becomes generic. Local minima of R correspond to stable equilibria of the object, whereas maxima and saddles correspond to unstable equilibria. Let s, u, and t denote the numbers of equilibria of the three types. Then, the *Poincaré-Hopf Theorem* [3] implies that $s=u$ in the planar case, and $s-t+u=2$ in the spatial case, i.e. u can be determined from s in the planar case and t from u, s in the spatial case. This simple observation motivates the following classification method of rigid bodies based on the number of equilibria.

Definition 2.1.6*: In two dimensions, class E_i (i=1,2,…) contains all bodies with s=i stable and u=i unstable equilibria.*

Definition 2.1.7*: In three dimensions, class $E_{i,j}$ (i,j=1,2,…) contains all bodies for which the number of equilibria are s=i, u=j, t=i+j-2.*

As simple examples, we mention the homogeneous, planar ellipse in class E_2 and the regular n-gons in class E_n; the homogeneous, spatial ellipsoid with three different axes in class $E_{2,2}$ the regular tetrahedron in class $E_{4,4}$ and the cube in class $E_{6,8}$.

In many applications, the number of unstable equilibria is less relevant than that of stable ones. Hence, we also define the simplified scheme of stability classes:

Definition 2.1.8: Stability class S_i includes objects in 2 or 3 dimensions with s=i stable equilibria.

Among the classes defined above, we will pay special attention to the following ones:

Definition 2.1.9: objects belonging to class S_1 are called monostatic.

Definition 2.1.10: 2D objects belonging to class E_1 and 3D objects in $E_{1,1}$ are called mono-monostatic.

While in the case of two-dimensional bodies, being monostatic implies being mono-monostatic (and vice versa), the three dimensional case is more complicated: a monostatic body could have, in principle, any number of unstable equilibria. As simple examples we mention the inhomogeneous, and mono-monostatic weeble toy (Fig. 5.A) and a monostatic (but not mono-monostatic) solid cylinder with chopped ends in class $E_{1,2}$ (Fig. 5.B).

2.1.4 The geometric approach to finding equilibria, and polygonal objects

We continue considering the convex hull $\mathbb{H}$ of an object. Assume that a planar object is in contact with a supporting line t. Then the line is tangential to $\mathbb{H}$. Let C denote the "contact set", i.e. the intersection of t with $\mathbb{H}$. C may be a single point or a line segment. There is a unique orientation of the object (referred to as $\mathbf{u}_0$) in which t is horizontal and it lies below the object (Fig. 6.A). Resting with this orientation in equilibrium requires the existence of unilateral
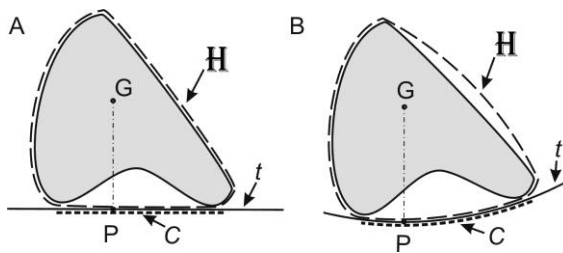
Fig. 6. Equilibrium of a planar object on a horizontal line (A) and in a hollow circle (B).
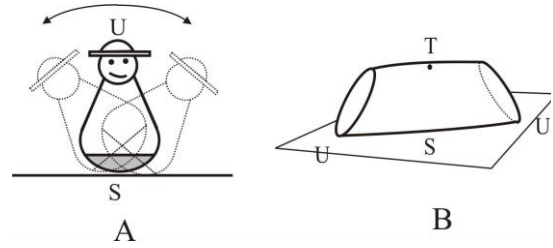
Fig. 5.A: a toy with one stable and one unstable equilibrium (i.e. an inhomogeneous, mono-monostatic body). B: a convex, homogeneous solid body with one stable equilibrium (monostatic body). In both plots, *S*, *T*, and *U* denote points of the surface which are under the center of mass when the body is in a sable (S), a saddle type (T) or an unstable (U) equilibrium.

(compressive) contact forces balancing the weight of the object. This condition is satisfied if the vertical projection P of the center of mass G to t is an element of C. The equilibrium is stable for rolling if the radius of curvature κ of the convex hull at P exceeds the corresponding value of the support function:

$$R(\mathbf{u}_0) = |GP| < \kappa \qquad (1)$$

[95] [105] [160]. For polygonal objects, the convex hull is also a polygon. There are two types of equilibrium: resting on a vertex and resting on an edge. The first type is always unstable ($\kappa=0$), and the second is always stable ($\kappa=\infty$). The stable equilibria can be found by projecting G to each edge of the convex hull. If the projection P is an internal point of the edge, resting on the edge is a stable equilibrium.

The conditions of existence and stability of equilibria in 3 dimensions are analogous to the planar case. Remarkable differences include the following:

1. polyhedra have three types of equilibria: resting on a facet, on an edge, and on a vertex of the convex hull. The first type is stable, the second and third are unstable.
2. stable equilibria of a polyhedron can be identified by projecting G to *each facet* of the convex hull. A projection inside the facet indicates a stable equilibrium.

2.2 THE MINIMUM NUMBER OF EQUILIBRIA ON A HORIZONTAL PLANE: ARNOLD'S PROBLEM

2.2.1 Problem statement

In this section, we study the number of static equilibrium poses (in short: equilibria) of bodies resting on a horizontal surface in the presence of uniform gravity. While many specific examples of solid bodies with a given number of stable equilibria have been demonstrated, *monostatic* and *mono-monostatic* bodies seem to be of special interest, as motion over a horizontal support, under the influence of gravity always ends in a particular final pose regardless of the intial conditions. We have seen that it is easy to construct a mono-monostatic body with non-uniform density distribution (Fig. 5). However, if we look for *homogeneous, convex* ones, the task is much more difficult. In fact, in Sec. 2.2.2, we will review the result of Domokos, Papadopoulos and Ruina [49] stating that

Theorem 2.2.1: *There are no convex, homogeneous objects in class E_1.*

More recently it was also pointed out in [170] that ***Theorem 2.2.1*** is equivalent to the famous Four-Vertex theorem [14] in differential geometry. The three-dimensional case poses even more difficult questions. Although one can construct a homogeneous, convex monostatic body (cf. Fig. 5.B), the task is far less trivial if we look for a monostatic polyhedron with *minimal number* of facets. Conway and Guy [43] constructed such a polyhedron with 19 faces (similar to the body in Fig. 5.B). It is still believed that this is the minimal number. It was shown by Heppes [79] that no homogeneous, monostatic tetrahedron exists. However, Dawson [47] showed that homogeneous, monostatic simplices exist in

d>7 dimensions. More recently, Dawson and Finbow [46] showed the existence of monostatic tetrahedra, however, with inhomogeneous mass density. At first sight it is not clear what could be the spatial analogue of ***Theorem 2.2.1***: emptiness of the classes $E_{1,1}$ (mono-monostatic)*, $E_{1,i}$* (monostatic) or $E_{i,1}$ are all candidate statements. As V.I. Arnold pointed out [50], the essence of ***Theorem 2.2.1*** is that in two dimensions the minimal number of equilibria is *four*. The only three-dimensional bodies with less than four equilibria are the mono-monostatic ones, i.e. class $E_{1,1}$. (For example, the monostatic body in Fig. 5.B represents class $E_{1,2}$, and it has 1 stable, 2 unstable and 1 saddle-type equilibrium, four equilibria altogether.) Hence the three-dimensional analogy of ***Theorem 2.2.1*** would be the emptiness of class $E_{1,1}$. Arnold hinted that a 3D counterexample, with less than 4 equilibria (i.e. a mono-monostatic body) may nevertheless exist. With our current notation this would mean

Theorem 2.2.2: *Class $E_{1,1}$ contains convex, homogeneous objects*

Our primary goal in Sec. 2.2 is to confirm Arnold's initial guess by proving ***Theorem 2.2.2***. We review the proof of ***Theorem 2.2.1*** in Sec. 2.2.2, and point out why it is not applicable in three dimensions. The failure of the proof provides us with a hint about how a 3-dimensional mono-monostatic body could look like. Following this trace, we proceed in Section 2.2.3 by constructing a two-parameter family of smooth, closed surfaces in a spherical coordinate system. The bodies representing class $E_{1,1}$ are embedded in this family and Section 2.2.3 defines the values of the two

parameters associated with them. The existence of appropriate values of the parameters is demonstrated analytically, and several solutions including the „Gömböc" shape are determined numerically. The proofs of some lemmas are presented in Appendix 5.1 to improve the readability of the main text. In Section 2.2.5, we use complete induction (based on the idea of the egg of Columbus) to prove a natural generalization of **Theorem 2.2.2** in the form of

Theorem 2.2.3: *there are convex, homogeneous objects in class $E_{i,j}$ for all $i,j>0$.*

and Sec. 2.2.6 is devoted to a brief summary of some recent works motivated by the results of the thesis.

2.2.2 The planar case

Theorem 2.2.1 can be proven as follows. Consider a convex, homogeneous planar object $\mathbb{B}$ and a polar coordinate system with its origin O coinciding with the center of gravity G of $\mathbb{B}$. We assume that the distance function r associated with $\mathbb{B}$ is differentiable and we use the angle φ in the polar coordinate system as independent variable of function r. Assume that $\mathbb{B}$ is in class E_1, i.e. $r(\varphi)$ has only one local maximum and one local minimum. In this case, there exists exactly one value $\varphi=\varphi_0$ for
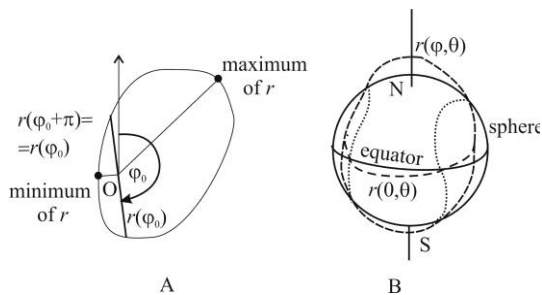
Fig. 7.A: Example of a convex, homogeneous, planar body represented by a distance function $r(\varphi)$ with two local extrema. B: a 3D body (dashed line) cut to a 'thin' and a 'thick' half by a tennis ball-like space curve (dotted curve) along which $r=r_0$. Continuous line shows a sphere of radius r_0, which also contains this curve.

which $r(\varphi_0)= r(\varphi_0+\pi)$, moreover, $r(\varphi)>r(\varphi_0)$ if $\pi>\varphi-\varphi_0>0$, and $r(\varphi)<r(\varphi_0)$ if $-\pi<\varphi-\varphi_0<2\pi$ (see Fig. 7.A). The straight half lines $\varphi=\varphi_0$ and $\varphi=\varphi_0+\pi$ of the polar coordinate system passing through O cut $\mathbb{B}$ into a "thin" $(r(\varphi)<r(\varphi_0))$ and a "thick" $(r(\varphi)>r(\varphi_0))$ part. This implies that *O can not coincide with the center of gravity,* contradicting our initial assumption, which completes the proof. •

Some elements of this proof are applicable to three dimensions. Similarly to the planar case, a 3D body in class $E_{1,1}$ can be cut in a unique way to a 'thin' and a 'thick' half along a closed level curve of the distance function r. By „halves" we mean two parts of the boundary such that the centroid solid angles associated with each of the two parts is 2π. (The concept of a solid angle will be used later and its definition is given in Appendix 5.5.3.) If this separatrix curve happens to be planar, its existence leads to contradiction (if, for example it is the 'equator' $\varphi=0$ and $\varphi>0/\varphi<0$ are the thick/thin halves, the center of gravity should be on the upper ($\varphi>0$) side of the origin). However in the case of a generic, spatial separatrix, the above arguments no more apply. In particular, the curve can be similar to the ones on the surfaces of tennis balls (Fig. 7.B). In this case the 'upper' thick ('lower' thin) part is partially below (above) the equator, thus it is possible to have the center of gravity at the origin. Our construction in the next section will be of this type.

2.2.3 A parametric family of candidate shapes

In this section, we define a suitable two-parameter family of functions $r(\theta,\varphi,c,d)$ in the spherical coordinate system of Fig. 4 where the spherical angles take values in $-\pi/2<\varphi<\pi/2$ and $0\leq\theta\leq2\pi$. $c>0$ and $0<d<1$ are parameters. The solid, homogeneous body bounded by r is denoted by $\mathbb{B}$. In Section 2.2.4 we will identify a range of the two
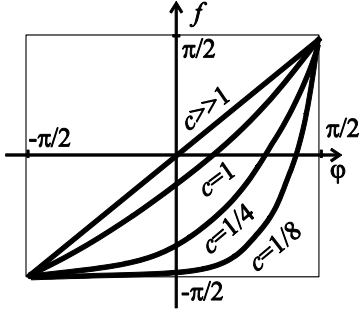
Fig. 8. The $f(\varphi)$ function at some values of c.

parameters where r is the distance function of $\mathbb{B}$, i.e. the center of mass of $\mathbb{B}$ is in the origin of the polar coordinate system; moreover $\mathbb{B}$ is convex and mono-monostatic.

Conveniently, r can be decomposed in the following way:

$$r(\theta,\varphi,c,d) = 1 + d \cdot \Delta r(\theta,\varphi,c) \qquad (2)$$

where Δr represents the shape of the deviation from the unit sphere. 'Thin'/'thick' parts of the body are characterized by negative/positive values of Δr (i.e. the separatrix between the thick and thin portions will be given by $\Delta r=0$), while the parameter d is a measure of the 'lumpyness' of the surface.

Our next goal is to define a suitable function Δr. We will have the maximum/minimum points of Δr ($\Delta r=\pm 1$) at the North/South Pole of the coordinate system ($\varphi=\pm\pi/2$). The shapes of the thick and thin portions of the body are controlled by the parameter c: for $c\gg 1$ the separatrix will approach the equator, for smaller values of c the separatrix will become similar to the curve on the tennis ball.

Consider the following smooth, one-parameter mapping $f(\varphi,c)$: $(-\pi/2,\pi/2) \rightarrow (-\pi/2,\pi/2)$:

$$f(\varphi,c) = \pi \cdot \left[\frac{e^{\left[\frac{\varphi}{\pi c}+\frac{1}{2c}\right]} - 1}{e^{1/c} - 1} - \frac{1}{2} \right]. \qquad (3)$$

For very large values of the parameter ($c\gg 1$), this mapping is almost the identity, however, if c is close to 0, the deviation from linearity is large (cf. Fig. 8).

Based on f, we define the related maps (Fig. 9)

$$f_1(\varphi,c) = \sin(\,f(\varphi,c))\,, \qquad (4)$$

$$f_2(\varphi,c) = -f_1(-\varphi,c)\,. \qquad (5)$$

These two functions are used to obtain the planar sections $\theta=0$ and $\theta=\pi/2$ of the object:

$$\Delta r(0,\varphi,c) = \Delta r(\pi,\varphi,c) = f_1(\varphi,c) \qquad (6)$$

$$\Delta r(\pi/2,\varphi,c) = \Delta r(3\pi/2,\varphi,c) = f_2(\varphi,c) \qquad (7)$$

which will become two planes of symmetry of the object. A big portion of section (6) of $\mathbb{B}$ lies in the thin part, while the majority of section (7) is in the thick part. The function
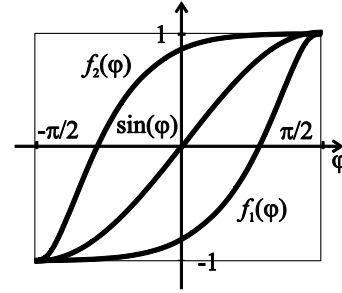
Fig. 9. The $f_1(\varphi)$, $f_2(\varphi)$, and $\sin(\varphi)$ functions at $c=1/3$
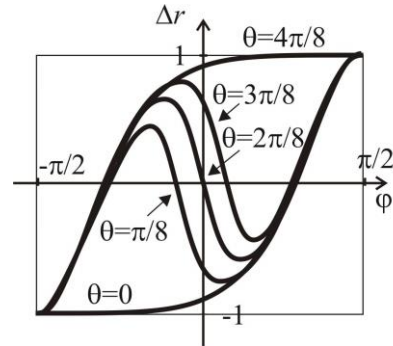
Fig. 10. Sections of the $\Delta r(\theta,\varphi)$ function at constant values of θ; $c=1/4$

17

$$a(\theta,\varphi,c) = \frac{\cos^2(\theta)\cdot\left(1 - f_1^2\right)}{\cos^2(\theta)\left(1 - f_1^2\right) + \sin^2(\theta)\cdot\left(1 - f_2^2\right)} =$$

$$= \frac{1}{1 + \tan^2(\theta)\dfrac{\cos^2(f(\varphi,c))}{\cos^2(f(-\varphi,c))}} \qquad (8)$$

is used to generate values of Δr between the previously specified two sections as a 'weighted average' type function of f_1 and f_2 in the following way (Fig. 10):

$$\Delta r(\theta,\varphi,c) = \begin{cases} a\cdot f_1 + (1 - a)\cdot f_2 & if \ |\varphi| < \pi/2 \\ 1 & if \ \varphi = \pi/2 \\ -1 & if \ \varphi = -\pi/2 \end{cases} \qquad (9)$$

The choice of the function a ensures on the one hand a smooth transition from f_1 to f_2 if θ is varied between 0 and $\pi/2$. On the other hand it produces a tennis ball-like separatrix between the thick and thin halves of the body (as in Fig. 7.B).

The function r defined by equations (2)-(9) is illustrated in Fig. 11 for intermediate values of c and d. Before we identify suitable ranges of the parameters, where r is a valid distance function and the corresponding body $\mathcal{B}$ is convex and mono-monostatic, let us briefly comment on the effect of c. For $c \gg 1$, the constructed surface $r = 1 + d\Delta r$ is separated by the $\varphi = 0$ equator into two halves: the upper ($\varphi > 0$) half is 'thick' ($r > 1$) and the lower ($\varphi < 0$) half is 'thin' ($r < 1$) as shown in Fig. 12.A. By decreasing c, the line separating the "thick" and "thin" portions becomes a space curve, thus the thicker portion moves downward and the thinner portion upward. As c approaches zero, the upper half of the body becomes thin and the lower one becomes thick (Fig. 12.B).

2.2.4 Proof of the main result

The proof of ***Theorem 2.2.2*** makes use of 3 lemmas. The first one

Lemma 2.2.4: the function r, defined in equations (2)-(9) of the previous section, has two singular points, namely the poles N and S
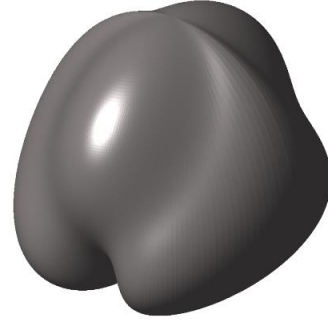
Fig. 11. Plot of $\mathcal{B}$ if $c=d=1/2$

deals with singular points of r, which becomes extremely useful because of the tight connection between singular points of distance functions and equilibria of convex objects. In Appendix 5.1.2, we demonstrate the singularity of the degenerate 'poles' of the spherical coordinate frame ($\varphi = \pm\pi/2$), by proving

$$\left.\frac{\partial r(\theta,\varphi,c,d)}{\partial\varphi}\right|_{\varphi=\pm\pi/2} = 0 \ \text{for any} \ \theta. \qquad (10)$$

which follows from elementary properties of the $\sin(\dots)$ function in (4), (5). At any other point, r is singular iff

$$\frac{\partial r(\theta,\varphi,c,d)}{\partial\varphi} = \frac{\partial r(\theta,\varphi,c,d)}{\partial\theta} = 0 \qquad (11)$$

As we show in the appendix, this is never satisfied because $\partial r/\partial\varphi > 0$ if $\theta = 0, \pi/2, \pi, 3\pi/2$, and $\partial r/\partial\theta \neq 0$ for all other values of θ. The two steps outlined above complete the proof of ***Lemma 2.2.4***.

The second lemma

Lemma 2.2.5: there exist positive constants $c_1 < c_2$, δ_0, and a function $F_1(d)$, such that for arbitrary $d < \delta_0$, $F_1(d)$ is inside the open interval (c_1,c_2) and $c = F_1(d)$ implies $G \equiv O$.

identifies a one-dimensional manifold in parameter space, along which r is a distance function, i.e. the center of gravity G of $\mathcal{B}$ coincides with the origin O of the reference frame.
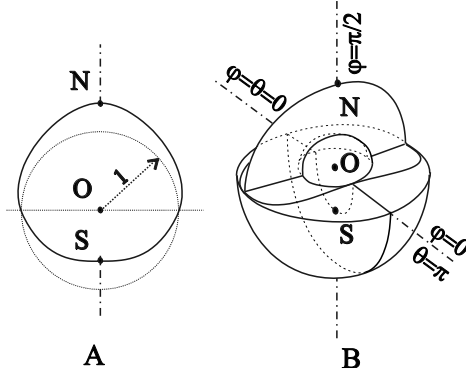
Fig. 12. A: Side view of $\mathbb{B}$ if $c>>1$ (and $d\approx1/3$). Note that, the object is a surface of revolution, moreover $\Delta r>0$ if $\varphi>0$, and $\Delta r<0$ if $\varphi<0$. B: Spatial view of $\mathbb{B}$ if $c<<1$. Here, $\Delta r>0$ typically for $\varphi<0$ and vice versa.

Lemma 2.2.5 is demonstrated in Appendix 5.1.2. The basic idea of the proof is illustrated by Fig. 12: if $c<<1$, then the center of mass is below the origin, whereas in the limit of $c\rightarrow\infty$, it is above the center of mass. We use continuity arguments to prove the existence of the intermediate values $c=F_1(d)$ where the two points coincide. The statement of *Lemma 2.2.5* is also illustrated in Fig. 13 where we have sketched the function F_1 within the rectangular box determined by the bounds $c_1<c<c_2$, and $0<d<\delta_0$.

Finally, the convexity of $\mathbb{B}$ is an important requirement, and thus we will also prove

Lemma 2.2.6: there exists a continuous, positive function $F_2(c)>0$ for any $c>0$ such that $\mathbb{B}$ is convex whenever $d< F_2(c)$.

The idea of the proof is extremely simple: in the limit of $d\rightarrow0$, the shape of $\mathbb{B}$ approaches a sphere, which is convex. Some technical difficulties arise from the singularity of the coordinate frame at the poles. For full description, see Appendix 5.1.3. The statement of this lemma is again illustrated by Fig. 13 where we sketched the function $F_2(c)$, which is positive over the $[c_1,c_2]$ interval and thus it lies above a part or the whole of the grey box.

With the 3 lemmas at hand, we are now ready to prove *Theorem 2.2.2*. Since $F_2(c)$

is a positive, continuous function, it has a global minimum $d_0>0$ over the closed interval $[c_1,c_2]$ according to the Extreme value theorem [102]. If $d<\min[\delta_0,d_0]$ and $c=F_1(d)$ then, according to *Lemma 2.2.5* and *Lemma 2.2.6*, $\mathbb{B}$ is convex and its center of gravity is at the origin. Due to *Lemma 2.2.4*, $\mathbb{B}$ has two static equilibria, marked by the singular points of r. Thus we conclude that homogeneous, convex, mono-monostatic bodies exist. •

Numerical analysis shows that d must be very small ($d<5\cdot10^{-5}$) to satisfy convexity together with the other restrictions, so the object constructed this way is very similar to a sphere. (In the admitted range of d the other parameter is approximately $c\approx0.275$.). Hence, the physical demonstration of the monostatic behavior of these objects might be problematic. This topic will be discussed further in Sec. 2.2.6. We remark that [49] also demonstrates the statement analogous to *Theorem 2.2.1* for closed, homogeneous, planar *thin wires*. The 3D analogue for convex, homogeneous spatial *thin shells* is again false, which can be proven in the same way as *Theorem 2.2.2.*

2.2.5 The egg of Columbus and complete induction

According to some accounts, Christopher Columbus attended a dinner, which a Spanish gentleman had given in his honor. Columbus asked the gentlemen in attendance to make an egg stand on one end. After the gentlemen successively tried to
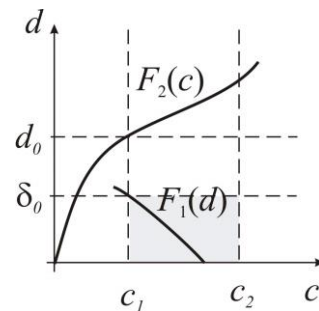
Fig. 13. Illustration for *Lemma 2.2.5* **and** *Lemma 2.2.6***.**
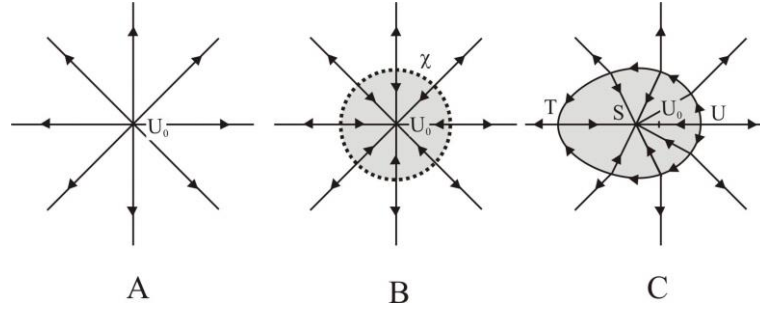
Fig. 14. Analysis of the Egg of Columbus. A: Negative gradient flow of the distance function *r* of the original egg near the tip U_0. (unstable equilibrium point.) B: Hitting the table with vertical egg axis creates a modified flow containing one minimum at U_0 and a set χ of degenerated equilibria. C: Hitting the table with slightly tilted egg axis creates a modified flow containing one minimum (*S*), one saddle (*T*) and one maximum (*U*). Grey color indicates the flat part of the egg.

and failed, they stated that it was impossible. Columbus then placed the egg's small end on the table, breaking the shell a bit, so that it could stand upright. Columbus then stated that it was "the simplest thing in the world. Anybody can do it, after he has been shown how!" The egg of Columbus has become a metaphor for natural simplicity. In this section we prove ***Theorem 2.2.3*** by induction. Our inductive argument is as simple as the egg of Columbus – and not just metaphorically.

Theorem 2.2.2 (proven in the previous sections) asserts the non-emptiness of class $E_{1,1}$. Assume that class $E_{i,j}$ is non-empty. If we can find a way to add one local minimum to the function *r* while keeping the number of maxima constant (and vice versa) by small perturbations not violating the convexity of the body, then the non-emptiness of all classes $E_{i+1,j}$ and $E_{i,j+1}$ *(i,j>0)*, and thus ***Theorem 2.2.3*** is proven.

The first, naive interpretation of the Columbus story is that he *turned* an unstable equilibrium point (Fig. 14.A) into a stable one. However, a closer look at the egg reveals that Columbus did something more complex. Based on the superficial account, we cannot decide which of the following scenarios were actually realized (supposing that the egg had a perfect rotational symmetry):

(i)   If Columbus hit the table with the egg so that the symmetry axis of the egg was exactly vertical, then by breaking the shell at the tip, he produced a small flat area on the surface, which corresponds to one new stable equilibrium point in the middle of a circle of degenerated balance points. This scenario is illustrated in Fig. 14.B.

(ii)   If the axis was somewhat tilted, then by breaking the shell at the unstable equilibrium point (maximum) he produced a small flat area containing one stable equilibrium point (minimum) inside the flat part and one saddle and a maximum at the borderline. This scenario is illustrated in Fig. 14.C.

Scenario (ii) is exactly what we need to produce an additional stable equilibrium without creating new maxima. Since the Columbus algorithm applies only to degenerate local maximum points of *r*, where *r* has perfect rotational symmetry, we will use a slightly different technique to produce additional maxima and minima one by one in the distance function.

A Increasing the number of stable equilibria by one

Consider a stable equilibrium of an object **B** and the corresponding local minimum point S_0 of the associated distance function (Fig. 15.A). Our geometric construction will assume that the surface of **B** is smooth and strictly convex in a close neighborhood of S_0. Consider another point S_1 on a sphere

20
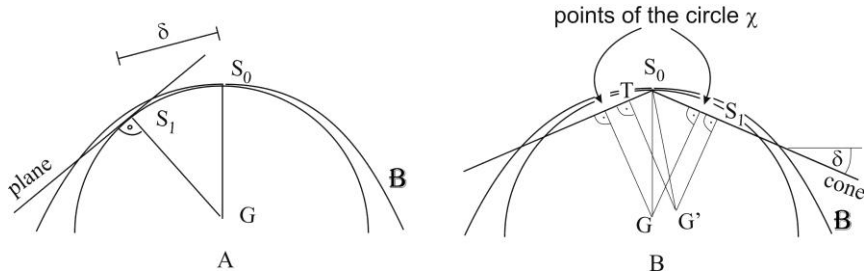
Fig. 15.A: the figure shows a section of $\mathcal{B}$ in the GS_0S_1 plane with the steps of adding one stable equilibrium point. B: a section of $\mathcal{B}$ in the GS_0G' plane with the steps of generating one unstable equilibrium point. For notation, see main text.

containing S_0 and centered at the center of mass G of $\mathcal{B}$, such that the distance between S_1 and S_0 is $\delta \ll 1$. The tangent plane of this sphere at S_1 divides $\mathcal{B}$ to two parts, one of which is a small cap. We remove the cap. If we assume for a minute that the center of mass stays at G, then the modified distance function r^* corresponding to the truncated body still has a local minimum at S_0 and a new local minimum at S_1. A new saddle point T also emerges, which is a straightforward consequence of the Poincaré-Hopf theorem. This situation is illustrated in Fig. 15.A, the negative gradient flows of r and r^* are sketched in Fig. 16.A and B, respectively.

The truncation of the body moves the center of gravity G of $\mathcal{B}$ by $O(\delta^4)$. This effect may perturb the locations of the stationary points of the distance function by $O(\delta^4)$ nevertheless the structurally stable picture of Fig. 16.B does not change qualitatively. It is also worth noting that a small neighborhood of S_0 remains smooth and strictly convex. Thus, the step of adding a new equilibrium can be repeated several times with S_0 serving as initial minimum point of the distance function.

B Increasing the number of unstable equilibria by one

Again, consider a stable equilibrium and the associated local minimum point S_0 of the distance function r. Draw a very flat cone of revolution ($\delta \ll 1$, see Fig. 15.B), with axis GS_0 and with its peak at S_0. The cone again

cuts $\mathcal{B}$ to two parts, and we remove the small one. If we now assume that the center of mass remains at G, the modified distance function r^* has a local maximum at S_0, it is decreasing radially until it reaches a circle χ of non-isolated equilibria and beyond the circle, it is increasing radially (Fig. 16.C).

The effect of the deviation of G on the number and type of equilibria can again be neglected if δ is small, with the exception of the circle of equilibria χ, which is degenerate and structurally unstable. Typically, the new center of mass G' is off the GS_0 line. In this case, the new distance function r^{**} will have one isolated minimum S_1 and a saddle point T instead of χ (Fig. 16.D, Fig. 15.B). In the non-typical case when G' happens to be on the line GS_0, then χ is preserved, however it can be broken up into a minimum and a saddle point by an adequate small perturbation of r^{**}. Finally, we have one stable (S_1) one saddle (T) and one unstable equilibrium (S_0) instead of the original stable point S_0.

The truncated body is weakly convex in the neighborhood of the new local minimum point S_1. Strong convexity can be restored by a further small perturbation of r (details omitted). If several new equilibria are generated, S_1 can be used as the initial local minimum point of the distance function at the repeated step of adding an equilibrium.

C Completing the proof of Theorem 2.2.3.

In the previous two parts we showed how convex bodies in class $E_{i+1,j}$ or in class $E_{i,j+1}$

21

can be generated by using a body of class $E_{i,j}$. Since **Theorem 2.2.2** proved the non-emptiness of class $E_{1,1}$, we now showed that none of the classes $E_{i,j}$, $i,j>0$ is empty   •.

2.2.6 Discussion

In this section, we introduced the notion of equilibrium classes in two and three dimension. We proved that all classes contain convex, homogeneous objects in 3D. Among all classes, the non-emptiness of $E_{1,1}$ was the most important results of the section. The proofs relied on elementary mathematical tools such as basic geometry and differential geometry. Given this simplicity, one may ask, how it is possible that the existence of mono-monostatic objects was not proved before? And why did people not discover elementary examples of objects in this class?

To understand this apparent contradiction, we performed some research for real-world representatives of mono-monostatic shapes. There exist objects in Nature in abundant numbers, which are very close to the mathematical abstraction of a convex, homogeneous rigid body: pebbles on the coast. We have studied the relative frequencies of equilibrium classes in a sample of 2000 pebbles from the coast of Rhodes, Greece. Interestingly, none of the pebbles was monostatic, and of course, there was no member of class $E_{1,1}$ among them. A semi-quantitative explanation of this behavior was given in [170], which is not repeated here. The main message of this examination was that mono-monostatic objects – if they exist – must be similar to the sphere, and such shapes are very sensitive to perturbations. This finding appears to be consistent with the result of our constructive proof, which provided us with mono-monostatic objects very close to the sphere.
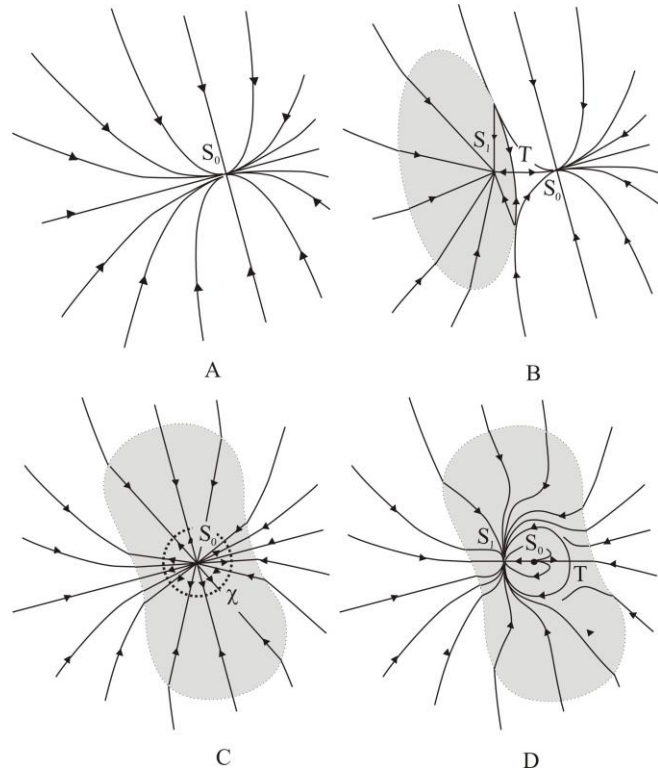
Fig. 16.A: Gradient flow of the distance function r of an object in the neighborhood of a local minimum point S_0. B: gradient flow of the modified function r^* generated by truncation of the object along a plane. A second minimum S_1 and a saddle point T occur. C: modified function r^* if the body is truncated along a cone. S_0 becomes local maximum and a circle χ of non-isolated singular points emerges on the cone. D: Because of the deviation of the center of gravity, the distance function r^{**} of the chopped object is a perturbed version of r^*. The structurally unstable circle typically breaks up to a minimum S_1 and a saddle point T. Grey color indicates the regions directly affected by the truncation.

Despite these discouraging preliminary results, we continued the search for better representatives of class $E_{1,1}$. By following the basic idea of Sec. 2.2.3, and by combining second-order surfaces (planes, ellipsoides, elliptic cones and cylinders) into a convex but non-smooth closed surface, we were able to produce a shape with 2 planes of symmetry (Fig. 17.A,B), which became known as the 'Gömböc'. We also created another similar shape with 3 planes of symmetry. In both cases, the level curves of the distance function follow tennis ball-like non-smooth curves (Fig. 17.B). The location of the center of gravity of these objects was determined numerically. With

A   B
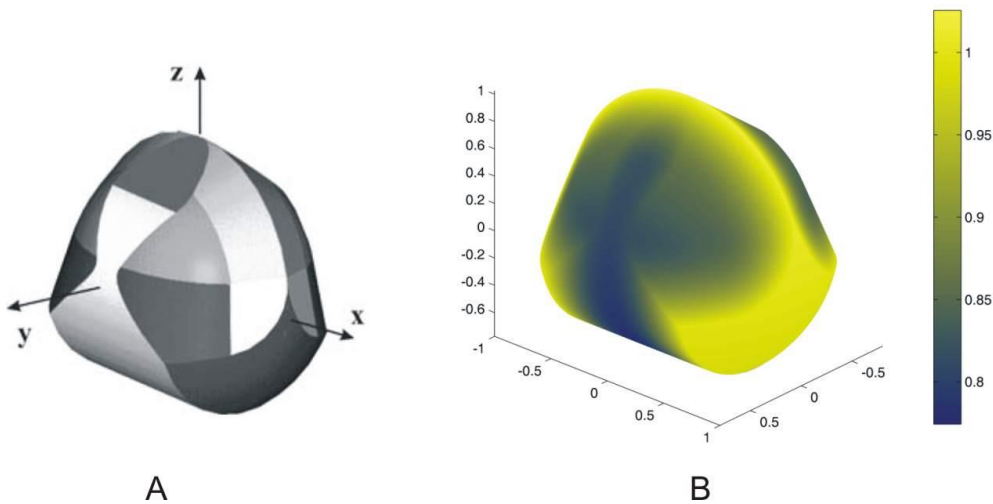
Fig. 17.A: second-order surface components of the Gömböc shape B: the Gömböc shape with surface coloring of the surfaces representing distance from the center of gravity. Notice that level curves of the distance function *r* resemble the "tennis ball curve".

those values at hand we could verify easily that they are mono-monostatic.

Even though the Gömböc shape was never developed into a fully analytic answer to Arnold's question, its apparent simplicity greatly contributed to the impact of this result both in and outside of the scientific community. To mention two examples, the Gömböc inspired the shapes of aerial robots developed recently at the University of Pennsylvania [113] and it became the title of an award-winning short movie by the German director Ulrike Vahl [90].

The rarity of mono-monostatic shapes in the physical world is our primary motivation to investigate the shapes of turtles, which is the subject of Sec. 2.3, below. The preliminary experiments with pebbles also inspired further research activity in the group of Gábor Domokos, in which the author of this thesis was also involved to some extent. This work includes for example the geological application of equilibrium classes [52] [51] as well as a refinement of equilibrium classification, which takes into account the topological structure of the distance function [48], which are beyond the scope of this thesis.

2.3 EQUILIBRIUM CLASSES AND SELF-RIGHTING ANIMALS

2.3.1 Monostatic shapes in Nature

The ability of self-righting is crucial for animals with hard shells [64] [59] [65] [164], e.g. beetles and turtles. It is often used as a measure of individual fitness

[66][153][7][33], although it is also influenced by the environment e.g. temperature [55]. Both righting behavior [6] [140] [150] [181] and the evolution of shell morphology [41] [114] [144] of turtles have been studied recently. An example of their interaction is the sexual dimorphism of species where males are often overturned

during combats [103] [23] [191], and their shell has adapted to facilitate righting. The aim of this section is to study the morphology of the turtle shell, and self-righting behavior, from a geometric point of view. We develop a geometric shell model based on field data, to uncover systematically the connections between righting strategies and stability classes.

In the perspective of self-righting, the class *of monostatic objects* is of special interest. Turtles in S_1 can self-right on a horizontal surface without any effort. The pebble experiment reviewed in Sec. 2.2.6 suggests that monostatic bodies are rare in nature. Even rarer are mono-monostatic bodies; nevertheless, the shapes of some highly domed terrestrial tortoises are somewhat reminiscent of them (Fig. 13 vs. Fig. 18.D). One of the motivations of this work is to discover whether monostatic shell shapes exist or not. In Sec. 2.3.2, we develop a simple geometric model of the shell. Model parameters are fitted to real measured shapes in Sec. 2.3.3. The stability class of the fitted model is numerically determined and compared with in vivo experimental data about the righting behavior of turtles in Sec. 2.3.4.

2.3.2 A parametric morpho-logical model of the turtle shell

We construct the shell model in three steps: transversal model, longitudinal model and 3D model. We also describe the technique to determine the equilibrium class of the final 3D model.

In the shell model (Fig. 18), a planar curve represents the approximate transversal contour of the shell (*transversal model*, see Fig. 18.A). This curve has 3 parameters (Fig. 19): p, controlling the shape of the carapace, h defining the height/width ratio of the contour, and k, determining the transition between plastron and carapace.

The transversal model (Fig. 18.A) is constructed in a polar coordinate system, with its origin at the middle of the contour, both horizontally and vertically. The height and the width of the cross-section are scaled to $2h$ and 2, respectively. The contour curve $K(\alpha,p,h,k)$ of the cross-section is achieved from the curves of the plastron (P) and of the carapace (C). The plastron is approximated by a straight line, given in our polar coordinate system by the function

$$P(\alpha,h,k) = \begin{cases} p_0 / \cos\alpha & \text{if} \quad -\pi/2 \le \alpha \le \pi/2 \\ \text{(not defined otherwise)} \end{cases} \quad (12)$$
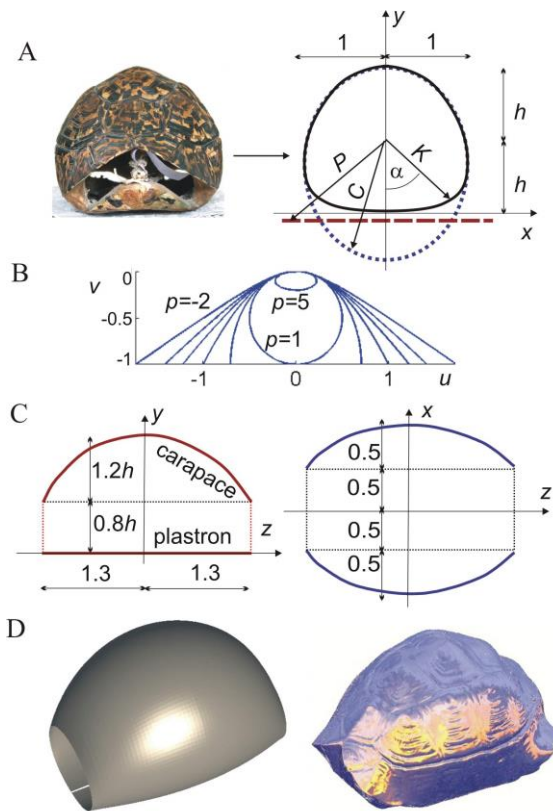
Fig. 18. Turtle shell model. A: Frontal view of shell (Stigmochelys pardalis) and three-parameter transversal model $K(\alpha,h,p,k)$ of main cross section. The plastron is approximated by straight line P, see (12). The carapace is approximated by curve C, see (13)-(15). A smooth transition between the plastron and the carapace is achieved by a merging function (16). B: Carapace shape at various values of parameter p. C: Longitudinal model: schematic side-and top-view contours are circular arcs obtained as averages from measurements. Sizes are normalized. D: Visual comparison of digitized shell image and model surface.
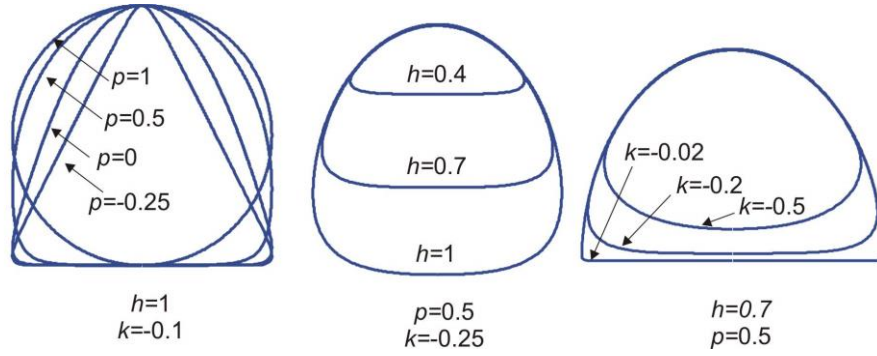
Fig. 19. Main cross section at various parameter values. Parameter _p_ determines the shape of the carapace, _h_ determines the relative positions of the carapace and plastron (height/width ratio), _k_ determines the roundedness at the carapace-plastron transition .

where p_0 is a scaling factor to be determined later. The shape of the carapace is first approximated in an orthogonal _u-v_ coordinate system by the curve

$$u = \pm(-v - pv^2)^{1/2} \qquad (13)$$

(Fig. 18.B). This curve is either an ellipse ($p>0$) or a hyperbola ($p<0$). Next, the curve is expressed in the polar coordinate system of Fig. 18.A by substituting

$$u = c_0 C \sin \alpha \qquad (14)$$

$$v = -c_0[C \cos \alpha + h] \qquad (15)$$

into (13) and by solving the resulting equation for C; c_0 is again a scaling factor to be determined later. The final contour $K(\alpha,h,p,k)$ is constructed as

$$K = \left[C^{1/k} + P^{1/k}\right]^k \qquad (16)$$

where the negative parameter $0>k>-1$ determines the roundedness of the transition between the plastron and the carapace. The factors c_0 and p_0 are determined numerically from the respective constraints that the lowest point of the final contour is at distance h and the widest points are at distance 1 from the origin of the polar coordinate system. Then, the highest point of the carapace will be at distance h above the origin (since the point $(u,v)=(0,0)$ of the curve corresponds to $(C,\alpha)=(h,\pi)$, cf. (14), (15). At some values of α, the curves P (for $\pi/2< \alpha \le 3\pi/2$) and C (in an interval around $\alpha=0$ if $p<0$) are not defined. Here, (16) is replaced by $K\equiv C$ and $K\equiv P$, respectively.

The _longitudinal_ model, describing side- and top-view contours of the shell is given by Fig. 18.C. These particular shapes have been chosen by using averaged data from the above-mentioned 30 individuals. Needless to say, the circular and straight contours, and the specific parameter values of Fig. 18.C do not represent precise fit to real animals. However, the mechanical behavior of the shell model is much less sensitive to these curves than to the shape of the transversal model: turtles _always_ roll transversally along the perimeter of the main cross-section. The only significant effect of the longitudinal model is to modify the height of the center of gravity. Slightly modified longitudinal curves have been
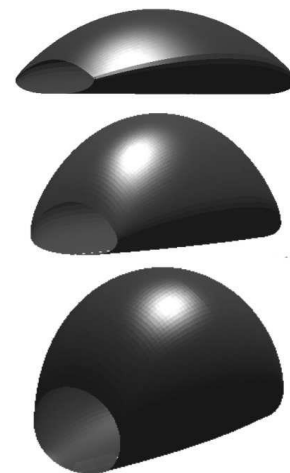
Fig. 20. Model shape at various parameter values. From top to bottom: _h_=0.4, 0.65, 0.9. In all cases the remaining two parameters _p_ and _k_ are obtained from the regression lines _p_=2.59_h_-1.51, _k_=0.90_h_-1.01.

25

tested and showed identical qualitative behavior.

Finally, the *3D model surface* emerges as a series of horizontally and vertically scaled versions of the main transversal section, fitting the longitudinal contours (Fig. 18.D, Fig. 20).

To determine the stability class of the model at given values of *p, h* and *k*, the center of gravity G of the model has to be found numerically. Due to the two planes of reflection symmetry, only the vertical coordinate of G needs to be computed. The distance function *r* corresponding to the 3D model, and its stationary points can be determined numerically in a straightforward way. The stability class S_i is identified by counting the local minimum points of *r*.

Our 3D model leaves the rostral and caudal ends of the shell undefined; we assume that the turtle has only unstable equilibrium points in these domains, in accordance with the facts that the real shells are somewhat elongated and turtles do not tend to get stuck in head- or tail-down positions.

2.3.3 Parameter fitting of the shell model

Contours (cf. Fig. 21) of 30 turtles belonging to 17 species have been digitized and the three parameters *p, h* and *k* of the transversal model were fitted to these contours by considering $n \approx 1000$ equidistant angles $\alpha_i = 2i\pi/n$ $(i=1,2,\ldots,n)$ in our polar

coordinate system and by minimizing the mean square radial error

$$e = \sqrt{\frac{1}{n}\sum_i \left[K(\alpha_i) - Q(\alpha_i)\right]^2} \qquad (17)$$

Here, $K(\alpha_i)$ and $Q(\alpha_i)$ denote points of the model and the measured contour, respectively. The results of the parameter-fitting are summarized in Fig. 22.A,B and in Appendix 5.2. Fig. 21 shows a comparison of measured contours and optimally fitted model contours.

2.3.4 The equilibrium classes of shell shapes

The previously described procedure identifies the fitted shape parameters *h, p, k* corresponding to any shell and thus the complete algorithm to determine the equilibrium class of any *individual turtle* (as given in Appendix 5.2). In order to analyse *global trends*, we introduce simplified, lower dimensional (two- and one-parameter) models, trading accuracy of individual predictions for visual and conceptual simplicity.

As a first step we eliminate parameter *k*. We consider the [*h,k*] projection of the [*h,p,k*] space (Fig. 22.A). Measured turtles are marked by squares. Linear regression to the data points (continuous lines) reveals $\bar{k}(h) = 0.90h - 1.01$. Straight dashed lines $k^{\pm}(h) = \max(0, \bar{k}(h) \pm 0.2)$ mark the approximate upper and lower envelope of the data points. Fig. 22.B shows the [*h,p*]
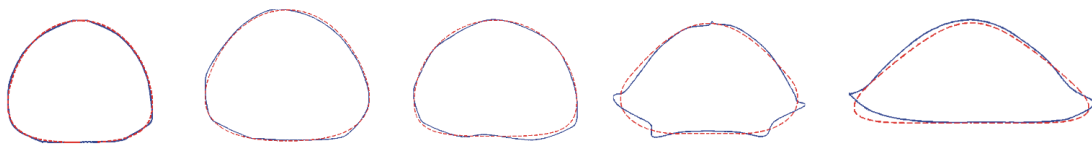
Fig. 21. Model fit to real contours. From left to right: Geochelone elegans (number 1 in Appendix 5.2), Stigmochelys pardalis (number 11), Chelonoidis nigra (number 20), Cuora amboinensis (number 26), Chelonia mydas (number 30). The model fits well to terrestrial species with highly domed cross-sections (three contours on the left side), but less so to flatter, semi-aquatic and aquatic turtles (two contours on the right) where sharp edges appear, improving swimming performance.

projection of the $[h,p,k]$ space. In addition to marking the measured turtles, we also fitted a line to the data points yielding $\bar{p}(h) = 2.59h - 1.51$ (continuous line) and we determined the equilibrium class of each $[h,p]$ point by assuming for k each of the two extreme values $k = k^+(h)$ and $k = k^-(h)$. Dashed lines depict the boundaries between stability classes S_1, S_2, and S_3 for both cases. The grey shading between the two sets of boundaries shows regions of the $[h,p]$ space where the equilibrium class of an individual may depend on k. Domain „X" corresponds to parameter values not compatible with the model. As we can observe in Fig. 22.B, not even these extreme changes of k have substantial influence on the borders. Few marks appear in the ambiguous grey zone between the two sets of boundaries; the stability class of the majority of individual turtles is predicted correctly by a simplified, two-parameter (h,p) model, yielding the following observations:

- although class S_1 is represented by a rather small domain (small ranges both for h and p), nevertheless, tall turtles are remarkably close to S_1, i.e. they tend to be *monostatic*.

- flat turtles fall into S_2, and the majority of medium turtles falls into S_3.
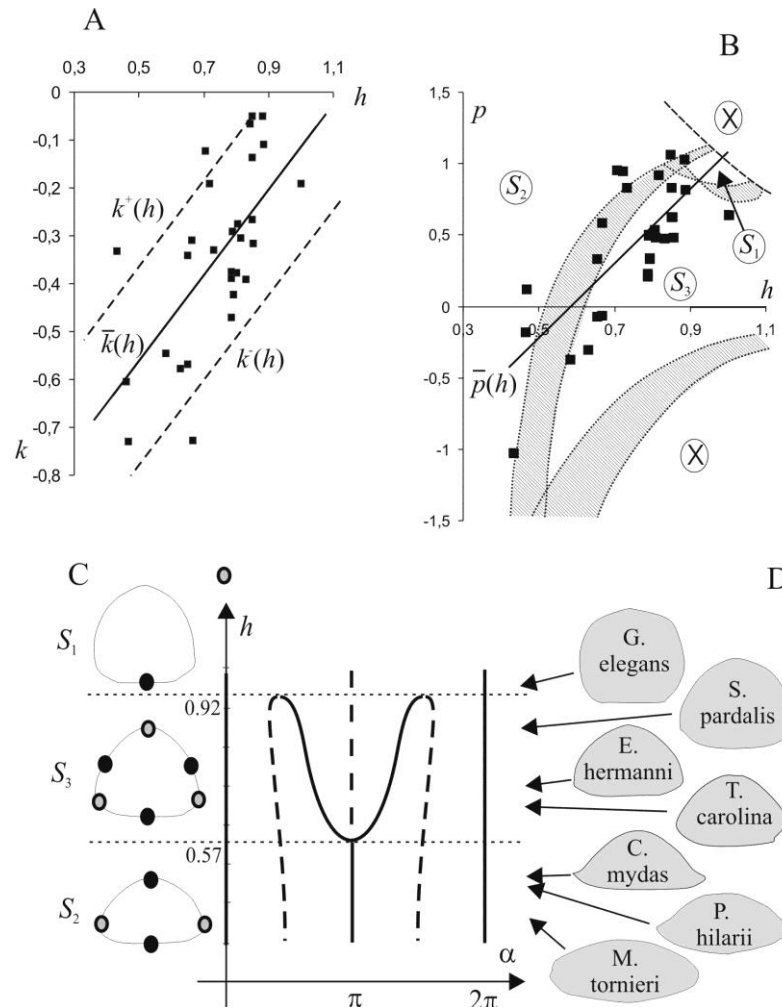
Fig. 22. A,B: fitted parameter values of measured turtles C: angular positions α of equilibria along the main cross-section of the turtle shell as function of *h* in the one-parameter model. Equilibria in all classes marked along main transversal cross section by black (stable) and grey (saddle point) circles. Unstable equilibria off the main cross-section (near head and tail) are not indicated. D: fitted *h* value and contour of some measured individuals.

27

Next we further simplify our model to better understand global trends. Strong linear correlation between the parameters (corr<h,p>=0.73; corr<h,k>=0.64) suggests that a one-parameter (h) model family is sufficient to approximate the geometry. From the biological point of view, this implies that a single, visually significant parameter (the height/with ratio h) basically determines the stability class, and, as we will see soon, the righting strategy. Fig. 22.C illustrates the angular locations of equilibria along the main cross-section as h is varied in the one-parameter model (i.e. in the case of $p = \bar{p}(h)$ and $\overline{k = k(h)}$). The figure reveals three equilibrium classes as well as a classical pitchfork bifurcation. The reduced model illustrates the transition between three different types of turtles:

- individuals below h=0.57 tend to have two stable equilibria, one on the plastron and one opposite, on the carapace,

- as h increases, two additional stable equilibria emerge on the back and their distance is growing monotonically,

- the additional stable equilibria vanish at h=0.92, where monostatic turtles appear.

A closer look at an actual shell (Fig. 18.D) explains why monostatic bodies may exist in three dimensions in contrast to 2D: the front and the back part of the shell are lower than the main cross-section, thus the center of gravity G of a complete turtle body is closer to the plastron than the geometric center of its 'main' cross-section. Indeed shell shapes resemble to some extent the shape depicted in Fig. 5.B. While this simple qualitative observation is intuitively helpful, it certainly does not account for the *quantitative* agreement between model parameters of highly domed turtle shells and monostatic bodies.

It is also worth pointing out that turtles in S_1 have multiple unstable equilibrium poses, i.e. they are not mono-monostatic. One unstable pose is represented by a point along the main cross-section (cf. Fig. 22.C), and due to their elongated shapes, there are at least two more unstable poses represented by points near each end of the body.

2.3.5 Ecological consequences

The *energy balance* of righting on a horizontal surface reveals a close relationship between the equilibrium class and the righting strategy (for the latter, see [6] [140]). Below we describe a qualitative model, which yields some insight into this relationship.

Non-monostatic turtles have to overcome a primary potential energy barrier (*primary energy deficit D_p*, Fig. 23.A) due to the unstable equilibrium at the turtle's side.
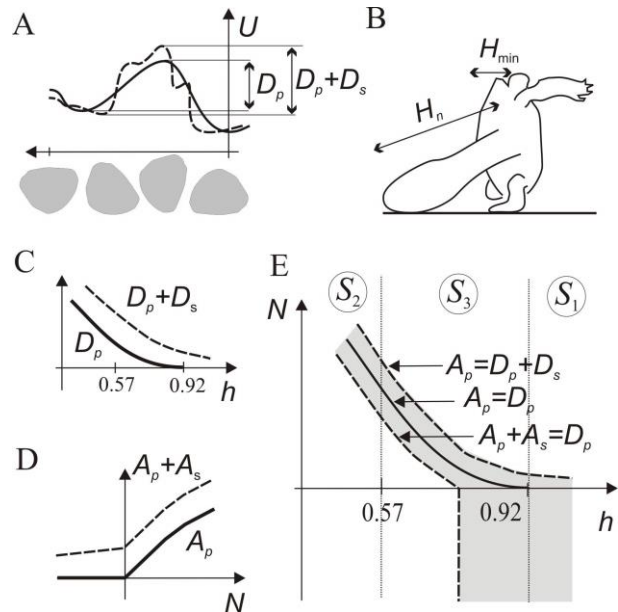
Fig. 23. Energy balance of righting. A: Illustration of primary (D_p) and secondary (D_s) energy deficit of rolling turtle due to potential energy barrier between stable equilibria. Continuous/dashed line denotes potential energy U of perfect/imperfect shell normalized by body size. B: schematic frontal view of a righting turtle. C: Primary (D_p) and secondary (D_s) energy deficit as functions of h. D: primary and secondary available biomechanical energy as functions of the excess neck length N. E: energy balance curves in the [h,N] plane.

Additional, secondary deficit (D_s) results from shell imperfections (Fig. 23.A). Turtles with high energy barriers use primarily their necks for righting [140], thus the *excess neck length N* is the dominant factor of *primary available biomechanical energy* (A_p). The neck's excess length (Fig. 23.B) is defined as $N=(H_n- H_{min})/H_{min}$, i.e. scaled difference between the neck's length (H_n) and the distance (H_{min}) from the neck's base to the top of the carapace. Additional, secondary energy (A_s) is generated by limb- and head-bobbing, ventral orientation of the head or feet (to move center of gravity), and nearly horizontal pushing with the legs (using friction) [6]. The latter often results in rotation around a vertical axis during righting efforts, helping the feet find support.

Here we make two simple assumptions:

- $D_p(h)$ is a monotonically decreasing function, which vanishes for monostatic (S_1) turtles (Fig. 23.C);
- $A_p(N)$ is a monotonically increasing function if $N>0$, and $A_p=0$ for $N\leq0$ (Fig. 23.D).

Energy balance curves, i.e. solutions of $A_p(+A_s)= D_p(+D_s)$ can be plotted in the plane of geometric parameters R and N. With the two assumptions listed above, the balance curves become similar to the sketch of Fig. 23.E. The region enclosed by the curves (grey fill) is narrow for flat turtles and it becomes wide for high ones. In the grey region secondary components (D_s, A_s) determine righting success. To the right of the grey region, righting is successful even in the presence of secondary deficits (shell irregularities). To the left, righting is unsuccessful even if secondary available energy (from head-bobbing, etc.) is used. This picture leads to the following qualitative conclusions:

For flat turtles (*h* under ~0.6, Fig. 24.A,) inside S_2, the curves form a *narrow band*, indicating that the primary parameters *h* and N dominate righting fitness. The
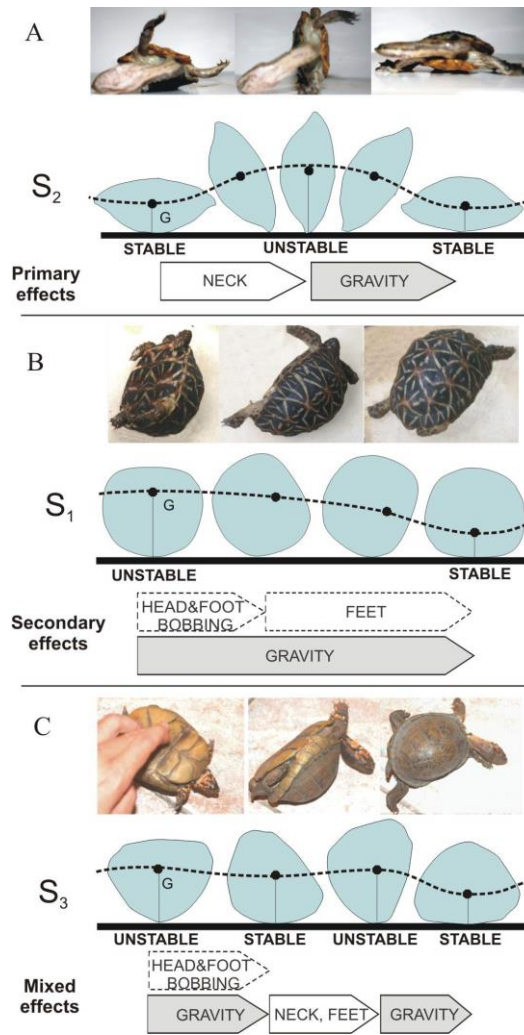
Fig. 24. Righting strategies. Each strategy is characterized by the typical shape of the rolling main cross-section (grey contours) as well as the orbit (dashed line) of the center of gravity G. Arrows denote key elements of righting, dashed arrows apply in presence of secondary energy barriers. A: flat turtles (*h*<~0.6 inside Class S_2, photo: Hydromedusa tectifera): high primary energy barrier between stable and unstable equilibria is overcome by primary biomechanical energy resulting from vertical push with neck. Righting fitness is determined by primary geometric parameters (height/width ratio *h*, excess neck length *N*). B: tall turtles (*h*>~0.8, inside or close to monostatic Class S_1, photo: Geochelone elegans): small, secondary energy barriers (resulting mainly from shell imperfections) are overcome by secondary sources of biomechanical energy: head- and foot-bobbing, push by feet. C: medium turtles (~0.6< *h* <0.8, inside or close to Class S_3, photo: Terrapene carolina): in the first phase of roll, secondary barriers are overcome by dynamic (secondary) energy, in the second phase, the primary energy barrier is overcome by primary energy (push with neck, feet). Photos by G. Domokos.

associated righting strategy is based on primary energies: righting is accomplished via a strong vertical push with the neck, lifting the turtle sufficiently to overcome the primary energy barrier. Most aquatic and semi-aquatic turtles, e.g. side-necked turtles (Pleurodira), snapping turtles (Chelydridae), mud turtles (Kinosternidae) follow this strategy. Shell irregularities are unimportant in this case.

Tall turtles (h above ~0.8, Fig. 24.B,) inside or close to the monostatic class S_1 usually have shorter necks than their carapace heights, i.e. $N<0$. Thus their h, N values are in the *wide grey zone* between the curves of Fig. 23.E, indicating the dominance of secondary effects in righting fitness. The *associated righting strategy* is based on secondary energies: Righting either starts spontaneously [6] or it is accomplished by dynamic motion of the limbs, to overcome small shell imperfections. Subsequently, when the plastron is already close to vertical and the legs reach the surface, horizontal pushing with the legs (using friction) produces additional moments to overcome secondary energy barriers. This is the primary strategy of highly domed terrestrial tortoises with short necks and rounded cross-sections, such as Geochelone, Stigmochelys, Astrochelys, and some Terrapene and testudo species.

For medium turtles (~0.6 $<h<$~0.8, Fig. 24.C) in or close to S_3, the energy diagram shows regions of both types: the three curves initially form a narrow band and subsequently diverge. The *associated righting strategy* is composed as a *mixture* of the previous two: if placed on the middle of the back, the turtle starts rolling spontaneously, assisted by dynamic limb and head motion to overcome shell irregularities (similar to class S_1) until it reaches stable equilibrium. From there, the successful righting strategy is based on a vertical push with the neck (similar to class S_2), accompanied by pushing with the legs. Many tortoises (e.g. Psammobates, many

Testudo, and Terrapene species) belong to this group.

Due to strong correlation between model parameters, by measuring the h=height/width ratio one can often correctly predict the righting strategy (Fig. 22.B,D). Nevertheless a *quantitative* analysis of the individuals' energy balance would require more details about the neck, the shell imperfections and other factors.

2.3.6 Discussion and ongoing works

Using theoretical modeling as a primary tool, we made quantitative predictions on optimal shell morphology for self-righting in a terrestrial environment by identifying a narrow monostatic range of the height/width ratio. The morphological analysis of actual shells revealed that the height/width ratio of highly domed species (G. Elegans, G. Radiata) is near the minimum for monostatic shapes ($h\approx0.9$), indicating an optimal tradeoff between self-righting ability and other factors penalizing increased height (e.g. decreased stability). The shape parameter p is also in the optimal range for these species ($0.8<p<1.1$). Thus, we may conclude that the advantage of being close to monostatic not only determines the height/width ratio, but it probably influences the exact shape (e.g. roundedness).

Our model also addressed the role of irregularities in the shell shape. Interestingly bad nourishment often produces shell imperfections [84] [189] decreasing the chances of successful righting, according to the presented theory.

Our own preliminary experimental investigation of righting strategies was in agreement with the model predictions Recently, these predictions have also been confirmed by more detailed experiments, which demonstrated the correlation between righting success and

morphological variations of individuals within a single species [73] [72] [154].

Many other factors have been identified to affect the shape of turtles. Flat shells with sharp and smooth edges are advantageous, respectively, for swimming [41] and for digging [191]. On the other hand, *increased shell height* was found to offer better protection against the snapping jaws of predators [133]; it also protects from desiccation and improves thermoregulation [35]. Many turtles exhibit sexual dimorphism, which is traditionally explained by need for the female's shell to enclose the eggs [24], however self-righting ability also plays here a role as males often tumble during fights [154]. Recently, more and more of these works begin to use quantitative models of shell morphology [24] [39] [141] [142] [151]. For example, the shell model described here was also used for the determination of the habitat of extinct turtles based on the shapes of fossilized shells [12].

2.4 MONOSTATIC BEHAVIOR IN CAGES, WITH APPLICATION IN AUTOMATED MANUFACTURING

In the previous two sections, we dealt with the theoretical analysis of the static equilibria of rigid bodies on a *flat, horizontal surface* with emphasis on monostatic shapes, and with a biological application. The forthcoming section contains an application-oriented discussion of monostatic behavior of objects inside a frictionless *circle* (2D) or *sphere* (3D). First, we motivate the investigation of this question by discussing the role of monostatic behavior in the field of industrial part feeding (Sec. 2.4.1). The specific questions addressed in Sec. 2.4 are chosen with an eye on this potential application, to which we return several times. The first step of the theoretical analysis in Sec. 2.4.2 is the generalization of the geometric approach to finding static equilibria on a horizontal support (Sec. 2.1) to a similar approach to equilibria in round cages. We also demonstrate the key observation that almost all objects become monostatic if they are enclosed in a sufficiently tight cage. Sec. 2.4.3 is devoted to the description of a computational algorithm, which determines the range of cage sizes corresponding to monostatic behavior. In addition, we also describe how full *orientational* ordering can be achieved in the 3D case, despite the fact that spherical cages can only ensure the uniqueness of a stable *pose* of equilibrium. The theoretical results are complemented by the theoretical and experimental analysis of an L-shaped part in Sec. 2.4.4. Remaining challenges of practical application in the field of part feeding are discussed in Sec. 2.4.5.

2.4.1 Part feeding with cages

A Industrial part feeding

Parts used in automated assembly lines are often available in bulk and are oriented by feeders before entering the assembly line. Traditionally, the parts are dropped to a horizontal surface (e.g. a tray, a vibratory bowl or a conveyor belt) and settle in one of the equilibrium poses. This process is sometimes referred to as 'pose selection'. After coming to rest, they are further processed by active manipulators (e.g. vibrated trays with depressions [44]; grippers [34], [159]; distributed manipulators [46], [157], [22], [179]; actively tilted trays [56]; throwing devices [101]) or passive physical barriers, such as

fences [1], [18], [19], [188] traps [17], [69], pins [194] or 'blades' [70]. Some of these devices change the orientations of parts, whereas others are designed to sort out badly oriented ones for recycling.

The current level of technological development offers many intelligent ways for the reorientation of parts (sensors combined with flexible manipulators). Nevertheless, when massive quantities of cheap parts have to be processed, simple and durable feeders are preferable. As a consequence, most industrial part feeders apply simple, sensorless methods, exploiting mechanical properties of the parts.

Although the core mechanism of a feeder is reused across different parts, the sorting and orienting devices require part-specific design. Traditional methods of designing an efficient feeding line for a new part are slow and expensive. Researchers have found two directions during the past two decades to facilitate feeder design. The first one is algorithmic planning and optimization [1] [15] [17] [18] [19] [195], to which we will return in Chapter 3. The second is developing flexible or universal orienting devices [22] [44] [157] [179], which require little or no part-specific adaptation. The new method introduced here aims to be a step towards the second solution.

B   Universal feeders in 2 and 3 dimensions

We follow a long tradition of distinguishing between planar and spatial part-feeding methods. Despite all real parts being three-dimensional, feeding methods of planar objects are often used for illustrative purposes, and they also have direct practical applications: we have pointed out that the majority of the orienting devices can only rotate parts about a vertical axis [147], without changing their initial pose. Rotating a part about an axis of fixed direction is inherently a planar problem, which can be solved using insights from a purely planar

model of part feeding (see point D below for a specific example).

Universal part feeders in 3D do not exist at this time, nevertheless planar universal part feeders have already been proposed in the late 1990's [22] [156] [157] [161]. Dense grids of small manipulators were abstracted as programmable, planar force fields. Parts were placed on top of the arrays. It was demonstrated that certain force fields rotate an arbitrarily shaped planar part into one or two orientations regardless of its initial configuration. These feeders did not become popular in the industry, because their complexity, and discrepancies between their real behavior and the idealization of programmable force fields.

A different approach to planar, universal part feeding was proposed by [179]: the parts were placed on a rigid, horizontal tray. The frictional forces induced by a carefully designed small-amplitude periodic motion of the tray rotated arbitrarily shaped parts into a uniform orientation. This method requires a high-precision 6 degree-of-freedom positioning system.

C   A new paradigm of part feeding

We have seen that some objects are indeed monostatic on a horizontal support. This is an ideal situation, in which the task of part feeding becomes trivial in 2D. In 3D, achieving uniform orientation still poses a challenge, nevertheless the task of part feeding becomes much easier than for general objects (see point D below for more details). Nevertheless, feedability is at best a secondary demand, thus parts are usually not designed to be monostatic. This is how one naturally arrives to the approach of optimizing the shape of the underlying support surface for feedability.

An important example of this approach is the industrial APOS feeder [86] in which parts are captured and oriented by an array of part-specific, identical depressions designed by trial and error. Motivated by

the APOS, Moll & Erdmann [110] investigated systematically, how planar parts can be pushed towards monostatic behavior by optimizing the shape of the underlying support curve. They considered the behavior of parts after being dropped from a sufficient height. For many parts, they could design support curves, for which the parts came to rest with high probability in a unique orientation. Nevertheless they could not achieve perfect monostatic behavior via this approach.

Our new method uses a particularly simple setup. Individual parts are enclosed in round, rigid cages (circles in 2D or spheres in 3D). Vibration of the cage is assumed to replace dry friction with an appropriate velocity-dependent damping such that all parts come to rest in stable frictionless equilibrium orientations (2D) or poses (3D), corresponding to local minima of the potential energy function induced by gravity. This setup can be applied as a part feeder if the object shows monostatic behavior in the cage, and as we show in Sec. 2.4.2, rigid objects have a strong tendency to become monostatic in round cages. Hence, round cages can be interpreted as a perfect theoretical solution to the problem raised by Moll & Erdmann. A similar idea inspired the planar universal feeder [156] [22], which used a force field mimicking a tight, compliant circular cage around the part.

The new method does not yield a universal feeder, because the radius of the cage has to be adapted to the part. Nevertheless the simplicity of the part-specific ingredients makes the adaptation process to a new part particularly easy.

D Complete orientational ordering in three dimensions

In 2D, a monostatic part rotates spontaneously to a uniform orientation, whereas in 3D, only uniform pose is
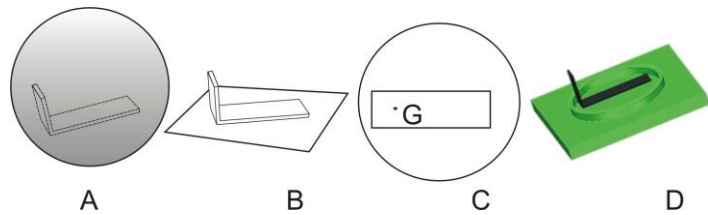
Fig. 25. The steps of achieving complete orientational ordering with cages.

achieved. An auxiliary step is necessary to rotate three-dimensional parts already in uniform pose to a uniform orientation. The auxiliary step is analogous to a planar part feeding task, because if parts are in uniform pose, then arriving to uniform orientation requires rotations about a vertical axis only. Various planar part feeding methods can be adapted to this task. The steps of a possible realization with a planar cage feeder are sketched below

1. Rotate the parts into uniform pose using a 3D cage feeder (Fig. 25.A).
2. Place the parts to a horizontal plane such that their poses remain identical. Their new pose may differ from the one in the cage, in particular, it should be a stable equilibrium on the plane (Fig. 25.B).
3. Consider a virtual planar part defined as the convex hull of the contact points of the object. The vertical projection of the center of mass G to the plane should be used as center of mass of the virtual planar part (Fig. 25.C).
4. Find an appropriate cage size α^* for this virtual planar part and enclose the contact points of the part in a vertical, sufficiently short cylinder of radius α^* as in Fig. 25.D.
5. Tilt the plane together with the cylinder by an angle small enough to avoid toppling of the part.
6. Inside the tilted ring, the potential energy function induced by gravity has a unique local minimum point.

2.4.2 Equilibria in round cages

We begin by discussing the behavior of rigid bodies enclosed in *tight* circles or
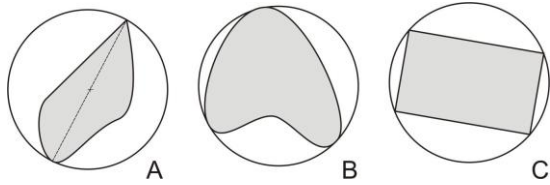
Fig. 26. The smallest enclosing circle of a bounded planar object has typically 2 (A) or 3 (B) points of contact with the object. In special cases (including objects with certain symmetries), the number of contacts may be higher (C).

spheres. Then we introduce a generalization of the notion of the convex hull, which will be used to find conditions of equilibrium and stability for objects in a round cage of arbitrary radius. Throughout the analysis, the planar case is discussed first, and the extension to 3D is presented thereafter.

A   Equilibria of an object in a tight cage

Every bounded, *planar* object has a unique smallest enclosing circle, which has 2 or 3 contact points with the object typically, but more than 3 contacts in degenerate cases (Fig. 26). In a cage having the shape and size of this circle, the motion of the object is restricted to pure rotation about the center O of the circle. If the walls of the cage are frictionless, gravity acts in the plane of the cage, and the center of gravity G of the object does not coincide with O, then the object has a unique potential energy minimum (G vertically below O), corresponding to a unique stable orientation. Analogously, 3D objects have a unique smallest enclosing sphere with 2 to 4 contact points typically. In a cage of this shape, they have a unique stable pose.

In special cases, including all planar objects with symmetries of order 3 or higher (Fig. 26.C), the center of the cage and the center of mass of the object coincide, and the potential energy of the object becomes invariant under rotation. Such objects do not orient themselves spontaneously in a tight, round cage. In practical applications, such an unwanted coincidence can be

avoided by changing the mass distribution of the object.

Theoretically, one could create a part feeder by placing individual parts into tight cages. Nevertheless this approach has several disadvantages. Most importantly, fitting a part with unknown initial orientation into a tight cage is itself a highly nontrivial manipulation task. In addition, every part requires a unique cage size. Finally, elongated planar parts maintain contact with the cage at a pair of opposing points of the circle (Fig. 26.A). The corresponding frictionless contact forces are collinear, i.e. they are theoretically insufficient to balance the object. In practice, such parts may exhibit very large contact forces and non-negligible friction-related effects. These may cause physical damage or the emergence of unexpected equilibria. The same problem arises for 3D parts with 2 or 3 contacts with the cage. All problems outlined above vanish if the cage used is larger than the smallest enclosing circle or sphere. This is why we will develop a computational algorithm in Sec. 2.4.3 to determine the exact range of cage size in which the monostatic behavior of polygonal (2D) or polyhedral (3D) parts is preserved. In preparation to this task, we review an important mathematical tool, and develop conditions of equilibrium in round cages.

B   Basic properties of α-hulls

We have seen that equilibria on a horizontal surface are identified by analysis of the convex hull of an object. The convex hull can be defined as the intersection of all half-planes (2D) or half-spaces (3D) containing the object. This definition has a natural generalization in which half-spaces are replaced by finite-sized balls (i.e. circles in 2D or spheres in 3D):

Definition 2.4.1*: the α-hull of an object is the intersection of all balls of radius α enclosing the object.*

A slightly different definition of the α-hull is extensively used in the context of associating object shapes with point clouds [54]. The existence of the α-hull requires that α exceeds the radius α_0 of the smallest enclosing ball of the object. For $\alpha \to \alpha_0$ the α-hull becomes identical to the smallest enclosing ball, whereas the limit $\alpha \to \infty$ of the α-hull is the convex hull.

Fig. 27. The α-hull of a triangle for 2 different values of α.

The α-hull of a *planar polygon* is a convex set (Fig. 27). with piecewise smooth boundary, which consists of arcs of circles of radius α (α-edges), joining at vertices. The minimum number of vertices and α-edges is 2.

The vertices of the α-hull form a subset of the vertices of the convex hull. The α-edges are always smaller than a semi-circle, see proof in Appendix 5.3.1. Analogously, the α-hull of a *spatial polyhedron* (Fig. 28) typically consists of

- vertices forming a subset of the vertices of the convex hull.
- α-edges: portions of *spindle tori* obtained by revolving circles of radius α around an axis joining 2 vertices of the α-hull. Despite their names, α-edges are surfaces rather than 1-dimensional manifolds but they shrink to line segments in the limit of $\alpha \to \infty$.
- α-facets: spherical triangles of radius α bounded by 3 vertices and 3 α-edges.

The minimum number of vertices is 2. An α-hull with two vertices (Fig. 28.B) has no α-facets and its single α-edge is a full spindle torus.

C Equilibria in round cages of arbitrary radius

For *planar objects*, an important difference between equilibria in a round cage and those on a horizontal line is the lack of translation symmetry of the round cage, which implies isolated configurations of equilibrium typically. Apart from this difference, the characterization of equilibria in a round cage is highly similar to the characterization of equilibria on a horizontal support, which is described in Sec. 2.1.3. The similarity is illustrated by Fig. 6.A and B. If a planar part rests in equilibrium under the influence of gravity, then there must be contact between the object and the cage. Thus the cage appears as a circle *t* of radius α tangential to the α-hull ℍ. Let P and C denote the lowest point of the cage, and the "contact set", i.e. the intersection of *t* with ℍ; and let κ be the radius of curvature of the α-hull at P. The geometric conditions of stable equilibrium are summarized in

Lemma 2.4.2: *a configuration corresponds to equilibrium if (1) G lies on the vertical*
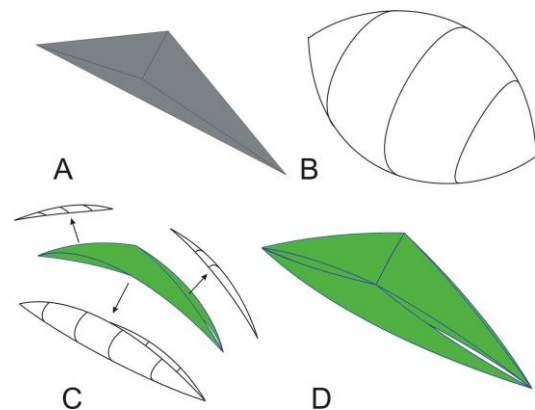
Fig. 28. An elongated tetrahedron (A) and its α-hull at three values of α (B-D). For small α (B), the α-hull consists of a single α-edge, with the shape of a spindle torus. For intermediate values of α (C), the α hull consists of two α-facets (shaded spherical surfaces), and 3 α-edges (white toroidal surfaces lifted from the α-hull). For larger α (D), the α-hull becomes similar to the convex hull: it has has 4 α-facets (shaded surfaces) and 6 α-edges (removed from the picture)
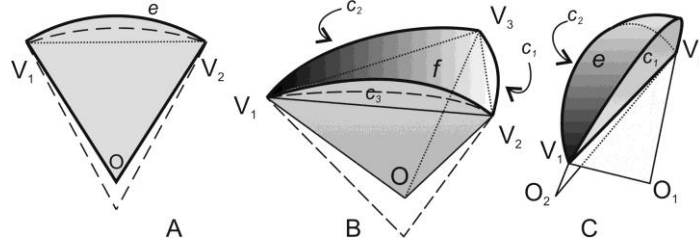
Fig. 29. Resting on the planar α-edge *e* (panel A); spatial α-facet *f* (B); or spatial α-edge *e* (C) is stable if the center of mass of the object is in the corresponding grey area (A) or volume (B,C). Points V_i are the vertices spanning the α-edge or α-facet in question. O is the center of *e* (A) and *f* (B). In panel C, O_1 and O_2 are centers of the two adjacent α-facets. Invisible lines are printed as dotted. Dashed lines in A and B show how the boundaries of the grey area/volume move if α is increased.

line through P and (2) P belongs to C. Moreover, the equilibrium is stable if

$$|GP| < min[\alpha, (\kappa^{-1} - \alpha^{-1})^{-1}] \qquad (18)$$

Lemma 2.4.2 is proven in Appendix 5.3.2. For polygonal planar objects, *C* is either a vertex or an α-edge of Ħ. Thus, there are two types of equilibrium: resting on an α-edge of the α-hull or on a single vertex of the α-hull. In the first case, $\kappa = \alpha$ and by (2), the equilibrium is stable if $|GP| < \alpha$. In the second case, $\kappa = 0$ implies instability. For a given α-edge *e* of the α-hull, a configuration satisfying the three conditions of ***Lemma 2.4.2*** exists if the center of mass G of the object is in the circular sector OV_1V_2 determined by the α-edge (Fig. 29.A).

The characterization of equilibria in a *3-dimensional* spherical cage is analogous to the planar case. Remarkable differences include the following:

- there are isolated equilibrium poses instead of isolated configurations due to rotational symmetry of the cage.
- polyhedra have three types of equilibrium: resting on an α-facet, on an α-edge, or on a vertex of the α-hull.
- Resting on a given α-facet *f* is a stable equilibrium if G is in the spherical sector determined by *f* (Fig. 29.B).
- Resting on a given α-edge *e* is a stable equilibrium if G is inside a region bounded by planar boundaries of the two stable regions associated with the adjacent α-facets and the toroidal

surface of *e* (Fig. 29.C). In the special case of an α-edge without adjacent α-facets (as in Fig. 25.B) the stable region is bounded only by *e*.

2.4.3 Algorithmic cage size selection

This section is devoted to the description of a computational algorithm, which determines the range of cage sizes in which a polygonal or polyhedral part is monostatic.

A naïve approach in 3D is to test each triple of vertices and each pair of vertices one by one as contact point candidates. For each set of contact point candidates, a range of the cage size can be determined such that all other vertices of the part are inside the cage, and the position of the center of mass satisfies the conditions of stable equilibrium. Such an algorithm requires $O(n^4)$ processing time, where *n* is the number of vertices of the object. The efficiency of the naïve algorithm can be improved by constructing the furthest-point Voronoi tessellation of the vertex set (complexity: $O(n^2)$), which yields all pairs and triples of vertices, which can touch the wall of the cage simultaneously. Here we describe another algorithm also with $O(n^2)$ complexity. The algorithm is based on tracking the topological evolution of the α-hull as α is increased gradually.

If α is varied, the structure of the α-hull, and the number of equilibria may change in various ways. A complete list of transitions is given below. The list is used by our cage size selection algorithm.

To understand the *planar case*, consider again an α-edge e connecting two vertices (V_1, V_2) as in Fig. 29.A. We have seen that resting on this α-edge is a stable equilibrium if G is in the sector OV_1V_2. If α is increased, then the arc e becomes flatter and O moves away from the V_1V_2 line (dashed lines in Fig. 29.A), and thus one of the following events may happen:

- one of the OV_1, OV_2 line segments crosses G such that G enters the grey region. In this case, resting on e becomes stable. The position of the arc e also changes during variation of α, nevertheless it never crosses G, because G remains in the interior of the α-hull for all α.
- the α-edge e crosses another vertex of the object. In this case, the new point becomes a vertex of the α-hull, dividing the edge e to two parts as in Fig. 27.

The two events described above are the only ones that change the structure of the α-hull or the number of stable poses. None of these events cause the number of stable poses to decrease, which proves

Theorem 2.4.3*: the number of stable equilibria of a planar object is a monotonically increasing function of* α.

We have seen in Sec. 2.4.2 that the case of *3 dimensions* is more complex because the surface of the α-hull is composed of α-facets and α-edges; moreover resting on α-facets and α-edges may both be stable. Resting on an α-facet f is stable if G is within the region bounded by the spherical surface f, three triangles OV_iV_j, and three circular caps (c_1, c_2, c_3) coplanar with the triangles (Fig. 29.B) As α is increased, the spherical triangle f becomes flatter and O moves away from the $V_1V_2V_3$ plane (dashed lines in Fig. 29.B). The following events may happen to an α-facet:

- One of the triangles OV_iV_j crosses G. The direction of crossing depends on the shape of triangle $V_1V_2V_3$: if its interior angle opposite the edge V_iV_j is acute, then G may enter the stable region, whereas if it is an obtuse angle then G may leave the stable region. Accordingly, resting on the α-facet becomes or ceases to be stable.
- One of the circular caps crosses G. The other side of the cap belongs to the stable region of an adjacent α-edge, hence the number of stable equilibria does not change.
- The surface f may not cross G because G remains in the interior of the α-hull.
- A vertex of the object crosses the α-facet. In this case, one new vertex and 3 α-edges are added to the α-hull, dividing the α-facet to three parts (Fig. 30.A).

Resting on a three-dimensional α-edge e is stable if G is within a region bounded by the toroidal surface of e, and two circular caps

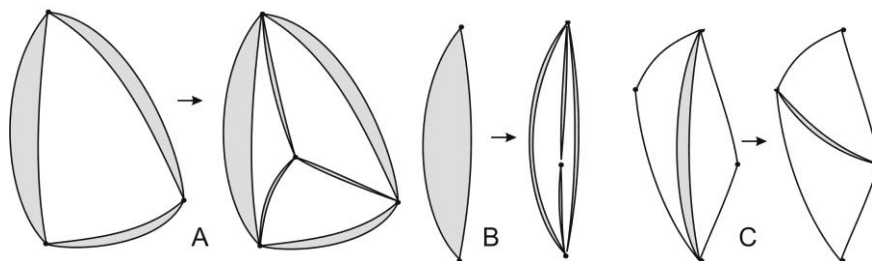**Fig. 30. Topological changes of the α-hull under variation of α. Each sketch shows a part of the boundary of a 3D α-hull. White and grey areas represent α-facets and α-edges, respectively.**

(c_1, c_2), as in Fig. 29.C. If α is increased, the surface of e becomes flatter, while the angle between the planes c_1 and c_2 may increase or decrease. Events associated with e are the following:

- G crosses one of the caps, thus resting on the α-edge becomes or ceases to be stable. As we have seen, the opposite side of the cap belongs to the stable region of an adjacent α-facet, hence the number of stable equilibria does not vary. The surface e also moves, nevertheless G may not cross e as it always remains in the interior of the α-hull.
- e crosses a vertex of the object, which becomes a new vertex of the α-hull, creating two more α-edges and 2 new α-facets (Fig. 30.B).
- The angle between planes c_1 and c_2 becomes 0 if α equals the radius of the sphere fitted to the four vertices of the two adjacent α-facets. In this case, e disappears, while a new α-edge is born (Fig. 30.C).

It is worth noting that one of the events associated with α-facets results in the elimination of a stable pose as α increases. Hence, ***Theorem 2.4.3*** does not generalize to three dimensions.

B Algorithmic selection of cage size

According to ***Theorem 2.4.3***, every *planar object* is monostatic if and only if the cage size is within an interval bounded from below by the size of the smallest enclosing circle. The interval extends to infinity for objects which are monostatic on a horizontal supporting surface. The interval may shrink to a single point if the critical value of α associated with the birth of a new equilibrium coincides with α_0. Such a coincidence is non-generic except for objects with certain symmetries. The upper endpoint of the interval can be found by gradually increasing α, and by tracking topological changes of the α-hull, until the emergence of multiple stable equilibria.

Specifically the steps of the algorithm for planar parts are the following.

1. Construct the smallest enclosing circle. The points of contact with the object become the vertices of the α-hull for $\alpha \rightarrow \alpha_0$ and there are α-edges between each pair of adjacent points of contact. The processing time of this step is O(n) [108].
2. For each α-edge, find the critical value of α, at which resting on the α-edge becomes a stable equilibrium. Complexity: O(1).
3. For each α-edge and each vertex of the object not included in the vertex set of the α-hull, find the critical value of α, at which the α-edge crosses the vertex. Complexity: O(n).
4. Find the smallest of the critical values identified in the previous steps. Complexity: O(n).
5. If the smallest critical value corresponds to the emergence of a stable equilibrium, exit the algorithm.
6. If the smallest critical value belongs to an α-edge-vertex crossing, then update the α-hull, calculate the critical values associated with the new α-edges, and return to step 4. Complexity: O(n)

The construction of the smallest enclosing circle is discussed in the literature [108], [186]. Steps 2 and 3 require elementary algebraic steps (e.g. finding the radius of a circle fitted to 3 points). For brevity, the equations solved during these steps are not presented. Each cycle of the algorithm requires at most O(n) processing time, and adds one vertex to the α-hull. Hence, the worst-case complexity of the algorithm is O(n^2).

In *three dimensions*, monostatic behavior may extend to multiple intervals of α because ***Theorem 2.4.3*** does not hold. The first step of the algorithm is finding the smallest enclosing sphere, for which efficient algorithms exist similarly to the planar case. In step 2, only α-facets are investigated, and critical values of α

associated with the emergence or disappearance of an equilibrium are determined. It has been shown in Sec. 2.4.3.A, that events associated with an α-edge do not change the number of stable poses. In steps 3 and 6, both α-edges and α-facets have to be considered. Step 5 is optional, because continuing the algorithm may uncover multiple intervals of α, where the object is monostatic. The worst-case complexity of the procedure remains $O(n^2)$.

2.4.4 Analysis of an L-shaped part

The cage size selection algorithm has been applied to the L-shaped part depicted in Fig. 31.A. This part has non-triangular facets, and it is perfectly symmetrical. To avoid computational difficulties, a random number drawn from a uniform distribution over the interval (-0.0005 0.0005) is added to the coordinates of each vertex. A MatLab implementation of the algorithm requires roughly 0.2 seconds to detect the critical cage size where the second stable pose emerges, and 1 second to identify all critical values of α.

The object has 5 stable poses on a horizontal plane, two of which are mirror images of each other (Fig. 31.B-E). If it is surrounded by its smallest enclosing sphere ($\alpha_0 \cong 1.146$) as a cage, a unique stable pose close to the

one in Fig. 31.B exists. As α is increased, 4 other stable poses emerge, which are close to the ones in Fig. 31.C-E, and none of the stable poses disappears. To estimate the effect of the initial random perturbation, the algorithm has been repeated 10 times with independent random numbers each time. The mean value and the standard deviation of critical cage sizes associated with the emergence of new stable poses are also given in Fig. 31. The emerging stable poses are not perfectly identical to the ones in the figure, because as α is varied, existing stable poses of the object may change. Our results indicate that this object is monostatic for $1.146 < \alpha < 1.243$.

To illustrate the second phase of three-dimensional orientation (discussed in Sec. 2.4.1.D), assume that the object rests on a horizontal surface in the pose of Fig. 31.B. The convex hull of the contact points is a 2 by 1 rectangle, and the projection of G is in an asymmetrical position. Due to the simple shape, the critical cage sizes can be determined without using a computer. The smallest enclosing circle is of radius $5^{1/2}/2 = 1.031$, and the virtual planar object is monostatic for $\alpha < 1.064$.

A simple experiment has also been performed to illustrate the behavior of this part. The setup (Fig. 32) includes a hollow plexiglass ball of internal diameter 154 mm, attached to an eccentric rotating mass (ERM) vibration motor (part of a hand-held massager) with vertical axis of rotation. The amplitude of the vibration is controlled by a compliant connection of adjustable size

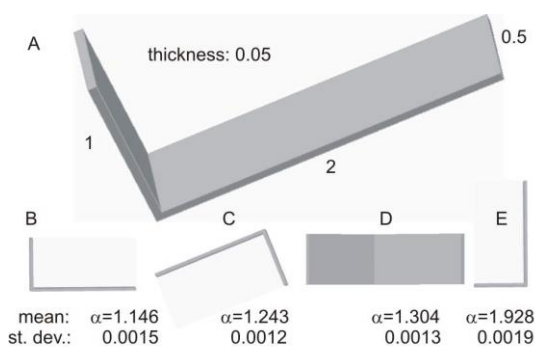**Fig. 31.A: an L-shaped part. B-E: stable poses of this object on a horizontal surface with mean and standard deviation of the critical values of α, where these stable poses emerge in a spherical cage.**
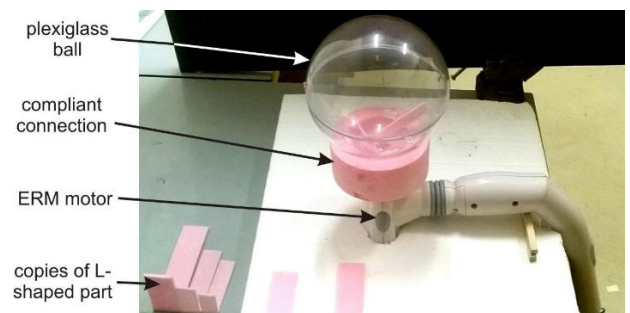
Fig. 32. The experimental setup
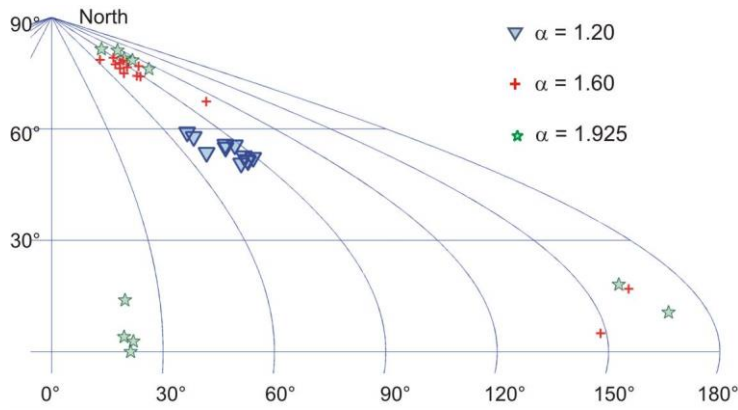
Fig. 33. Sinusoidal projection of a quarter of pose space (see Fig. 1) and experimental results with three different cage sizes

between the ball and the motor. The L-shaped part has been manufactured in three sizes. The length unit of Fig. 31 corresponds to 64 mm, 48 mm, and 40 mm for the three sizes. The corresponding dimensionless cage sizes (α) are 1.20, 1.60, and 1.925. Hence, theory predicts monostatic behavior for the largest object, and four stable poses for the other two.

Each part has been placed 12 times in the cage with random initial configuration, and the final poses after 8 seconds of vibration have been measured. Poses have been reconstructed from measurements of apparent angles between the vertical and edges of the objects in photographs (details omitted).

The results are depicted in Fig. 33. The experiment confirmed the prediction that the largest part always reaches the same pose, whereas multiple stable poses are reached by the other two parts[1]. The generation of random initial conditions has not been standardized, hence the measured probability distributions of final poses are not representative. Several theoretically stable poses have not been reached at all during tests with random initial conditions. One of these poses appeared unstable in the experiment, which is probably a consequence of the relatively large vibration amplitude, enabling the part to

escape from marginally stable poses. Other stable poses were observable only if the object was launched with carefully chosen initial configuration. For example, the pose of Fig. 31.C appeared in the experiments.

The experimental results are scattered around minimum points of the potential energy. The variability is only partially caused by an imperfect pose reconstruction. The physical sources of variability are discussed in Sec. 2.4.5. There is also a visible tendency for the large parts to rest in a slightly asymmetrical pose (off the 90° of east longitude line of Fig. 33), which is caused by the direction of rotation of the ERM motor breaking the perfect symmetry of the setup.

2.4.5 Discussion

In this section we studied the monostatic behavior of rigid objects enclosed in round cages. We found that almost all objects become monostatic if the cage is sufficiently tight, and we developed a computational algorithm to identify the exact limits of monostatic behavior. We addressed various questions motivated by the potential application of this setting as a part feeder. Our investigations are closed by the discussion of remaining problems and challenges of application.

Cage feeders are applicable to almost all parts, except for those where either the center of gravity coincides with the center of the smallest enclosing ball or the critical cage size associated with the birth of a new equilibrium coincides with the radius of the smallest enclosing ball. Both types of coincidence are non-generic for irregularly

---

[1] A video of the experiment is available as supplementary material of [172]

shaped parts, but they often become generic among highly symmetric ones. Nevertheless, not all symmetrical parts are problematic as illustrated by the example of Sec. 2.4.4. In the case of an unwanted coincidence, the feedability of the part can be improved by drilling holes into the part or by using multiple materials to shift the center of gravity.

The practical application of cage feeders requires a robust method to enclose the parts in the cage (or assemble the cage around the part), which is challenging in the 3D case because the cage itself is completely closed. The development of such a manipulation scheme is beyond the scope of the present work.

Our model assumes a perfect elimination of dry friction, nevertheless the real effect of vibration is more complex. The low-frequency (50Hz) and relatively high-amplitude (~1 mm) excitation used in the experiments may cause parts to bounce in the cage. As a result, the final resting poses of the parts (after turning off vibration) will show some variability, or they may even escape from the proximity of marginally stable poses (Sec. 2.4.4). This effect could be eliminated by the application of small-amplitude ultrasonic vibration [97] [155]. Even then, friction reduction is usually incomplete. Vibration may induce nearly frictionless interactions for low sliding velocities, but much friction remains for fast sliding. In other words, dry friction is largely replaced by viscous friction, which is beneficial for a cage feeder, because viscous forces efficiently stop motion at

points of frictionless equilibrium. Some remaining dry friction at zero sliding velocity turns isolated poses of equilibrium into small, continuous sets, which is a second source of variability of the final pose. Vibration may also keep the object in steady slow rotation about a vertical axis, which has been observed in the experiments. More work is needed to explore how this complex behavior affects the performance of cage feeders.

There is one more task to be solved if the cage size selection algorithm is applied to polyhedral approximations of parts with curved surfaces. The approximations may have small clusters of stable poses instead of a single stable pose of the original part. In addition, stable poses with very small basin of attraction may emerge in a small neighborhood of the unstable equilibrium poses of the original part [51]. The refinement of the polyhedral approximation reduces the distances between the equilibrium poses in such a cluster, but they do not necessarily disappear. An extreme example of this artefact occurs for object containing a piece of spherical surface centered exactly at their center of mass. The polyhedral approximation replaces a continuous set of neutral equilibria by a large but finite set of stable and unstable poses. If this phenomenon is not taken into account, the algorithm yields a conservative rather than an exact result. The efficient identification of this type of artefact is subject to future work.

2.5 EQUILIBRIA OF FLOATING OBJECTS: ULAM'S PROBLEM

We will next investigate the equilibria of objects floating on the surface of a liquid, which appears to be another generalization

of finding the equilibria of objects on horizontal ground. In this problem, the average density ρ of the object (defined as

total mass / total volume) relative to the density of the liquid emerges as a scalar parameter, similarly to the cage size parameter α in Sec. 2.4. Resting on a solid surface is identical to the special cases of ρ→0 and 1. It is an intriguing question if there are monostatic homogeneous, convex planar floating objects of density ρ (a generalization of **Theorem 2.2.1**) and if there are mono-monostatic, convex, homogeneous floating objects of density ρ in 3D (generalization of **Theorem 2.2.2**). Indeed both questions are unsolved except for special cases: if ρ is sufficiently close to 0 or 1, mono-monostatic behavior on solid ground is preserved, nevertheless if ρ=1/2 then an invariance property of floating [167] implies that monostatic behavior is impossible. We skip the detailed discussion of these modest results of the author. Instead, we investigate a different, but closely related question with a long and fascinating history.

2.5.1 Historical background and problem statement

The equilibria of floating objects have intriguing properties. The stable equilibria of symmetrical objects are often asymmetrical [68][57][58][11][124]. Alternatively, the set of equilibrium configurations may have symmetries exceeding the degree of the object's symmetry. An interesting question about floating objects – often referred to as Floating Body Problem – was proposed over seventy years ago by Stanislav Ulam [106]: are spheres the only bodies that can float (without turning) in any orientation? We investigate this question for rigid objects affected by gravity and buoyancy forces, while capillary effects are neglected.

Ulam's problem was proposed while he was with the Mathematics Department of the University of Lwów (then part of Poland, today in Ukraine) chaired by the eminent mathematician Stefan Banach. During the 1930's, a place called "Scottish Café" was

an important scene of social life for the members of the department and their visitors, where they often posed, discussed, and solved mathematical problems of all types and difficulties. Interesting problems were collected in a hand-written notebook, bearing the title *Księga Szkocka* or Scottish Book. New problems were recorded in the book even during the first period of Worl War II, when Lwóv was under Soviet occupation and several Russian mathematicians visited the city. The German occupation brought an immediate and tragic end to the flourishing mathematical life in Lwóv, a city with a Jewish population of over 200.000 people. Nevertheless, the Scottish Book survived. After the war, it was translated into English in the United States by Ulam and became known in mathematical circles. Some problems became quite famous. For example, the prize of a live goose (something of quite high value shortly after Great Depression of economy) was documentedly offered for problem 153. The problem was eventually solved and the prize was collected in 1972 by the Swedish mathematician Per Enflo.

The Floating Body Problem appears as number 19 in the book, and only a few special cases have been tackled until recently. A simpler two-dimensional version of this problem, also credited to Ulam, concerns the existence of non-circular planar objects (i.e. logs with horizontal axis), which can float in every orientation. There are simple nontrivial solutions in the form of disconnected bodies in two dimensions as well as of shapes containing holes in 3 dimensions [7]. To exclude such strange solutions, both questions are commonly restricted either to convex bodies or to *star-shaped* bodies (the latter being a property related to but less restrictive than convexity). In the current work, we restrict our attention to *ρ-simple* objects where 0<ρ<1 is a scalar parameter representing the density of the object relative to the liquid.

Definition 2.5.1: *a 3D body is ρ-simple if the intersection of the body with any plane dividing its volume into two parts of volume ratio ρ:1-ρ forms a simply connected set.*

The class of ρ-simple objects also includes all convex objects. Convex solutions of the planar problem were found long ago for density ρ= ½ relative to the liquid [8], and much more recently for other densities [185] [182], see also [167] for some closely related questions. In both cases, many nontrivial neutrally floating objects have been identified. In three dimensions, there are no solutions in the limit of resting on a solid surface (i.e. ρ→0 or 1) [112]; and no solutions among star-shaped objects with central symmetry (other than the sphere) for density ρ=½ [145] [60]. Nevertheless, the German physicist F. Wegner has proposed a perturbation expansion scheme of the sphere for objects with central symmetry and ρ≠½ [183], as well as for bodies with arbitrary shape and ρ= ½ [184]. His calculations point towards the existence of many nontrivial solutions in these wider classes of shapes, even though the proofs are incomplete in that the convergence of the perturbation series has not been examined. Furthermore, no attempt to construct actual solutions of the problem has been reported.

We will take a different approach to construct three-dimensional, neutrally floating objects of density ρ=1/2 with cylindrical symmetry. Our method is an adaptation of [8] to the three-dimensional problem. After reviewing the geometric conditions of neutral floating in Section 2.5.2, these are transformed into a non-standard integro-differential equation with given initial conditions (ie. an initial value problem) for the generating curve of the object (Section 2.5.3-4) using fractional order derivatives. It is shown in Section 2.5.5 that sufficiently small perturbations of the sphere yields physically meaningful nontrivial solutions of the problem and several examples are constructed by

integrating the equations numerically in Sec. 2.5.6. This section is closed by a short discussion of related problems.

2.5.2 Geometric criteria of neutral floating

By the principle of Archimedes, a body of density ρ floats in a liquid of density 1 in such way that a fraction ρ of the object's volume is immersed in the liquid. A configuration satisfying Archimedes' principle is an equilibrium iff the centroid of the object (G) is exactly above the centroid of the immersed portion. The equilibrium is neutral, if after small rotations (with the preservation of Archimedes' principle), the centroid of the immersed part remains on a sphere centered at G, yielding constant potential energy. Our goal is to design objects, for which every configuration of the object satisfying Archimedes' principle is a neutral equilibrium, i.e. for which the centroids of the immersed parts for every possible pose form a sphere of arbitrary radius *s* centered at G.

Any plane that divides the object's volume in ratio ρ:1-ρ is called a *water plane* (*W*) and the intersection of the object with any water plane *W* a *water section* or *W**. We consider two water planes infinitesimally close to each other. The transformation mapping one (W_1) to the other (W_2) is a rotation by an infinitesimal angle α_{12} about a line l_{12}. The water planes and sections have two remarkable properties described below. For a more detailed description, the reader is advised to consult [68] [183] [184] or references therein.

P1: The conservation of the immersed volume implies that l_{12} goes through the centroid of W_1*. It follows from this property that *every water plane is a tangent plane of the closed surface E formed by the centroids of water sections. We will refer to E as 'water envelope'.* Indeed, *E* is not necessarily a
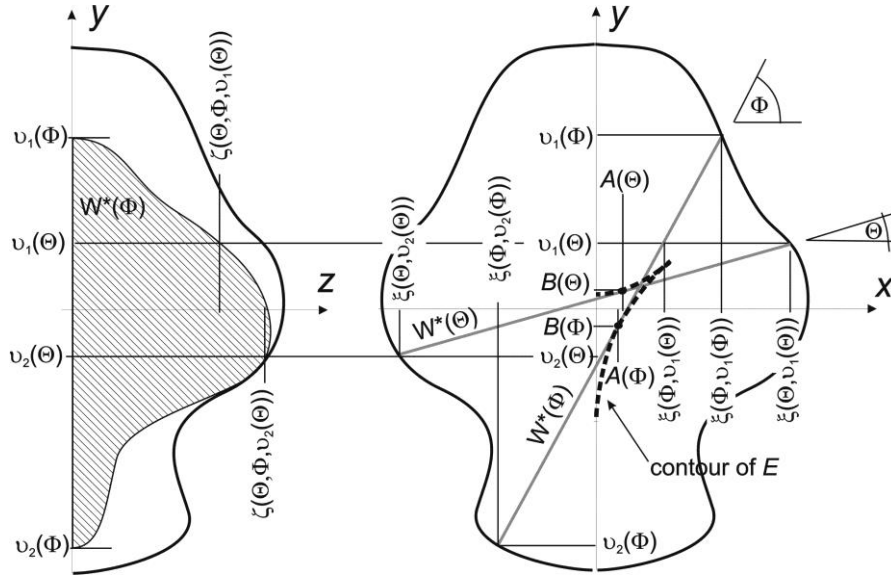
Fig. 34. Projections of a shape of revolution to the *x-y* plane (right panel) and half of its projection to the *y-z* plane (left panel). Thick solid lines denote its contour, *y* is the axis of revolution. The dashed curve in the right panel is the contour of the water envelope. $W^*(\Theta)$ and $W^*(\Phi)$ are two water sections, whose planes are parallel to the *z* axis. $W^*(\Phi)$ is also shown in the left panel by hatching. For further notation, see the main text.

smooth surface, but it is a 'wavefront', which may contain singularities. Nevertheless, it has a well-defined tangent everywhere.

P2: If W_1 corresponds to a neutral equilibrium, then the distance between the centroids of the immersed volumes (G_1 and G_2) corresponding to the two water planes is $|G_1 G_2| = s\alpha_{12}$ where s is the radius defined in the previous paragraph. The same distance can also be expressed as $|G_1 G_2| = \alpha_{12} I_{12} (\rho V)^{-1}$ where V is the volume of the object and I_{12} is the area moment of inertia of W_1^* about the axis l_{12}. Thus, neutrally floating bodies are characterized by the additional property that *the moment of inertia of any water section, about any axis through its centroid is constant (I).*

Property P2 is necessary but not sufficient for a neutral equilibrium. It implies that the centroids of immersed volumes form a sphere of radius s, but it is not necessarily centered at G. However, for objects of density ½, G is exactly halfway between the centroid of the submerged part (G_1) and centroid of the rest of the object (G_1') Furthermore, G_1 and G_1' are opposite points

of the above mentioned sphere. Hence, the sphere is centered at G, i.e. properties P1-P2 are necessary and sufficient.

2.5.3 Integral equations of neutral floating

After introducing some new notation, we develop integral equations corresponding to P1 and P2. We restrict our attention to objects, which are invariant to arbitrary rotation about axis *y* of a Cartesian coordinate system *x-y-z* (Fig. 34). Due to their rotational symmetry, it is enough to consider water planes and sections parallel to the *z* axis. Let $W^*(\Phi)$ denote one such water section, which is at angle $0 \le \Phi \le \pi/2$ to the *x-z* plane (marked by grey hatching in the left panel and by a solid line section in the right panel of Fig. 34). According to property P1 of Section 2.5.2, the centroid of $W^*(\Phi)$ belongs to the contour of the rotation-symmetric water envelope E (dashed line in the right panel of Fig. 34). The *x* and *y* coordinates of this point are $A(\Phi)$ and $B(\Phi)$. The intersection of $W^*(\Phi)$ with the *x-y* plane is a line section (solid line in right panel of Fig. 34). Let $\upsilon_1(\Phi)$ and $\upsilon_2(\Phi)$ denote the *y* coordinates of its

44

endpoints (where υ_2 is usually negative). The functions A, B, υ_1 and υ_2 together determine the object's shape uniquely.

Let $0 \le \Theta \le \Phi$. We will consider a second water section $W^*(\Theta)$ The intersection of $W^*(\Phi)$ with the plane $y=\upsilon_j(\Theta)$ is a line section parallel to the z axis. The x coordinate of all points along this line section is denoted by $\xi(\Phi, \upsilon_j(\Theta))$, which can be expressed as

$$\xi(\Phi, \upsilon_j(\Theta)) = A(\Phi) + \left(\upsilon_j(\Theta) - B(\Phi)\right)\cot\Phi \quad (19)$$

The half-length of the same line section is by Pythagoras' theorem:

$$\zeta(\Theta, \Phi, \upsilon_j(\Theta)) = ...$$
$$...\sqrt{\xi^2(\Theta, \upsilon_j(\Theta)) - \xi^2(\Phi, \upsilon_j(\Theta))} \quad (20)$$

We introduce new variables $\alpha=\sin\Theta$, $\phi=\sin\Phi$ and express the previously defined functions in the new variables as $a(\alpha)=A(\Theta);$ $b(\alpha)=B(\Theta);$ $Y_j(\alpha)=\upsilon_j(\Theta);$ $X(\phi,Y_j(\alpha))=\xi_j(\Phi,\upsilon_j(\Theta))$.The new notations will lead to more convenient equations later. Then, (19), (20) become

$$X(\phi, Y_j(\alpha)) = \qquad (21)$$
$$= a(\phi) + \left(Y_j(\alpha) - b(\phi)\right)\phi^{-1}\left(1 - \phi^2\right)^{1/2}$$
$$= \left(\tilde{a}(\phi) + \left(Y_j(\alpha) - b(\phi)\right)\phi^{-1}\right)\left(1 - \phi^2\right)^{1/2}$$

$$Z(\alpha, \phi, Y_j(\alpha)) = \sqrt{X^2(\alpha, Y_j(\alpha)) - X^2(\phi, Y_j(\alpha))} \quad (22)$$

where

$$\tilde{a}(\alpha) \stackrel{def}{=} a(\alpha)\left(1 - \alpha^2\right)^{-1/2} \quad (23)$$

Now we are ready to transform criteria P1 and P2 into integral equations:

$$P1: \quad \sum_{j=1}^{2}(-1)^j \int_0^\phi Z(\alpha, \phi, Y_j(\alpha))\left(Y_j(\alpha) - b(\phi)\right)Y_j'(\alpha)d\alpha = 0 \qquad (24)$$

$$P2: \quad \sum_{j=1}^{2}(-1)^{j+1} \int_0^\phi Z(\alpha, \phi, Y_j(\alpha))\left(Y_j(\alpha) - b(\phi)\right)^2 Y_j'(\alpha)d\alpha = I\phi^3 \qquad (25)$$

where prime (') means derivative, and property P2 has been applied to an axis parallel to z. Notice that the left side of (25) is the moment of inertia of a projection of the water section $W^*(\arcsin\phi)$ to the y-z plane rather than that of the water section itself. This is compensated by the ϕ^3 term on the right side.

An arbitrary infinitesimal rotation can be composed from two rotations, where the first axis of rotation is parallel to z and the second is perpendicular. For the first type of rotation, eq. (25) is the exact condition of neutrality, whereas the rotational symmetry of the object implies that the second type rotation preserves neutrality. Hence, if the water envelope is given, then (24),(25) are necessary and sufficient conditions of neutral floating.

2.5.4 Formulation as an initial value problem

Analogously to the solution of the planar problem by [8] we first choose a water envelope (see Section 2.5.5 for more details). Once the functions a and b have been specified, the integral equations (24),(25) depend on values of the functions $Y_j(\alpha)$ over the interval $\alpha \in (0, \phi)$. This observation suggests a transformation of the equations into an initial value problem. (24) and (25) can be written in the general form

$$\sum_{j=1}^{2} (-1)^{j+1} \int_{0}^{\phi} g_i(\alpha, \phi, Y_j(\alpha)) Y_j'(\alpha) d\alpha = f_i(\phi) \tag{26}$$

where f_i are scalar functions and g_i are scalar functionals; $i = 1$ for the first equation and 2 for the second. Differentiating (26) with respect to ϕ yields

$$\sum_{j=1}^{2} (-1)^{j+1} \left(\int_{0}^{\phi} \frac{\partial g_i(\alpha, \phi, Y_j(\alpha))}{\partial \phi} Y_j'(\alpha) d\alpha + g_i(\phi, \phi, Y_j(\phi)) Y_j'(\phi) \right) = f_i'(\phi) \tag{27}$$

which is a system of 2 linear algebraic equations in the unknowns $Y_j'(\alpha)$ ($j = 1,2$) if the values of the integrals are known. If the two-by-two matrix composed of the elements $g_i(\phi, \phi, Y_j(\phi))$ is nonsingular, then $Y_j'(\phi)$ can be expressed explicitly from the equations, yielding a first-order initial value problem for $Y_j(\phi)$. Nevertheless it might happen that all elements of the matrix are zero. In this case, the second derivative of (26) becomes

$$\sum_{j=1}^{2} (-1)^{j+1} \left(\int_{0}^{\phi} \frac{\partial^2 g_i(\alpha, \phi, Y_j(\alpha))}{\partial \phi^2} Y_j'(\alpha) d\alpha + \left. \frac{\partial g_i(\alpha, \phi, Y_j(\alpha))}{\partial \phi} \right|_{\alpha=\phi} Y_j'(\phi) \right) = f_i''(\phi) \tag{28}$$

which is again a candidate for an initial value problem. If the $\partial g_i()/\partial \phi$ terms also happen to be zero, additional derivation of the equations might be necessary. Unfortunately, this method fails for the specific function g_i of the problem of neutral floating, because $g_i(\phi, \phi, Y_j(\phi))$ is identically zero whereas the first derivative $\partial g_i / \partial \phi$ does not exists; specifically

$$\lim_{\alpha \to \phi} \left| \frac{\partial g_i(\alpha, \phi, Y_j(\alpha))}{\partial \phi} \right| = \infty \tag{29}$$

The diverging limit indicates that differentiating (26) twice is "too much",

whereas differentiating only once is not enough. This special property of g_i is a consequence of the square-root type singularity of the function Z in (22) at $\alpha = \phi$, inherited by g_i. The specific form of Z implies that *the fractional derivative of order 3/2 of g_i is finite and nonzero at $\alpha = \phi$; thus the 3/2th derivative of (26) leads to an initial value problem.

Fractional derivatives are defined as integer order derivatives of a fractional integral of order less than 1 [109]. Thus, the first step towards the 3/2th derivative is to take the semi-integral of (26) using the definition of Riemann–Liouville differintegrals:

$$\sum_{j=1}^{2} (-1)^{j+1} \int_{0}^{\chi} (\chi - \phi)^{-1/2} \cdot \int_{0}^{\phi} g_i(\alpha, \phi, Y_j(\alpha)) Y_j'(\alpha) d\alpha d\phi = \int_{0}^{\chi} (\chi - \phi)^{-1/2} \cdot f_i(\phi) d\phi \tag{30}$$

Before proceeding with the differentiation, the order of integration is changed on the left side of the equation and the new functions G_i and F_i are introduced in order to shorten the expression:

$$\sum_{j=1}^{2} (-1)^{j+1} \int_{0}^{\chi} Y_j'(\alpha) \cdot \underbrace{\int_{\alpha}^{\chi} (\chi - \phi)^{-1/2} g_i(\alpha, \phi, Y_j(\alpha)) d\phi \, d\alpha}_{G_i(\alpha, \chi, Y_j(\alpha))} = \underbrace{\int_{0}^{\chi} (\chi - \phi)^{-1/2} \cdot f_i(\phi) d\phi}_{F_i(\chi)} \tag{31}$$

We differentiate both sides with respect to χ, using the Leibniz integral rule:

$$\sum_{j=1}^{2} (-1)^{j+1} \left(\int_{0}^{\chi} Y_j'(\alpha) \cdot \frac{\partial}{\partial \chi} G_i(\alpha, \chi, Y_j(\alpha)) d\alpha + Y_j'(\chi) \cdot \underbrace{G_i(\chi, \chi, Y_j(\chi))}_{zero} \right) = F_i'(\chi) \tag{32}$$

The term $G_i(\chi, \chi, Y_j(\chi))$ is by definition (see (31)) a definite integral of a function with an integrable singularity over an interval of zero length, hence it equals zero for any value of χ. For a more detailed explanation, see eq. (170) of Appendix 5.4.1. Thus we have

$$\sum_{j=1}^{2} (-1)^{j+1} \int_{0}^{\chi} Y_j'(\alpha) \cdot \frac{\partial}{\partial \chi} G_i(\alpha, \chi, Y_j(\alpha)) d\alpha = F_i'(\chi) \tag{33}$$

Differentiating both sides once more yields

$$\sum_{j=1}^{2} (-1)^{j+1} \left(\int_{0}^{\chi} Y_j'(\alpha) \cdot \frac{\partial^2}{\partial \chi^2} G_i(\alpha, \chi, Y_j(\alpha)) d\alpha + Y_j'(\chi) \cdot \frac{\partial}{\partial \chi} G_i(\alpha, \chi, Y_j(\alpha)) \Big|_{\alpha = \chi} \right) = F_i''(\chi) \tag{34}$$

The functions $F_i''(\chi)$ can be expressed in closed form, specifically $F_1''(\chi)=0$ and $F_2''(\chi)=8I\chi^{3/2}$. Thus, the unknowns $Y_j'(\chi)$ can be expressed explicitly from (34) as

$$\mathbf{Y}'(\chi) = \begin{bmatrix} 1 & 0 \\ 0 & -1 \end{bmatrix} \mathbf{A}(\chi, \mathbf{Y}(\chi))^{-1} \left(\begin{bmatrix} 0 \\ 8I\chi^{3/2} \end{bmatrix} - \int_{0}^{\chi} \mathbf{C}(\alpha, \chi, \mathbf{Y}(\alpha), \mathbf{Y}'(\alpha)) d\alpha \cdot \begin{bmatrix} 1 \\ -1 \end{bmatrix} \right) \tag{35}$$

where $\mathbf{Y}$ and $\mathbf{Y}'$ are column vectors composed of the functions Y_j and Y_j'; $\mathbf{A}$ and $\mathbf{C}$ are 2 by 2 matrices with elements

$$a_{ij}(\chi, Y_j(\chi)) = \frac{\partial}{\partial \chi} G_i(\alpha, \chi, Y_j(\alpha)) \Big|_{\alpha = \chi} \tag{36}$$

$$c_{ij}(\alpha, \chi, Y_j(\chi), Y_j'(\chi)) = \dots$$

$$\dots = Y_j'(\alpha) \cdot \frac{\partial^2}{\partial \chi^2} G_i(\alpha, \chi, Y_j(\alpha)) \tag{37}$$

In the sequel, the matrices $\mathbf{A}$ and $\mathbf{C}$ will be examined thoroughly in order to uncover important properties of the solutions of the initial value problem (35).

2.5.5 Solutions of the integro-differential equation

A The existence and uniqueness of solutions

Solid spheres of any radius S are neutrally floating objects. They correspond to $Y_j(\phi) = S(-1)^{j+1}\phi$. We deduce implicitly that

47

this function satisfies the initial value problem (35) for $a(\phi)=b(\phi)\equiv0$ with initial conditions $Y_j(0)=b(0)$. We refer to the corresponding equations and solutions as well as elements of these equations as *trivial* equations, solutions, etc. In this section, we want to examine nontrivial solutions obtained by minor perturbations of the functions $a(\phi)=0$ and $b(\phi)=0$.

There are some technical issues arising from singularities of the equations at $\chi=0$. Every solution (including the family of trivial solutions) satisfies

$$Y_j(0)=0 \tag{38}$$

i.e. (38) does not provide us with a well-defined initial condition. Indeed, if $\chi\to0^+$, all elements $\mathbf{A}$, $\mathbf{C}$, and $\mathbf{F}$ in (24), (25) go to zero, which is inherited by (35). Hence, (35) becomes identity. This means that an initial condition must also include $Y_j^{'}(0)$. For example, the trivial solutions have $\mathbf{Y'}(0)=S\cdot[1 \ -1]^T$. To avoid difficulties arising from the singularity of our variables at $\chi=0$, we narrow our focus to those solutions, which coincide with the trivial solution ($a(\phi)=b(\phi)=0$ and $Y_j(\phi)=S(-1)^{j+1}\phi$) if $\phi<\alpha_1$ for some positive scalar α_1. It is demonstrated below that the problem has a unique solution under this restriction.

It should also be noticed that differentiating an equation may introduce fake solutions. Specifically (35) has been obtained by taking the $3/2^{\text{th}}$ derivative of an equation of the form $u(\chi,\mathbf{Y}(\chi),...)=0$. After differentiation, the new equation admits fake solutions for which $u(\chi,\mathbf{Y}(\chi),...)=constant\cdot\chi^{3/2}$ rather than 0. Nevertheless, the set of fake solutions correspond to water sections with moment of inertia $I+constant\cdot\chi^{-3/2}$, which contradicts any initial condition of the form $Y_j^{'}(0)=constant$. Hence all solutions of our initial value problem will be true solutions of the original equations (24), (25).

We start the formal proof by introducing *Lemma 2.5.2*, which states that any solution of the perturbed equations must be close to the trivial solution, without examining if such solutions exist or not. The questions of existence and uniqueness are answered by the subsequent *Lemma 2.5.3*. The two lemmas are summarized in *Theorem 2.5.4*, which is the main result of Sec. 2.5.

Lemma 2.5.2: *for any given scalar $0<\alpha_1$, there exist positive scalars k and ε_0, such that if*

(i) $a(\alpha)=0$, $b(\alpha)=0$ and $Y_j(\alpha)=(-1)^{j+1}\alpha$ for all $0\leq\alpha\leq\alpha_1$; and

(ii) the absolute values of $\tilde{a}(\alpha)$, $b(\alpha)$, and of their derivatives up to third order exist and are $<\varepsilon<\varepsilon_0$ for any $\alpha_1\leq\alpha\leq1$

then any solution of equations (35) over the interval $\alpha_1<\alpha\leq1$ satisfies

$$\left|Y_j{}'(\alpha)-(-1)^{j+1}\right| \leq k\varepsilon e^{k\alpha} \tag{39}$$

Proof of Lemma 2.5.2:

We arrive to (39) via proof by contradiction. The initial section $0\leq\alpha<\alpha_1$ of $Y_j(\alpha)$ satisfies (39) for any k by point (i) of *Lemma 2.5.2*. Let us assume now that (39) is violated no matter how large k is. Then there must exist a unique scalar $\alpha_1<\chi(k)<1$ for any k such that (39) holds for $\alpha\leq\chi(k)$ and there is equality in (39) for $\alpha=\chi(k)$ and $j=1$ or 2. The inequality condition implies the following bound on $Y_j(\alpha)$:

$$\left|Y_j(\alpha)-(-1)^{j+1}\alpha\right| \leq \int_0^\alpha\left|Y_j{}'(\beta)-(-1)^{j+1}\right|d\beta < \varepsilon\int_0^\alpha ke^{k\beta}d\beta = \varepsilon\left(e^{k\alpha}-1\right)<\varepsilon e^{k\alpha} \quad if \quad \alpha\leq\chi(k) \tag{40}$$

which will be used in the sequel. From this point, the argument k of χ is dropped for brevity.

If ε is small enough, then (39) and (40) imply that

1) each entry of $\mathbf{A}(\chi,\mathbf{Y}(\chi))$ is within a neighborhood of radius $*\cdot\varepsilon e^{k\chi}$ of their trivial values, and the trivial values are bounded (the latter is proven in Appendix 5.4.1); $*$ represents some finite positive scalar, which is independent of k. Furthermore, $\mathbf{A}(\chi)$ is non-singular, i.e. $|\det\mathbf{A}|$ has a positive lower bound (see Appendix 5.4.2). The two results imply that $\mathbf{A}^{-1}(\chi,\mathbf{Y}(\chi))$ is also within a neighborhood of radius $*\cdot\varepsilon e^{k\chi}$ of its bounded trivial value.

2) if $k>1$, then the second derivative of G_i is within distance $*\cdot\varepsilon e^{k\alpha}$ of its bounded trivial value, i.e.

$$\frac{\partial^2}{\partial\chi^2}G_i(\alpha,\chi,Y_j(\alpha))\in\ldots$$
$$\ldots\frac{\partial^2}{\partial\chi^2}G_{ij}^{(0)}(\alpha,\chi)\pm*\cdot\varepsilon e^{k\alpha} \tag{41}$$

see Appendix 5.4.3 for proof. By plugging (39) and (41) into (37) one obtains

$$c_{ij}\in\left((-1)^{i+1}\pm k\varepsilon e^{k\alpha}\right)\left(\frac{\partial^2}{\partial\chi^2}G_{ij}^{(0)}(\alpha,\chi)\pm*\varepsilon e^{k\alpha}\right)\in\ldots.$$

$$\underbrace{(-1)^{i+1}\frac{\partial^2}{\partial\chi^2}G_{ij}^{(0)}(\alpha,\chi,Y_i)}_{\text{bounded trivial value}}\pm\underbrace{\left(\max\;|\frac{\partial^2}{\partial\chi^2}G_{ij}^{(0)}(\alpha,\chi)|+*\cdot\underbrace{k^{-1}}_{<1}+*\cdot\underbrace{\varepsilon e^{k\alpha}}_{\ll1}\right)\cdot\varepsilon k e^{k\alpha}}_{*\varepsilon k \exp(k\alpha)\text{ deviation}} \tag{42}$$

Hence, we conclude that each entry of $\mathbf{C}(\alpha,\chi,\mathbf{Y}(),\mathbf{Y}'())$ is within a neighborhood of radius $*\cdot\varepsilon k e^{k\alpha}$ of its bounded trivial value.

Eq. (35) together with the bounds of $\mathbf{A}^{-1}$ and $\mathbf{C}$ found above, imply that (39) holds if $\alpha=\chi$ with the left hand side strictly smaller than the right-hand side, provided that k exceeds some threshold that we denote by k_0. This result contradicts the assumption that we have equality in (39) if $\alpha=\chi$. Hence, (39) is true for all χ if $k>k_0$. Details of the last piece of calculation are omitted, but we point out that $\mathbf{C}$ is inside an integral in (35). Integrating its maximum deviation $*\varepsilon k\exp(k\alpha)$ from the trivial value yields $*\varepsilon\exp(k\chi)$ maximum deviation in $\mathbf{Y}'\bullet$

Lemma 2.5.3: *there exists a positive scalar ε_0 such that (35) has a unique solution if (i) and (ii) of **Lemma 2.5.2** are satisfied.*

*Proof of **Lemma 2.5.3**:* ODE's with Lipschitz-continuous right-hand sides and given initial condition have unique solutions according to the Picard-Lindelöf theorem [42]. We present an adaptation of the standard proof of this result to the initial value problem (35).

By introducing the function $\mathbf{\Psi}()=\mathbf{Y}'()$, (35)-(37) can be rewritten as

$$\mathbf{\Psi}(\chi)=\begin{bmatrix}1&0\\0&-1\end{bmatrix}\mathbf{A}\left(\chi,\int_0^\chi\mathbf{\Psi}(\beta)d\beta\right)^{-1}\left(\begin{bmatrix}0\\8I\chi^{3/2}\end{bmatrix}-\int_0^\chi\mathbf{C}\left(\alpha,\chi,\int_0^\alpha\mathbf{\Psi}(\beta)d\beta,\mathbf{\Psi}(\alpha)\right)\cdot d\alpha\cdot\begin{bmatrix}1\\-1\end{bmatrix}\right) \tag{43}$$

$$a_{ij}=\left.\frac{\partial}{\partial\chi}G_i\left(\alpha,\chi,\int_0^\alpha\Psi_j(\beta)d\beta\right)\right|_{\alpha=\chi} \tag{44}$$

$$c_{ij}=\Psi_j(\alpha)\cdot\frac{\partial^2}{\partial\chi^2}G_i(\alpha,\chi,\int_0^\alpha\Psi_j(\beta)d\beta) \tag{45}$$

Assume that the solution Ψ of (43) is known for $\chi \leq \chi_0$ and satisfies (39):

$$\left| \Psi_j(\chi) - (-1)^{j+1} \cos \chi \right| \leq k\varepsilon e^{k\chi} \qquad (46)$$

We aim to prove that there is a unique solution over an additional finite interval $\chi_0 < \chi \leq \chi_1$. Splitting the integrals in (43) at χ_0 yields

$$\Psi(\chi) = \begin{bmatrix} 1 & 0 \\ 0 & -1 \end{bmatrix} \mathbf{A}\left(\chi, \underbrace{\int_0^{\chi_0} \Psi(\beta)d\beta}_{known} + \int_{\chi_0}^{\chi} \Psi(\beta)d\beta \right)^{-1} \cdot$$

$$\cdots \left(\underbrace{\begin{bmatrix} 0 \\ 8I\chi^{3/2} \end{bmatrix} - \int_0^{\chi_0} \mathbf{C}\left(\alpha, \chi, \int_0^{\alpha} \Psi(\beta)d\beta, \Psi(\alpha) \right) \cdot \begin{bmatrix} 1 \\ -1 \end{bmatrix} d\alpha}_{known} - \int_{\chi_0}^{\chi} \mathbf{C}\left(\alpha, \chi, \int_0^{\alpha} \Psi(\beta)d\beta, \Psi(\alpha) \right) d\alpha \cdot \begin{bmatrix} 1 \\ -1 \end{bmatrix} \right) \qquad (47)$$

The right-hand side of (47) defines a self-map K over the space σ_0 of vector valued continuous functions $\Psi(\chi)$ over the interval $\chi \in (\chi_0, \chi_1)$. σ_0 and the metric d induced by the norm

$$\| \Psi(\chi) \| \overset{def}{=} \max_{\chi, j} \left| \Psi_j(\chi) \right| \qquad (48)$$

form a Banach space. Let σ denote the closed subset of σ_0 determined by (46). The arguments used in the proof of *Lemma 2.5.2* imply that for ε small enough and $k > k_0$, K maps σ into itself. The contraction principle implies that *if K is a contraction* then it has a unique fixed point, corresponding to a unique solution of (47). Repeated application of the above argument yields

global existence and uniqueness for $\alpha_1 \leq \chi \leq 1$. Integrating the solution Ψ leads to a unique solution $\mathbf{Y}$ of the original problem.

The only remaining gap in the proof is the *contractivity of K*. $\mathbf{A}$ is Lipschitz in its second variable (cf. (173)). As $\mathbf{A}$ is nonsingular (Appendix 5.4.2), its inverse is also Lipschitz with some Lipschitz constant L_{invA}. Similarly, (45) and some examination of (176) yield that $\mathbf{C}$ is Lipschitz-continuous functional of $\Psi(\chi)$, $\chi \in (\chi_0, \chi_1)$ with a Lipschitz constant L_C (details omitted).

Next, we consider two arbitrary elements $\Psi^{(1)}$ and $\Psi^{(2)}$ of the set σ. Then,

$$d\left(\mathbf{A}\left(\chi, \int_0^{\chi_0} \Psi(\beta)d\beta + \int_{\chi_0}^{\chi} \Psi^{(1)}(\beta)d\beta \right)^{-1}, \mathbf{A}\left(\chi, \int_0^{\chi_0} \Psi(\beta)d\beta + \int_{\chi_0}^{\chi} \Psi^{(2)}(\beta)d\beta \right)^{-1} \right) \leq L_{invA} (\chi - \chi_0) d\left(\Psi^{(1)}, \Psi^{(2)} \right) \qquad (49)$$

and

$$d\left(\int_{\chi_0}^{\chi} \mathbf{C}\left(\alpha, \chi, \int_0^{\chi_0} \Psi(\beta)d\beta + \int_{\chi_0}^{\chi} \Psi^{(1)}(\beta)d\beta, \Psi^{(1)}(\alpha) \right) d\alpha, \int_{\chi_0}^{\chi} \mathbf{C}\left(\alpha, \chi, \int_0^{\chi_0} \Psi(\beta)d\beta + \int_{\chi_0}^{\chi} \Psi^{(2)}(\beta)d\beta, \Psi^{(1)}(\alpha) \right) d\alpha \right) \leq \cdots$$

$$\cdots L_C (\chi - \chi_0) d\left(\Psi^{(1)}, \Psi^{(2)} \right) \qquad (50)$$

These inequalities and the boundedness of all terms in the formula of K imply that $d(K(\Psi^{(1)}), K(\Psi^{(2)})) \leq L(\chi - \chi_0) d(\Psi^{(1)}, \Psi^{(2)})$ with

some constant L. Hence, if $\chi - \chi_0 < L^{-1}$ then K is contractive. •

The statements of the two lemmas can be summarized as

Theorem 2.5.4: *for any given scalars $0<\alpha_1<1$ and $\Delta>0$, there exists a positive scalar ε_0 such that (35) has a unique solution $\mathbf{Y}(\chi)$ if (i) and (ii) of* **Lemma 2.5.2** *are satisfied. Furthermore, the solution satisfies $Y_j(\chi)=(-1)^{j+1}\chi$ for $0\leq\chi\leq\alpha_1$ and $|Y_j(\chi)-(-1)^{j+1}\chi|<\Delta$ for $\alpha_1<\chi\leq1$.* $\mathbf{Y}(\chi)$ *is also a valid solution of* (24), (25).

What follows in the next subsection is the demonstration that the solution whose existence has just been proven generates a ρ-simple object.

B Characterization of acceptable solutions

The water envelopes $a(\phi)$ and $b(\phi)$ together with a pair of function $Y_j(\phi)$ over the interval $0\leq\phi\leq1$ determine the 'upper' ($j=1$) and the 'lower' ($j=2$) half of a unique curve in the x-y plane. The coordinates (x,y,z) of a point $P_j(\phi)$ of the curve are $x=(-1)^{j+1}X(\phi,Y_j(\phi))$; $y=Y_j(\phi)$; $z=0$. Rotation of this curve about the y axis generates a unique object with cylindrical symmetry. Below we state a sufficient condition under which the object is ρ-simple. This condition is satisfied by the nontrivial solutions predicted by **Theorem 2.5.4**.
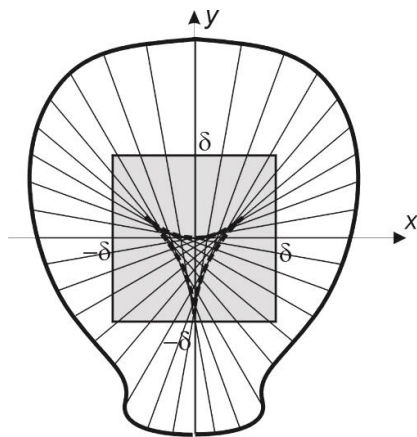
Fig. 35. Illustration of *Lemma 2.5.5*: **if the water envelope is inside the grey square, and the contour curve is outside, then the object is a ρ-simple topological ball.**

Lemma 2.5.5 *If for any $0<\phi<1$*

$$\begin{aligned} \text{either} \quad & (-1)^{j+1}Y_j(\phi)>\delta \\ \text{or} \quad & (-1)^{j+1}X(\phi,Y_j(\phi))>\delta \end{aligned} \tag{51}$$

with

$$\delta=\max\left\{\begin{array}{c}\max_\phi|a(\phi)|\\\max_\phi|b(\phi)|\end{array}\right\} \tag{52}$$

then the object is a ρ-simple topological ball.

Proof of **Lemma 2.5.5**:

The condition of the lemma implies that one can draw a square of size $2\delta\times2\delta$ about the origin of the x-y plane such that the water envelope is inside the square while the contour curve is outside (Fig. 35). Outside the square, the upper-right quarter of the x-y plane is covered with the non-intersecting tangent lines $L(\phi)$ of E, each containing a point $P_1(\phi)$ of the generating curve. The lower-right quarter contains the points $P_2(\phi)$ each one lying on the mirror images of lines $L(\phi)$ about the y axis. Thus, all points $P_j(\phi)$ for $\phi<1$ are in the right half-plane, separated from the y axis. Furthermore, two points of the contour curve corresponding to different values of ϕ or different values of j, lie on different lines, hence they may not coincide. Altogether we have found that the *contour curve does not touch the y axis* (except at the endpoints: $\phi=1$), and *it is not self-intersecting* (or self-touching). Rotating such curves generates topological balls.

Due to the cylindrical symmetry of the object, being ρ-simple is equivalent of requiring that the intersection of $L(\phi)$ with the object (from here on: $L^*(\phi)$) is a connected line segment for every ϕ (rather than the union of multiple segments). $L^*(0)$ is connected, hence, the object is ρ-simple iff by varying ϕ, the topology of $L^*(\phi)$ does not change. A topological change of L^* occurs at ϕ if the contour curve touches $L(\phi)$ at $P_1(\phi)$ or the mirror image of $L(\phi)$ at $P_2(\phi)$ *without crossing the line*. Nevertheless this situation is impossible because, as already

mentioned, the points $P_j(\phi)$ lie on the lines $L(\phi)$ and their mirror images, which are free of intersections outside the square.•

2.5.6 Numerical examples

A convenient way to find a suitable water envelope is to pick a C^1 function $\rho(\Phi)$ with a bounded but possibly discontinuous second derivative representing the signed radius of curvature of the water envelope at tangent angle Φ. Then,

$$A(\Phi) = \int_{\Phi}^{\pi/2} \rho(\Theta)\cos\Theta\, d\Theta + c_A \qquad (53)$$

$$B(\Phi) = \int_{\Phi}^{\pi/2} \rho(\Theta)\sin\Theta\, d\Theta + c_B \qquad (54)$$

The symmetry of the problem dictates some constraints

A: $A(\pi/2)=0$, hence $c_A=0$;

B: variations of c_B result in translated copies of the same envelope, i.e. we can choose $c_B=0$.

C: $A(0)=0$, which means that (53) provides a constraint for $\rho(\Phi)$

D: $\rho(\Phi)$ is π-periodic and even;

E: $\rho(\Phi-\pi/2)$ is odd, implying $\rho(\pi/2)=0$.

In the variables α and ϕ, (53) and (54) become

$$a(\phi) = \int_{\phi}^{1} \rho(\arcsin \alpha)\, d\alpha \qquad (55)$$

$$b(\phi) = \int_{\phi}^{1} \rho(\arcsin \alpha)\, \frac{\alpha}{\sqrt{1-\alpha^2}}\, d\alpha \qquad (56)$$

The $\arcsin\alpha$ function has a square-root singularity at $\alpha=1$. According to observation E, $\rho(\arcsin\alpha)\approx constant\cdot(\pi/2-\alpha)^{1/2}$ near $\phi=1$. This singularity is cancelled by a $(\pi/2-\alpha)^{-1/2}$ term in (56), thus $b(\phi)$ becomes C^2 with a bounded third derivative. At the same time, $a(\phi)\approx constant\cdot(1-\phi^2)^{3/2}$ near $\phi=1$, which means that $a(\phi)$ is singular at $\phi=1$, but the related function $\tilde{a}(\phi)$ (see (23)) has a bounded third derivative. The smoothness of b and $\tilde{a}$ mean that any function $\rho(\Phi)$ multiplied by a sufficiently small constant meets condition (ii) of ***Lemma 2.5.2***.

Next we present two examples fulfilling the above requirements:

$$\rho(\Phi) = c \cdot \cos\big((2n+1)\Phi\big) \qquad n = 1,2,3\ldots \qquad (57)$$

$$\rho(\Phi) = c \cdot \begin{cases} 0 & if & \phi \le \pi/4 \\ \sin^2 4\Phi - \dfrac{85}{84}\sin^3(4\Phi) & if & \pi/4 < \phi \le \pi/2 \end{cases} \qquad (58)$$
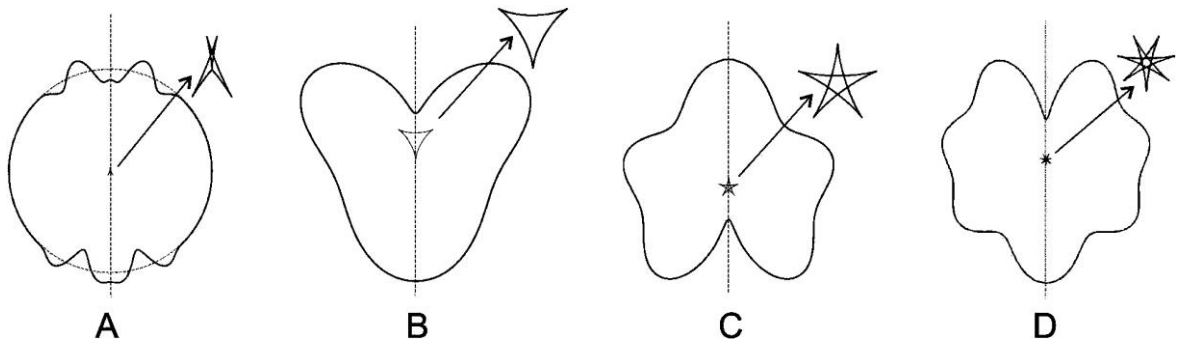

Fig. 36. Numerically determined contour curves and water envelopes of some neutrally floating shapes with cylindrical symmetry. A: water envelope (58) with c=0.5; B-D: water envelope (57) with n=1,2,3 and c=0.5; 0.5;0.4. In all cases, $Y_1'(0)=-Y_2'(0)=1$.

where *c* is an arbitrary constant; the number 85/84 is determined by Observation C. The second example obeys condition (i) of the lemma, hence this envelope generates a nontrivial solution by **Theorem 2.5.4** if its unspecified constant is small enough, see also Fig. 36.A.

The first example does not meet condition (i) nevertheless the solution appears to exist and to be unique in this case, too (Fig. 36.B-D, Fig. 37). Indeed, condition (i) is probably unnecessary for **Lemma 2.5.2**, but it simplifies the proof outlined in Appendix 5.4.3. Additionally, condition (i) has a central role in the proof of **Lemma 2.5.2**. Nevertheless, existence (and uniqueness) of the solution might be provable with a different approach without condition (i).

2.5.7 Related works

In Sec. 2.5, we presented a proof of existence of neutrally floating, simple objects of density 1/2 (other than the sphere) in three dimensions. We also constructed examples among bodies with cylindrical symmetry. Our study leaves many open questions, including the necessity of condition (i) in **Theorem 2.5.4**, or the existence of solutions for densities other than 1/2.

The present discussion of the Floating Body Problem concentrates on gravitational (and buoyancy) forces, and excludes any other forces acting on the object. A different approach has been taken by R. Finn and coworkers [63] [62], see also [77] [134], who studied particles floating in gravity-free environment under the effect of capillary forces. In this approach, the contact angle of the object and the liquid is a free parameter analogous to density in the presence of gravity. The two-dimensional capillary floating problem admits nontrivial solutions similarly to the Archimedean version, see [76] for more background. In three dimensions, only a special nonexistence result has been published: spheres are the only objects, which can float

in any orientation in such a way that the capillary forces generate *a perfectly flat liquid surface* around the object. In most cases, a macroscopically flat liquid surface typically becomes distorted in a small neighborhood of a floating object to minimize the surface energy of the solid liquid and air-liquid interfaces. This more general situation seems to be unexplored.

While gravity-free floating may appear as an unusual setting at first sight, it is physically as relevant as the Archimedean approach. Physical systems under terrestrial conditions are inevitably subject to both gravity and capillary forces. The relative strengths of the two forces are determined by the dimensionless Eötvös- (or Bond-) number of the system. Small-scale objects have low Eötvös numbers (indicating the dominance of capillary effects), whereas upscaling an object increases the Eötvös number. For example, the Eötvös number of a ball of density ½ and radius *r* floating in water is approximately $(r/4mm)^2$. Thus, the dominance of each of the two effects can be realized in a physical experiment. Additionally, there exists a generalized –
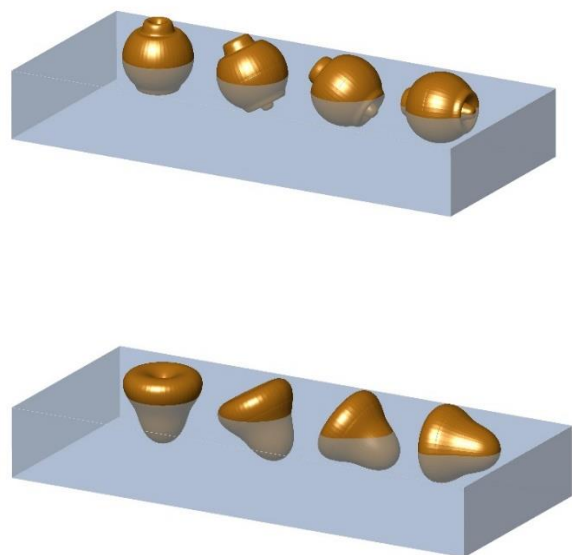
Fig. 37. Three-dimensional models of the neutrally floating object depicted in Fig. 36.A-B

and completely unexplored – version of Ulam's problem, which seeks neutrally floating objects under combined influence of gravity and surface tension for given density, contact angle and Eötvös number.

There are many other intriguing problems related to the equilibria of floating objects, some of which are discussed in paper [167] of the author. These include for example the existence of monostatic and neutral behavior for objects, which are floating while pinned at their center of gravity; and the balance points of hollows shapes on horizontal ground partially filled with a liquid. Indeed all problems tackled in Chapter 2 belong to a rich group of geometric problems, in which one seeks to find shapes such that an associated function has as few extremal points as possible (see for example the Four vertex theorem or the Tennis ball theorem) or such that an associate function becomes constant (as in the case of curves with constant width and surfaces of constant curvature). Many of these problems can be found for example in [130].

CHAPTER 3:

THE STABILITY OF EQUILIBRIA AND THE DYNAMICS INDUCED BY IMPACTS AND FRICTION

IN the previous chapter, we have looked at various problems related to the number of equilibria of a rigid body. Most of these problems required a geometric approach. Now we move on to studying *the motion* of bodies near a stable equilibrium, motivated by various engineering applications, including part feeding, as well as robotic grasping and locomotion. The aim of Chapter 3 is twofold:

- to study the stability of equilibria against small perturbations
- to estimate the degree of attractivity of stable equilibria, i.e. the likelihood that the motion of an object with an uncertain initial state terminates in a given equilibrium.

Both questions require the investigation of the dynamics of these systems. In Sec. 3.1, we review basic concepts of rigid body dynamics with unilateral contacts. This is followed by the analysis of *pose statistics*, i.e. the probability distribution of final resting poses of an object dropped onto the ground with random initial conditions. Similarly to Chapter 2, the support surface is assumed to be flat, and thus many notions of Chapter 2 (including equilibrium poses) remain in use. The method of the analysis remains largely geometric as we develop geometrically inspired phenomenological models of the falling motion. Nevertheless, the results of the analysis are benchmarked against predictions of a custom-made numerical simulation tool, which considers the full hybrid dynamics, including impacts.

In Sec. 3.3, we study the *static stability* of equilibria, i.e. stability against small perturbing forces. These perturbations do not induce separation of active contacts, nor slippage of sticking contacts. Due to the simplicity of the objects' response to the perturbation, we are able to assess the stability of multibody systems with arbitrary number of components and point contacts. The external supports of the system may have an arbitrary geometric arrangement. The lack of translational and rotational symmetry of the environment explains why we consider the stability of a *configuration of equilibrium* (rather than a pose or an orientation of equilibrium as in Chapter 2). In this setting, dry friction becomes a crucial ingredient, which is taken into account by the analysis. The basic tools of the analysis include

- *contact regularization*: we replace rigid contacts with viscoelastic ones and consider the behavior of the system as the stiffness of contacts goes to infinity.
- *energetic analysis*: we seek a local minimum of a potential energy function, as a sufficient condition of stability.

In Sec. 3.4, we study the *Lyapunov stability* of equilibria, i.e. stability against arbitrary small state perturbations. Even though Lyapunov stability is a standard concept in dynamical systems theory, its application to rigid mechanical systems with contacts is difficult, because even an infinitesimally small perturbation initiates complex, nonlinear, and hybrid motion. The richness of the dynamics makes this problem similar

to the famous *n*-body problems in celestial mechanics. The motion of two point masses under gravity has been understood since the times of Kepler and Newton. Nevertheless for 3 or more bodies, the system's motion becomes extremely complex, and it is subject of active research. The simplest example of complex behavior is the circular, restricted 3-body problem (the planar motion of a small mass in the gravitational field of two big masses orbiting along circular paths around each other), which is considered today an important model problem of celestial mechanics. In the field of Lyapunov stability analysis in the presence of unilateral frictional contacts, the simplest case is that of a single, planar, rigid body resting on a slope with a single contact point (1 body - 1 contact, or 1B1C problem). In response to small perturbations, this systems undergoes simple bouncing and rocking motion, which enables one to easily determine the condition of stability [36]. At the same time, the behavior of systems with multiple contact points is complex and poorly understood. The present work deals with the next simplest scenario: a single planar body with 2 supports on a flat slope (restricted 1B2C problem). Our results are based on constructing a Lyapunov-like function, which usually decreases during the motion, despite the possibility of temporary increase.

3.1 NEW CONCEPTS

3.1.1 Friction

In Sec. 3.2, we investigate objects on a flat, horizontal terrain, and assume interactions to be frictionless for the sake of simplicity.

Nevertheless, equilibrium on a terrain, which is not horizontal usually requires dry friction, and indeed friction is inevitably present in most engineering problems. Therefore, in Sec. 3.3 we use a general model of *sticking* friction for isolated point contacts. As long as a rigid contact is in stick state, the contact force **f** is determined from the requirement of no relative motion between the interacting objects, and for compliant contacts (see Sec. 3.1.5), **f** is determined by a contact model. The heart of the friction model is a continuous scalar-valued indicator function $S(\mathbf{f})$ associated with each contact point. S is used to determine if the state of the contact stays in stick state or not. Specifically, an active contact is in sticking state as long as $S(\mathbf{f}) > 0$ and slips or separates if $S(\mathbf{f}) = 0$.

In Sec. 3.4, we restrict our attention to planar systems and Coulomb friction. In the case of stick, the Coulomb model is implemented by the indicator function $S(\mathbf{f})$ $= \mu_i f_z - |f_x|$. where f_z and f_x are the normal and tangential components of **f** and μ_i is a scalar friction coefficient. In the case of slip, the Coulomb model predicts $f_x = \pm \mu_i f_z$ such that the direction of the tangential component opposes the direction of sliding. For the sake of simplicity, we will assume that the static and dynamic coefficients of friction are identical.

3.1.2 Impacts

Impacts are inevitable parts of rigid body dynamics with unilateral contacts. Simple models of impact were developed by Newton and others long time ago. Nevertheless, a 'rigid impact' is a simplified representation of complicated interaction between Newtonian dynamics, shock-waves, viscoelastic material response and friction. The outcome of even a single impact is often very sensitive to model

details, and predicting it is notoriously difficult. This difficulty explains the variety of impact models used by the scientific community, and the failure of simple models to reliably predict the outcome of an impact [37] [152].

In Sec. 3.2, we focus on a phenomenological model of the motion, which does not require an impact model. Nevertheless, impacts are explicitly modelled in the numerical simulations. We assume frictionless impacts with a prescribed kinematic coefficient of restitution $0 < e < 1$ In Sec. 3.3, we consider stability against perturbations, which do not cause impacts, hence no impact model is needed here. In Sec. 3.4 we investigate the effect of state perturbations, which do cause impacts. An impact model of single-point impacts by Chatterjee and Ruina is used, which has two restitution parameters: a normal coefficient of restitution e and a tangential coefficient of restitution e_t. Details of the model are given in Sec. 3.4.

Simultaneous impacts are also crucial ingredients of rigid body dynamics. For example if an object slips or sticks at one point, while another point hits the ground, then simultaneous impacts occurs at the two points. The post-impact state is often a discontinuous function of the pre-impact state. The infinite sensitivity of simultaneous impacts poses a great challenge to modelling. In the numerical simulations of Sec. 3.2, an a priori modeling assumption is used to replace a simultaneous impact by a sequence of single-point impacts (see Appendix 5.5.2). The investigations of Sec. 3.4 avoid the need to model simultaneous impacts. All we need is the plausible assumption that every simultaneous impact absorbs some of the system's kinetic energy.

3.1.3 Contact modes

A rigid, frictional point contact is in one of the states of separation (F), stick (S), and slip, each of which is characterized by

different equations. In two dimensions, we can also distinguish between the positive and the negative directions of slip (P and N). In three dimensions, a continuous set of sliding directions exist, which can be characterized by a single discontinuous equation.

In order to decide, which contact mode is followed by a system, one has to follow a 3-step procedure. First, kinematically admissible candidates are identified using kinematic constraints. Then, the accelerations of the system are determined in each contact mode using additional equality constraints. Finally, consistency conditions have to be checked to decide, which mode yields a consistent solution. For example, the kinematic admissibility constraints of the F mode are

$$
\begin{aligned}
&either \quad z_i > 0 \\
&or \;\; \left(z_i = 0 \;\; and \;\; \dot{z}_i \geq 0 \right)
\end{aligned}
\tag{59}
$$

where z is the distance between the two interacting surfaces. The equality constraints are

$$
f_{i,x} = f_{i,z} = 0
\tag{60}
$$

where $f_{i,x}$ and $f_{i,z}$ are components of the contact force and the consistency condition is

$$
if \;\; z_i = \dot{z}_i = 0 \;\; then \;\; \ddot{z}_i \geq 0
\tag{61}
$$

For more details, see [36].

3.1.4 Hybrid dynamics

The motion of a rigid system consists of contact mode transitions (a source of non-smoothness of the continuous dynamics) and impacts (discrete state transitions). The event-driven numerical simulation scheme of Sec. 3.2 detects all of these events and switches to the relevant set of equations or discrete mappings every time. There exist other methods (the so-called time-stepping

schemes), which do not require event detection [152].

A peculiar property of rigid contact dynamics is that infinitely many impact events may occur in a finite time window. Indeed forward-time accumulation points of impacts of exponentially decreasing intensity [126] [193] (sometimes referred to as Zeno point or complete chattering sequence) represent the only generic mechanism by which a contact switches from F mode to sustained contact. The simplest example of chattering is the motion of a partially elastic bouncing ball. Naïve, event-driven simulation schemes get stuck forever while approaching a Zeno point [2] unless they detect this situation. Our simulation scheme includes a detection algorithm (see Appendix 5.5.2 for details).

Impacts may also accumulate backward in time [122], which is one of the generic mechanisms of transitioning to F mode from a sustained contact. 'Reverse chattering' is one of the two primary sources of instability in the sense of Lyapunov. (The second mechanism is ambiguity, which is explained in Sec. 3.1.7, below.) The stability conditions developed in Sec. 3.4 can be interpreted as sufficient conditions of not having reverse chattering dynamics.

3.1.5 Contact regularization

The concept of a rigid body is an abstraction, since every real solid undergoes small deformations under the effect of external loads. Some aspects of the dynamics of quasi-rigid bodies depend sensitively on these small deformations. For example, the contact forces of *statically indeterminate* structural systems may depend on microscopic deformations. Modeling dynamic phenomena associated with contacts such as break squeal and friction induced vibrations also require the consideration of deformations in the contact areas [80] [87]. The consistent contact modes predicted by rigid body theory may

also be unstable, which cannot be uncovered without modelling contact dynamics [98]. Finally, and most importantly for us, the stability analysis of an equilibrium may also require the modelling of compliance, as we explain in Sec. 3.1.8.

The deformations of a stiff body are often concentrated around contact points. This fact inspires the following modeling approach:

- the bodies are assumed perfectly rigid
- they are allowed to overlap in small regions around contact points
- there are contact forces between overlapping bodies. The forces represent repulsion and friction and are determined by a contact law. A general class of contact laws will be described and used in Sec. 3.3.
- the contact law has a positive compliance parameter ε. Larger values of ε correspond to a softer contact. The limit $\varepsilon \to 0$ corresponds to a quasi-rigid system hence it is of special interest.

3.1.6 Painlevé's paradox

In Sec. 3.1.3, we briefly reviewed the identification of the instantaneous contact mode of a system using inequality and equality constraints. Such an implicit formulation of the governing equations may suffer from non-existence and non-uniqueness. It can be proven using linear complementarity theory that there is always a unique consistent contact mode in the case of frictionless interactions, nevertheless this is not the case in the presence of dry friction. It was discovered in the late 19th century that several contact modes may be consistent simultaneously, or there may be no consistent mode at all [131] [129] [127]. These phenomena, which became known as Painlevé's paradoxes represent a major restriction of rigid models. Identifying systems prone to the paradoxes and predicting their behavior are subject to ongoing research today [36]. Non-existence
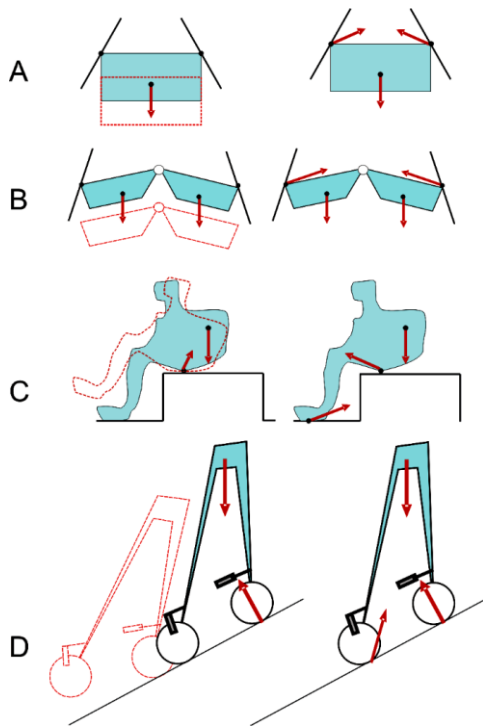
Fig. 38. Four examples of ambiguous equilibrium. A: a block between two planes; B: a two-element open kinematic chain between two planes; C: a rigid body resembling a person with a heavy backpack resting on a step-shaped terrain [137]. D: a 2-wheeled planar robot on a slope with one wheel freely rotating and the other one blocked. The objects are subject to their own weights and contact forces, both denoted by solid arrows. The non-static solutions (arrows and dotted lines representing forces and displacements, respectively) are shown on the left side, and the static equilibria are illustrated on the right side. A is force-closed, however the other 3 are not. B and D are statically determinate, whereas A and C are indeterminate.

is resolvable in simple systems by considering *grazing impacts* i.e. impacts where the pre-impact normal velocity of the contact point is 0. Nevertheless, non-uniqueness has no resolution within the framework of rigid body mechanics.

The Painlevé paradoxes are present in the problem investigated in Sec. 3.4. One of the strengths of our approach is its robustness in the presence of Painlevé paradoxes: our Lyapunov-like function shows a desired from of behavior along all possible solution trajectories, hence it is not necessary to

make a choice between solution alternatives.

3.1.7 Ambiguous equilibria

'Ambiguous equilibria' are important examples of solution indeterminacy. In this case, the static equilibrium is a consistent solution of the equations of motion, but it coexists with consistent accelerating motion departing from the same immobile initial state (Fig. 38). [131] [152] [104] [10] [75]. Ambiguity is an important phenomenon in robotics, because it often occurs if an object is grasped or if a robot moves over a complex terrain in the presence of friction [75]. The presence of ambiguity is generally considered an indicator of instability [131].

In Sec. 3.3 we perform a stability analysis of equilibria. One of the main results of the analysis is that even ambiguous ones may be stable in a certain sense, defined in Sec. 3.1.8. These results suggest that ambiguous equilibria may be acceptable in some applications, among which we discuss robotic grasping in more depth. Nevertheless, we will also see in Sec. 3.4 that ambiguity implies instability in the sense of Lyapunov [128] (for definition, see Sec. 3.1.8). Practically, this result means that ambiguous equilibria do not resist significant vibrations and similar dynamic perturbations.

3.1.8 Criteria of stable equilibrium

Rigid multi-body systems with unilateral point contacts are used as models in various fields of mechanical engineering and robotics including for example object manipulation, grasping, fixturing, and locomotion. The question of stability is a central issue in most applications. Various criteria are used in the engineering community to evaluate static configurations of mechanical systems. A large body of work has been devoted to clarifying the relation of these properties to each other and

to standard notions of stability in dynamical systems theory.

Most conditions of 'safety' or 'stability' can be classified into one of the following three groups:

- conditions, which are easy to check but do not have a clear implication with respect to the dynamic behavior of the system.
- conditions which are difficult to check, but they ensure a well-defined dynamic behavior.
- conditions, which are easy to check and have clear implications, but they are very restrictive.

To start with the first group, the traditional method of engineers is to look for *frictional equilibria*, for which given external forces can be balanced by contact forces consistent with the contact and friction laws [78] [32]. The interpretation of this concept as a stability condition is supported by the nature of dry friction. If an object with ≥ 2 contacts in 2D or ≥ 3 not collinear contacts in 3D is balanced by non-zero contact forces and frictional forces in the interior the friction cone (i.e. with strictly positive indicator function *S*), then infinitesimally small perturbing external forces can always be balanced by the adaptation of the contact forces. While this approach works perfectly in some simple cases (such as robotic walking on a horizontal terrain), it does not account for ambiguous equilibria, for which rigid body theory fails to give a well-defined prediction. This observation inspired the authors of [131] to propose *unambiguity*, also called *strong stability* (STRS) as a criterion of safe equilibria (Fig. 38). Unfortunately, they have not explored the implications of unambiguity from the point of view of dynamical systems theory. *Force closure* and *wrench resistance* [125] [119] are also popular criteria in the context of grasps. These are satisfied, if *arbitrary* external wrench (force and torque) can be balanced by appropriately chosen contact forces (within the bounds of the friction

model). Even though it may sound very restrictive, its relation to other notions is not completely understood. For example Fig. 38.A shows a system possessing force closure without STRS.

For criteria introduced so far, it is unclear, which set of perturbation they are stable against (if any), and how they respond to these perturbation. These important questions are addressed by standard notions of dynamical systems theory such as asymptotic stability (AS) and Lyapunov stability (LS) [3]. Frictional equilibria rarely posses AS because they have continuous sets of equilibrium, and they tend to move to a nearby point within the set when responding to perturbations. Nevertheless LS is an important tool. Let $|\dots|$ denote an arbitrary vector norm and let $\mathbf{q}(t)$ be the state vector of a dynamical system. In the case of a mechanical system, $\mathbf{q}$ consists of generalized coordinates and velocities. Then,

Definition 3.1.1 *An invariant point* $\mathbf{q}_0$ *of the dynamical system exhibits Lyapunov stability (LS) if for any* $\eta > 0$ *there exists* $\rho > 0$ *such that* $|\mathbf{q}(0)-\mathbf{q}_0| < \rho$ *implies* $|\mathbf{q}(t)-\mathbf{q}_0| < \eta$ *for all* $t > 0$.

LS implies STRS [128] because a small perturbation of an ambiguous equilibrium may result in divergent motion in that non-static contact mode, which is consistent together with equilibrium. Nevertheless, LS is more restrictive than STRS because an infinitesimal perturbation in state space may also induce loss of stability via reverse chattering in the presence of STRS. A slightly modified version of LS (called *finite time Lyapunov stability*, and defined as LS plus the additional requirement that perturbed trajectories converge to nearby equilibria) has been proposed [135] [128] [126] as a stability criterion for quasi-static robots.

The major drawback of LS in the context of equilibria of rigid bodies with unilateral contacts is the difficulty of assessment due to their complex dynamic behavior when an

equilibrium state is perturbed and contacts separate [152] [128] [126] [122] [171]. The work [126] was the first to investigate the model problem of a planar rigid body with 2 point contacts and those authors developed sufficient stability conditions. Our work in Sec. 3.4 will also address this model problem. Jen et al. [93] examined the Lyapunov stability of grasps, however they assume idealized finger control, which always prevents contact separation. Leine and van de Wouw [100] studied dynamic stability of continuous equilibrium sets, which is fundamentally different from the stability analysis of individual points within a set. The Lyapunov stability analysis of limit cycles [88] also requires different (and usually simpler) tools.

The third group of criteria in the robotics literature, includes *frictionless equilibrium*, which ensures LS in the presence of some friction [135]. *Form closure* [121],[20] (also called first-order immobility) and *second-order immobility* [162],[138], imply immobility solely by kinematic constraints [136]. The weakness of this third group of criteria is their limited applicability. For example, they are never satisfied by an object resting on a slope, as in the problem of Sec. 3.4

A different strategy of avoiding the difficulties associated with non-smooth and hybrid systems to take into account deformations of the components for example via contact regularization. Compliant systems exhibit smoother behavior, and they can be investigated by using the theory of smooth dynamical systems. In the context of grasping, it is common practice to treat local minimum points of a potential energy function as safe [120]. We choose this approach in Sec. 3.2 by investigating stability according to

Definition 3.1.2*: a rigid equilibrium configuration possesses static stability (STAS) if it is the $\varepsilon \to 0$ limit of a local minimum point of the potential energy function where ε is the compliance parameter of the regularized contact model.*

This property has well-defined dynamic consequences, similarly to the AS and LS. The significance of static stability from the point of view of dynamical systems theory is briefly discussed in Appendix 5.6, where we show that systems with static stability stay in a close neighborhood of their initial configuration in response to small variations of the external loads.

3.2 PHENOMENOLOGICAL MODELING OF MOTION AND POSE STATISTICS

In Sec. 2.4, we have reviewed common methods of industrial part feeding. It has been pointed out that the first step of part feeding is to drop objects onto a horizontal surface where they settle in one of their stable poses. The initial "pose selection" is followed by further steps of manipulation to achieve complete orientational ordering. The majority of the orienting devices can only rotate parts about a vertical axis [147],

but they cannot change their initial poses. Those parts, which are initially in a wrong pose, must be filtered out. Hence, the efficiency and the throughput of a feeder depends heavily on the probability of coming to rest in the pose preferred by the feeder.

This fact motivates investigations of the problem of 'pose statistics': given an object

with multiple stable poses, find the probabilities of coming to rest in each of the poses after being dropped from a considerable height with uncertain initial conditions. In Sec. 3.2, we address this problem in the following steps: in Sec. 3.2.1, we review and compare possibile methods to investigate pose statistics, and introduce the approach used in this work. In Sec. 3.2.2, we review existing estimators of pose statistics and propose several new ones. The estimators are evaluated and the most accurate ones are identified. In Sec. 3.2.3, we investigate the robustness of pose statistics against modelling assumptions, which is a crucial hypothesis when simple estimators are to be applied. Finally, open questions are discussed in Sec. 3.2.4.

3.2.1 Background

A Methods of obtaining part pose statistics

There are two straightforward approaches to obtain the pose statistics of an individual object: repeated physical experiments [158], and direct computer simulations [15] [157], [148], [163]. Experiments require the part to be manufactured as well as costly or tedious data processing. Computer simulation is much simpler, but generating a statistically reliable amount of pose statistics data by simulation is too slow for certain applications. Fast methods can be applied in computer-aided design software to provide the user with real-time feedback about the list of stable poses and the associated resting probabilities, while a part is being designed; they also facilitate the automated optimization of part shape through a large number of iterative steps. This demand inspired the development of simple estimators [25], [71], [187], [26], [116], [117], [40], [99], which provide approximate pose statistics with low computational cost.

The downside of the estimators is their unknown reliability. Several studies have compared their predictions with

experiments or simulations [25], [26], [71], [118], [162] and relatively low error rates have been reported. However, none of them has been benchmarked against more than a few specific objects or a restrictive class of shapes (e.g. square prisms). We attempt to fill this gap by

1. producing a benchmark dataset of pose statistics via the numerical simulation of random polyhedral objects (see points B,C below),
2. testing five existing estimators against data, and
3. proposing 3 new estimators.

Next, we discuss the challenge of obtaining a high-quality benchmark dataset.

B Benchmarking the estimators

Comparing and evaluating estimators requires a benchmark dataset. Both simulated and experimental datasets should be treated with caution because the difficulty of modeling impacts and friction [148]. The trajectory of an object falling onto a surface includes many impacts and the outcome of every single one depends on object shapes, sizes, materials, surface types, and initial conditions in a highly nontrivial way (see Sec. 3.1). Ideally, an experimental benchmark dataset should cover all possible combinations of these factors. At the same time, all these details should be known about the system for which the estimation is made. Similarly, the impact and friction models embedded in a simulation code should reflect all these factors. These requirements are unrealistic, i.e. from the point of view of accuracy, neither experiments nor simulations are satisfying.

Despite the sensitivity of an object's trajectory to the outcome of individual impacts, several researchers suggest that pose statistics are relatively robust against the variation of such factors. The deviation of simulated statistics from experiments for a small set of objects is below 3% [71]; the effect of the quality of the support surface is

also moderate (see [25], [26], [118] and Fig. 39). An attempt to rigorously prove the robustness of pose statistics is beyond the scope of this work, but more evidence for this observation will be presented in Sec. 3.2.3.

Motivated by the possibility to examine a large variety of object shapes, we use a simulated dataset as reference.

C The simulated dataset

The simulated objects are convex, traingular polyhedra. This is acceptable because the surface of any object can be approximated by a polyhedron; a concave object shows the same behavior as its convex hull (see Sec. 2.1); and a non-triangular face can be divided to triangles.

1057 random polyhedra have been generated with N=6665 stable poses altogether. The approximate values of the probabilities associated with each pose have been determined by simulating n=100 drop tests for each object (hence each probability is an integer multiple of 1/100). This procedure has been repeated three times, with three distinct values (0.2; 0.5; and 0.8) of the normal coefficient of restitution. The probabilities are collected in three vectors: $\mathbf{s}_{0.2}$=[$s_{1,0.2}$, $s_{2,0.2}$, …, $s_{N,0.2}$], $\mathbf{s}_{0.5}$=[$s_{1,0.5}$, $s_{2,0.5}$, …, $s_{N,0.5}$] and $\mathbf{s}_{0.8}$=[$s_{1,0.8}$, $s_{2,0.8}$, …, $s_{N,0.8}$], whereas the vector of all 3N probabilities is denoted by $\mathbf{s}$. The comparison of $\mathbf{s}_{0.2}$ and $\mathbf{s}_{0.8}$ sheds light on the effect of parameter ρ on pose statistics, and the whole dataset $\mathbf{s}$ is used to evaluate and to fit the estimators of pose statistics.
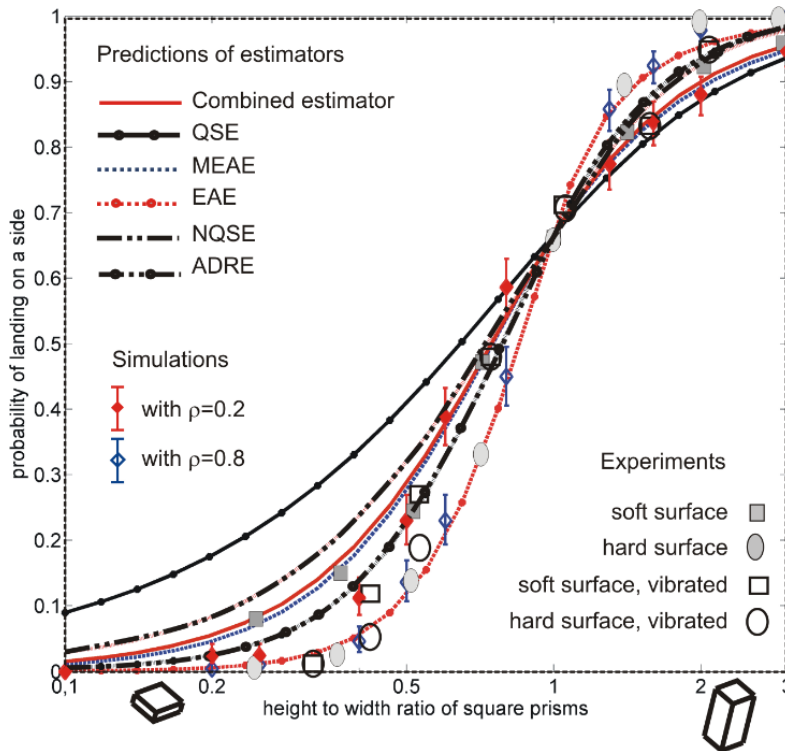

Fig. 39. Comparison of various predictions and measurements of the pose statistics of square prisms. The four sides of the prisms are treated as identical, similarly to the two bases. The diagrams show the probabilities of landing on the sides. Continuous curves show the predictions of various estimators. Diamonds with error bars are simulation results with the model of this paper and their 95% confidence intervals. Squares and circles indicate experimental results of [26] and [118]. Each point is based on 500 or more trials. See Sec. 3.2.3 for details

For the sake of simplicity, interactions between the objects and the underlying surface are modeled as perfectly frictionless. This simplification is supported by the above discussed robustness of pose statistics.

More detailed descriptions of the object generation and of the numerical solver are presented in Appendix 5.5.1.

D Measuring the quality of an estimator

To evaluate the estimators, the set $\mathbf{s}$ of simulated probabilities is compared with the predictions $\mathbf{e}$=[e_1,e_2,…e_{3N}] of an estimator and with the unknown exact probabilities $\mathbf{p}$=[p_1,p_2,…p_{3N}]. The distinction between $\mathbf{p}$ and $\mathbf{s}$ is necessary because of the relatively low number (n=100) drop tests performed with each
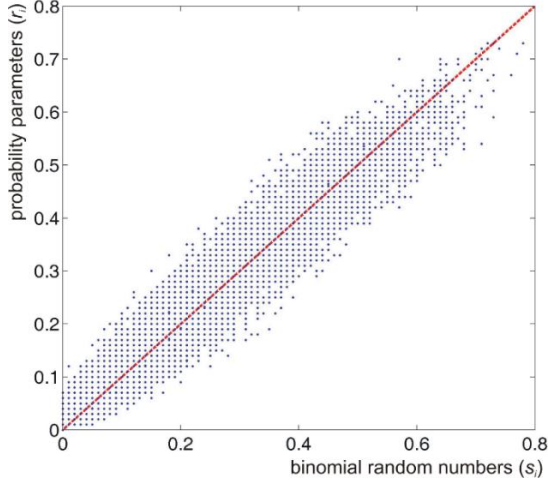
Fig. 40. Illustration of the noise caused by the finiteness of *n* (see main text for explanation)

specimen. Mathematically speaking, the elements of **s** are random numbers drawn from binomial distributions with *n* trials and probability parameters $p_1, p_2, \ldots p_{3N}$.

Let σ denote the root mean square deviation of two datasets (**α**, **b**) of equal size *N*:

$$\sigma^2(\mathbf{\alpha}, \mathbf{\beta}) \overset{def}{=} N^{-1} \sum_{j=1}^{N} \left(\alpha_j - \beta_j \right)^2 \qquad (62)$$

The deviation of **e** and **s** is caused partly by the finiteness of *n* and partly by the imperfectness of the estimator. The two components can be partitioned as

$$\sigma^2(\mathbf{e}, \mathbf{s}) =$$
$$= (3N)^{-1} \sum_{j=1}^{3N} \left(e_j - s_j \right)^2$$
$$= (3N)^{-1} \sum_{j=1}^{3N} \left(e_j - p_j + p_j - s_j \right)^2 \qquad (63)$$
$$= \sigma^2(\mathbf{e}, \mathbf{p}) + \sigma^2(\mathbf{p}, \mathbf{s}) -$$
$$\underbrace{\ldots \frac{2}{3} N^{-1} \sum_{j=1}^{3N} \left(e_j - p_j \right)\left(s_j - p_j \right)}_{\overset{def}{=} C}$$

where $\sigma(\mathbf{e}, \mathbf{p})$ measures the error of the estimator; $\sigma(\mathbf{p}, \mathbf{s})$ represents noise in the simulation results due to the finiteness of *n*, and the last term *C* is the covariance of the two errors.

The value of $\sigma(\mathbf{p}, \mathbf{s})$ can be estimated using the formula of the variance of binomially distributed random variables:

$$\sigma^2(\mathbf{p}, \mathbf{s}) \approx (3N)^{-1} n^{-1} \sum_{j=1}^{3N} p_j (1 - p_j) \qquad (64)$$

The equality marked by '≈' is approximate due to the finiteness of *N* (though the error terms are neglected as *N* is much larger than *n*). As a further approximation, the unknown values p_j in (64) are replaced by the known values s_j, yielding $\sigma^2(\mathbf{p}, \mathbf{s}) \approx 0.0327$.

The term *C* in (63) is much smaller than $\sigma^2(\mathbf{p}, \mathbf{s})$ unless the estimator is overfitted to the noisy observations. Extreme overfitting, i.e. $e_j = s_j$ would yield $C = 2\sigma^2(\mathbf{p}, \mathbf{s})$. Some estimators examined in this work are based on physical intuition rather than on curve fitting; others have a small set of parameters fitted to a relatively large set of data. Hence, overfitting can be excluded, and *C* is negligible. Thus the error of the estimator can be approximated by

$$\sigma(\mathbf{e}, \mathbf{p}) \approx \left[\sigma^2(\mathbf{e}, \mathbf{s}) - 0.0327^{\,2} \right]^{1/2} \qquad (65)$$

This quantity is used to compare and to evaluate the estimators.

If **p** was known, a graphical illustration of the partitioned noise term $\sigma(\mathbf{p}, \mathbf{s})$ could be obtained by drawing random numbers $r_1, r_2, \ldots r_{3N}$ from binomial distributions with *n*=100 trials and probability parameters $p_1, p_2, \ldots p_{3N}$; and by plotting them against the probability parameters. Unfortunately, *p* is unknown, but one can use the approximations s as input instead. The (r_i, s_i) points are off-diagonal (Fig. 40) due to the finiteness of *n*. Later, several plots of estimated vs. simulated results will be shown (Fig. 41). The points in these plots are even more off-diagonal due to estimator errors. Fig. 40 can be interpreted as the plot

of a 'perfect estimator', which predicts **p** without any error.

3.2.2 Estimators of pose statistics

Now we proceed with an overview of existing estimators, and with the development of three new ones. Every estimator is evaluated against the benchmark dataset. We also discuss outlier cases, i.e. situations where simple estimators show a bad performance.

A Existing estimators

In one of the first papers on pose statistics, Boothroyd [25] proposed an estimator based on the extension and the depth of the potential energy valleys associated with the stable poses of an object (energy barrier method). The definition of the 'energy barrier' was given originally only for cylinders and square prisms. As it is not clear how to extend it to an arbitrary shape, this concept is not examined here.

Another early work on the topic [26] hypothesized that the probability of resting on a facet of the polyhedron is roughly proportional to the centroid solid angle Ω_i of the facet from the center of mass. This is motivated by the fact that in a uniformly distributed random pose, the probability that the centroid is above facet i would be $\Omega_i/4\pi$.

The solid angle of a surface embedded in 3D space from a point O is the area of the central projection of the surface to a unit sphere S_O centered at O. There are closed formulas for the solid angle of a spatial triangle [165], which can be used to find the centroid solid angles of a facet of the polyhedron.

As we have seen in Chapter 2 resting on a facet is not necessarily an equilibrium, nevertheless this estimator assigns positive probability to every facet. This can be corrected by assuming that the probabilities
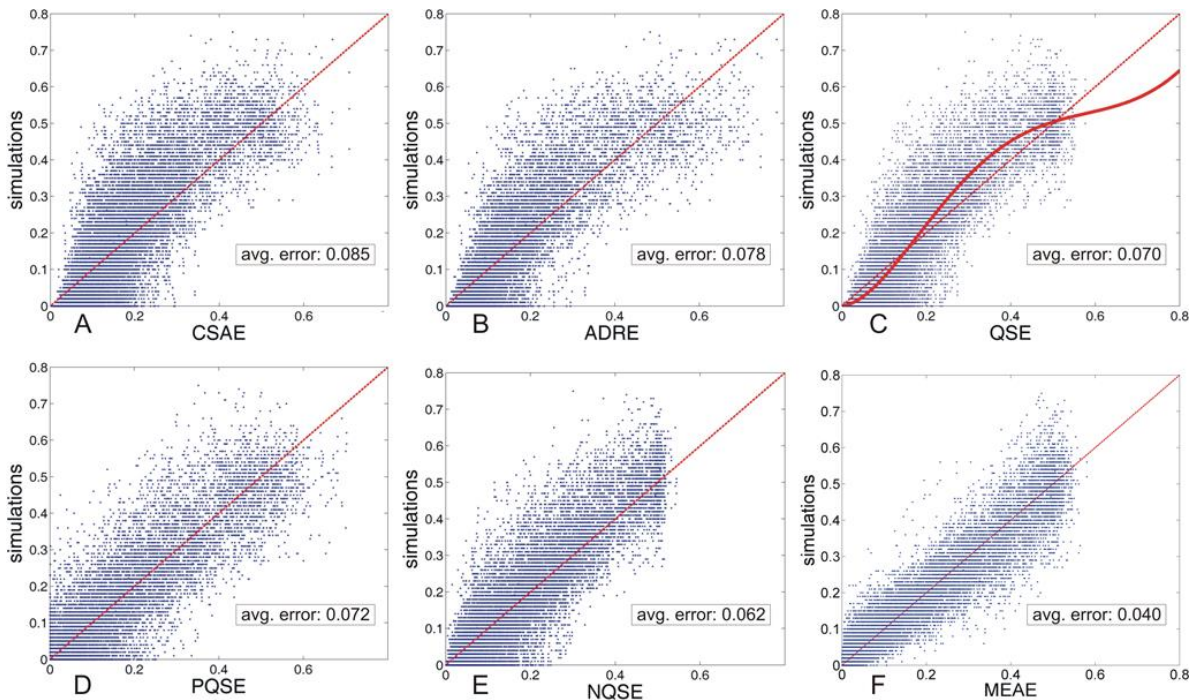
Fig. 41. Comparison of pose statistics estimators. Each plot corresponds to an estimator discussed in the thesis. Each individual dot in the plots shows the probability of coming to rest in a specific stable pose of a random polyhedron based on 100 simulations (vertical coordinate) vs. the prediction of the same probability provided by the estimator (horizontal coordinate). Points close to the main diagonal are indicators of a better estimator. Nevertheless, deviations from the main diagonal are caused partly by other factors (Fig. 40, Sec. 3.2.1.D). The solid curve in panel C is a parametric function fitted to the data points, which is used in Sec. 3.2.2.B

associated with non-equilibrium facets are 0, and those of stable facets are proportional to their centroid solid angles:

$$e_i = \Omega_i / \sum_{stable\ facets} \Omega_j \qquad (66)$$

This is referred to as centroid solid angle estimator or CSAE. A diagram of the CSAE analogous to Fig. 40 is plotted in Fig. 41.A. The latter point-cloud occupies a wide region around the main diagonal, which indicates a significant estimator error. The error of the CSAE calculated by (65) is 0.085. The surface areas of facets can also be used as part pose estimator in a similar manner [116]. This estimator yields similar

results to the CSAE with higher error (0.112).

References [116], [117], and other works of the same authors investigate the hypothesis that the probability of landing on a stable facet is proportional to the ratio Ω_i/d_i where d_i is the distance of the facet from the center of mass (angle-distance ratio estimator or ADRE). The estimated probabilities are obtained by a formula analogous to (66). The error of the ADRE is 0.078, i.e. it is slightly better than the CSAE (Fig. 41.B)

In [187], the CSAE is complemented by a physically inspired algorithm to distribute the probabilities associated with unstable facets among stable ones. The CSAE is used in [187] to estimate the initial probability of landing on a given facet as the object is dropped. If resting on the initial facet is not an equilibrium pose, the object is assumed to topple over one of its three edges to an adjacent facet quasi-statically. The toppling continues until a stable facet is reached. A simple physically inspired rule is chosen to determine, which way the polyhedron topples. This model of toppling motion can be represented by an acyclic directed 'toppling graph' (its vertices correspond to facets of the polyhedron, and its edges indicate the directions of toppling), on which the state of the object evolves. The initial probability distribution predicted by

the CSAE is propagated along the graph towards stable states to obtain the quasi-static estimator (QSE, Fig. 41.C), which has a lower error (0.070) than the CSAE.

By examining the experimental pose statistics of a few objects, several authors have noticed that the previously described estimators tend to underestimate the probabilities associated with large facets and overestimate the likelihood of landing on smaller ones. This tendency – also reflected by the nonlinear trends of the point clouds in Fig. 41.A-C – was attributed by [71] to the fact that an object resting on a small facet is much more sensitive to perturbations than one resting on a large facet. To address this issue, the QSE was modified in the following way [71]: the initial probabilities (coming from CSAE) were redistributed between each pair of adjacent facets according to a simple phenomenological rule that increased the initial probability associated with large facets. The modified initial probabilities were propagated down the toppling graph (as in the case of the QSE) to obtain the predictions of the perturbed quasi-static estimator (PQSE). The PQSE was tested against experiments and simulations with three specific objects. It was found to outperform the QSE, indeed its performance was comparable to that of direct numerical simulations. When applied to our set of random objects, this estimator assigns negative initial probabilities to some small facets, which is meaningless. In such situations, we reduce the amount of redistribution to keep the initial probabilities nonnegative. The predictions of the PQSE (Fig. 41.D) lack the nonlinear trend of the CSAE however the estimator error remains roughly the same (0.072).

B *Improving the performance of estimators by nonlinear fitting*

Inspired by the initial observations of [71], we examine a purely mathematical method to avoid the overestimation of probabilities
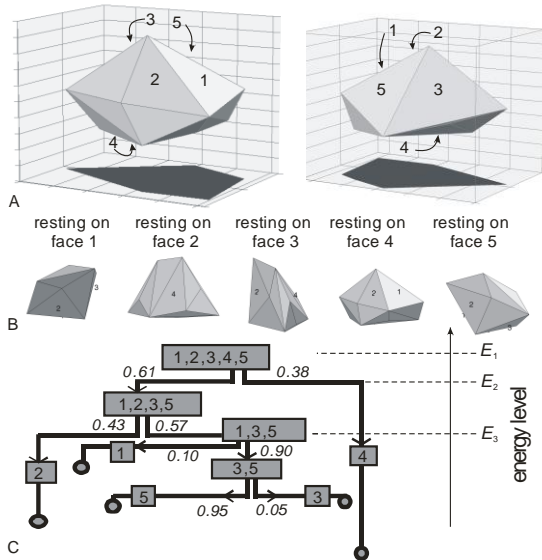
Fig. 42.A: front (left) and rear (right) view of one of the polyhedra used in the simulation. Resting on any of the 5 enumerated faces corresponds to a stable pose. B: the stable poses of the polyhedron C: the splitting graph of the polyhedron with transition probabilities. There are four critical energy levels, at which the reachable set splits. According to (68), the critical energy levels are those at which a saddle point of the function $R(\mathbf{u})$ leaves the reachable set. Circles represent the potential energy levels at which a component of the reachable set disappears.

associated with small faces. The results e_j of the QSE estimator are used as basis. The parametric nonlinear function

$$f(x) = \\ ...x + x(1-x)\left(c_0 + c_1 x + c_2 x^2 + c_3 x^3\right) \quad (67)$$

is fitted to the points of Fig. 41.C to minimize the variance $\sigma^2(f(\mathbf{e}), \mathbf{s})$. The fitted values are c_0=-0.874; c_1=8.03; c_2=-16.3; c_3=7.70. It is hypothesized that the probabilities of landing on various faces of a polyhedron are proportional to $f(e_j)$, leading to a formula similar to (66). The error of the new 'nonlinear quasi-static estimator' (NQSE) is significantly lower (0.062) than any of the previous ones (Fig. 41.E).

C EAE: a new estimator

The philosophy behind the QSE estimator and its variants was to get rid of complex dynamics by considering a highly damped, quasi-static model of the moving object, and to derive estimations from the 'tamed' model. The new estimator presented here attempts to capture the statistical properties of the complex dynamics instead of neglecting it. The main idea of the estimator is illustrated by Fig. 42.

Let $E(t)=U(t)+K(t)$ denote the total mechanical energy, the potential energy, and the kinetic energy of the object as functions of time. The reference level of the potential energy is the supporting surface. The object may not penetrate into the surface, yielding $U(t) \geq mgR(\mathbf{u}(t))$ where $\mathbf{u}$ is a unit vector representing a pose and R is the support function (as defined in Sec. 2.1). At the same time, $K(t)$ is nonnegative. These inequalities imply

$$R(\mathbf{u}(t)) \leq E(t) / (mg) \quad (68)$$

i.e. those poses for which $R(\mathbf{u})$ exceeds a certain threshold, are not reachable by the object. The initial mechanical energy of the object is enough to make every pose reachable. However its motion is accompanied by energy absorption, which is assumed to happen either continuously or through small steps. The set of reachable poses shrinks gradually (Fig. 43). The topological changes of the reachable set have been investigated thoroughly in [94]. The next paragraph gives a brief description of these results. The function R has s local minima corresponding to the stable poses. Accordingly, there are s-1 energy levels at which the number of disconnected components of the reachable set increases by one. The splitting events occur at saddle points of the function $R(\mathbf{u})$ (but not necessarily all saddles are involved in splitting events, see top panels of Fig. 43. The fragmentation of the reachable set can be described by a 'splitting graph' (Fig. 42.C) in which rectangular nodes represent

connected components of the reachable set at various energy levels. Each node is labelled by the list of stable poses contained by that component. Pairs of edges represent splitting events, and their positions show the corresponding energy levels. Those energy levels, at which a component disappears, are marked by circle-shaped nodes at the bottom of the graph; however these values are not used by the estimator.

The mechanical energy and the actual pose of the object together determine a node of the splitting graph. This node is referred to as the discrete state of the object. During its motion, the discrete state of the object changes from time to time. The *Energy absorption estimator* (EAE) is based on a phenomenological description of this process. A Markov chain is considered on the graph. The transition probabilities are assumed to depend on geometric properties of the examined object. Specifically, if a component Γ_i of the reachable set splits to two parts (Γ_{ia}, Γ_{ib}) at some energy level E^*, the transition probabilities π_{ia}, π_{ib} are assumed to be proportional to the centroid solid angle of the two components at energy level E^*:

$$\pi_{ia} = \Omega(\Gamma_{ia})/(\Omega(\Gamma_{ia}) + \Omega(\Gamma_{ib}))$$
$$\pi_{ib} = \Omega(\Gamma_{ib})/(\Omega(\Gamma_{ia}) + \Omega(\Gamma_{ib}))$$

(69)

An algorithm to identify the connected components of the reachable set at the energy levels corresponding to saddles of $R(\mathbf{u})$ is outlined in [94]. The complexity of this algorithm is linear in the number of vertices of the polyhedron. In the current work, I use a different algorithm, which is described in Appendix 5.5.2 and in [168]. The centroid solid angles Γ_{ia}, Γ_{ib} can be determined in a straightforward way due to the facts that level curves of R are composed of circular arcs (Fig. 43) and that there are closed formulas for the solid angles of a triangle [165] and of a circular sector with center C, provided that the plane of the sector is perpendicular to OC [107].

Initially, the object's discrete state corresponds to the node at the top of the graph with probability 1. Eq. (69) is used to calculate the likelihood of reaching each other discrete state. Among these, the probabilities associated with the absorbing states at the bottom of the tree (each corresponding to one stable pose) are the predictions of the EAE estimator.

The error of the estimator is 0.068. In comparison with previous results, this error level is not very impressive. Nevertheless, much better results are obtained if the support function R is replaced by the distance function r (Sec. 2.1) in (68). Even though the author has no physical argument why such a modification should be beneficial, the error of the *Modified energy absorption estimator* (MEAE) is only 0.040 (Fig. 41.F).
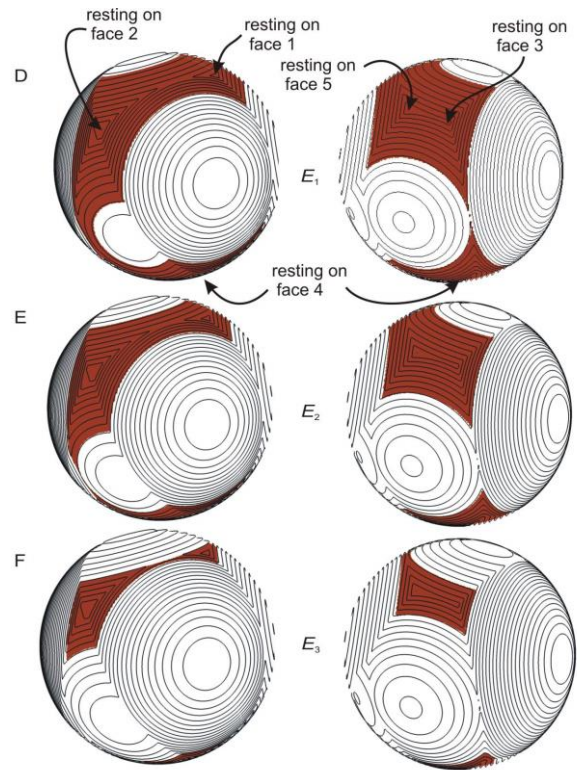

Fig. 43. Front (left) and rear (right) views of the sphere representing the space of poses, with level curves of the $R(\mathbf{u})$ function. The shaded areas are the set of reachable poses at three energy levels (dashed lines in panel C). E_1 is not critical because the reachable set remains connected, but E_2 and E_3 are critical.

Table 3.2.1: comparison of the estimators

	name	average error	largest observed deviation from simulation
existing estimators	CSAE	8.5%	43.5%
	ADRE	7.8%	40.9%
	QSE	7.0%	45.8%
	PQSE	7.2%	42.5%
new estimators	NQSE	6.2%	44.9%
	EAE	6.8%	58.0%
	MEAE	4.0%	32.7%
	combined	3.6%	32.0%

The run time of a MATLAB-based implementation of the MEAE estimator is between 0.1 and 1.5 second depending on the complexity of the polyhedron. The run time of the EAE estimator is slightly higher. The code has not been optimized for speed.

For most polyhedral objects, the computational complexities of the estimation algorithms are $O(v)$ where v is the number of vertices (Appendix 5.5.2 , [168]). This is lower than the $O(v\log v)$ complexity of finding the convex hull.

D Combining several estimators

The NQSE and the MEAE estimators capture different aspect of the dynamics. It is likely that improved results can be obtained by combining them. Specifically, parameter c of the convex combination

$$\mathbf{e}_{combined} = c\mathbf{e}_{MEAE} + (1-c)\mathbf{e}_{NQSE} \qquad (70)$$

has been tuned to minimize $\sigma^2(\mathbf{e}_{combined}, \mathbf{s})$. The error of the combined estimator with c=0.75 shows further reduction (0.036). Linear and nonlinear combinations of more than 2 estimators have also been examined, however they did not yield significantly better results. This is probably caused by the

strong correlation of the predictions of different estimators.

E Outlier cases

Estimators produce exceptionally large errors in some cases. The maximum deviations of various estimators from results obtained by simulation are summarized in Table 3.2.1. The best performance is that of the new combined estimator. We also examined the 3 largest observed deviations of the combined estimator: 32.0%; 31.9%, and 29.5%. The finiteness of n is partly responsible for these outlier cases. To separate this effect, 1000 drop tests (instead of 100) were simulated with those 3 particular objects that produced the outlier cases. The errors of the estimator were reduced to 20.8%, 22.5%, and 17.6%. This result suggests that the combined estimator never or extremely rarely produces errors significantly exceeding 20%.

3.2.3 Verification of the results

It is a crucial assumption that pose statistics are robust against modelling errors. The detailed discussion of this question is beyond the scope of this thesis, but the plausibility of the assumption is illustrated by a systematic examination of the coefficient of restitution ρ and by a comparison of simulated results with experiments under various conditions.

A Sensitivity to the coefficient of restitution

The deviation of the simulated datasets obtained with ρ=0.2 and ρ=0.8 is $\sigma(\mathbf{s}_{0.2}, \mathbf{s}_{0.8}) = 0.0728$. This can be partitioned similarly to the techniques described in Sec. 3.2.1 D. The Biennaymé formula for the

variance of sums of random variables; the connection between the raw moments and the central moments of a probability distribution; and the formula of the variance of a binomially distributed random variable yield

$$\sigma^2(\mathbf{s}_{0.2},\mathbf{s}_{0.8}) \approx \sigma^2(\mathbf{s}_{0.2},\mathbf{p}_{0.2}) + \sigma^2(\mathbf{p}_{0.2},\mathbf{s}_{0.8})$$

$$\approx \sigma^2(\mathbf{s}_{0.2},\mathbf{p}_{0.2}) + \sigma^2(\mathbf{p}_{0.2},\mathbf{p}_{0.8}) + \sigma^2(\mathbf{p}_{0.8},\mathbf{s}_{0.8})$$

$$\approx N^{-1}n^{-1}\sum_{j=1}^{N} p_{j,0.2}(1-p_{j,0.2}) + \sigma^2(\mathbf{p}_{0.2},\mathbf{p}_{0.8}) \quad (71)$$

$$+ N^{-1}n^{-1}\sum_{j=1}^{N} p_{j,0.8}(1-p_{j,0.8})$$

The unknown values $p_{j,\rho}$ in (71) are replaced by the known values $s_{j,\rho}$, which lets one estimate the deviation of the unknown 'exact' datasets as

$$\sigma(\mathbf{p}_{0.2},\mathbf{p}_{0.8}) \approx \left(\sigma^2(\mathbf{s}_{0.2},\mathbf{s}_{0.8}) - N^{-1}n^{-1}\sum_{j=1}^{N} s_{j,0.2}(1-s_{j,0.2}) - N^{-1}n^{-1}\sum_{j=1}^{N} s_{j,0.8}(1-s_{j,0.8}) \right)^{1/2}$$

$$= \left(0.0728^2 - 0.0321^2 - 0.0332^2\right)^{1/2} = 0.0563 \tag{72}$$

Hence, the effect of the coefficient of restitution on pose statistics is moderate (on average: 5.6%) despite the fact that the trajectory of an individual falling object can fundamentally change its character in response to variations of ρ. This result confirms the robustness of pose statistics against modeling errors.

B Comparison with experiments

The pose statistics of square prisms of various length-to-width ratio have been investigated experimentally among others by [26] and by [118]. Both works report on drop tests with hard and soft support surfaces. In [118], the surface is vibrated. The results of these experiments are summarized in Fig. 39. The predictions of various estimators and simulation results are also shown.

As already noted by [26], the quality of the support surface has significant influence on the experimental results. Depending on the length/width ratio, the effect of the surface type on the results is between 0 and 15%. This is comparable to the effect of the coefficient of restitution found in Sec. 3.2.3 A.

The simulation results agree well with experiments obtained with a hard surface, but they deviate significantly from the soft surface results. This observation suggests that our results do not apply very well to objects dropped onto soft surfaces, and further work using a different benchmark dataset is desirable in that case.

Finally, comparison of the estimators reveals a somewhat surprising result. The combined estimator shows the best fit to the benchmark dataset, but it has relatively large errors (up to 17% for some length/width ratios and surface types) in the case of square prisms. The ADRE and the EAE perform significantly better for this particular class of objects.

3.2.4 Conclusions

We have performed a systematic comparison and evaluation of existing estimators of pose statistics. It was found that the average errors of these estimators are between 7 and 11% (Table 3.2.1). Such an error level can be tolerated in some situations, but estimations based on direct numeric simulation are significantly more accurate (though not perfectly accurate as discussed in Sec. 3.2.1 B). The increasing

availability of cheap computation makes simple estimators less attractive, nevertheless there are applications for which dynamic simulation is too slow. For this reason, estimators with low error rates are of practical interest. In the current work, a new estimators has been proposed with average error 3.6% and maximum error near 20% (based on a large, random dataset).

To measure the performance of the estimator, simulations with a frictionless model have been used as reference. The effect of modeling errors and the influence of experimental conditions on pose statistics have been tested in several ways. Large variations of the coefficient of restitution change the probabilities by 5.6%

on average. According to earlier experiments with square prisms, the quality of the support surface has an effect of similar magnitude. On the one hand, these observations indicate that further significant reduction in estimator error is not possible without treating the coefficient of restitution and other parameters (e.g. friction coefficient) as known. We do not examine such extensions, because these parameters are often unknown in real-life situations. On the other hand, understanding the parameter-dependence of pose statistics requires further effort (e.g. the systematic variation of physical parameters in physical experiments or in simulations with a more detailed model).

3.3 COMPLIANT CONTACTS AND STATIC STABILITY OF EQUILIBRIA

We now turn our attention towards the stability analysis of equilibria. The first notion to be investigated is *static stability*, which was defined in Sec. 3.1. It has been pointed out that static stability is a relatively weak form of stability, nevertheless it has practical relevance for systems, which operate in an environment free of significant vibrations and other dynamic perturbations. Robotic grasping is one of the natural fields of application, as we explain in Sec. 3.3.1, below. The basic assumptions and some new notation are introduced in Sec. 3.3.2. A model of nonlinear, viscoelastic, spatial or planar, frictional or frictionless contacts is presented in Sec. 3.3.3. Our main contribution is proving static stability for a wide class of systems by investigation of the Taylor expansion of the potential energy (Sec. 3.3.4). An application of the new theorem in the field of quasi-static locomotion is outlined in Sec. 3.3.5, which is followed by a brief summary and discussion of other fields of application (Sec. 3.3.6).

3.3.1 Background

For long time, research in robotic grasping was focusing on the problem of a single rigid body held by a gripper. The static stability of a rigid body with stiff, linear elastic contacts was analyzed by [120] [111] [89]. They found that the stability of many but not all grasps is influenced by the curvatures of the object and the gripper at the contact points. However, *Theorem 4* of [89] is a sufficient condition of stability relying only on first-order kinematics, i.e. no curvature effects. What they show is that every object grasped by rigid fingers is stable if the arrangement of fingers ensures that any infinitesimal motion of the object would cause either penetration into a finger, or contact slip or contact separation. The present work generalizes this result to multi-body systems and kinematic chains (rigid bodies connected by hinges). At the
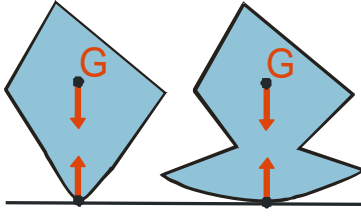
Fig. 44. An unstable (left) and a stable (right) system violating condition (ii). Their stabilities are determined by the curvatures at the contact point. G is the center of gravity.

same time, the contact interactions are allowed to be nonlinear elastic or even visco-elastic. These extensions are motivated primarily by the growing interest in grasping non-rigid objects [38] [74] [192] and by the complex nature of real contact interactions [21],[146]. The stability condition presented in this thesis was the first one for complex objects (consisting of multiple rigid components), which does not require knowing the curvatures at the contact points.

In order to apply the notion of static stability, the system under investigation must have a continuous potential energy functions associated with the contact forces and the external loads. Contact interactions between ideally rigid objects are characterized by discontinuous potentials therefore we consider small deformations of the system. In addition, only conservative loads and elastic contact interactions induce potential energy functions, which is quite restrictive. Nevertheless, it is possible and physically reasonable to use our definition of static stability in the case of forces, which can be decomposed into the sum of conservative components (forces with a potential) and dissipative components (i.e. forces which do not increase the total energy of the system). In order to cover a wide range of physical phenomena (most notably viscoelastic material response), contact forces and loads are allowed to have dissipative components. For the same reason, elastic contact forces may be nonlinear. The resulting contact model is more realistic than the linear spring models often used elsewhere.

3.3.2 Problem statement and main results

Let **q** denote the vector of generalized coordinates of a system. We will prove the following sufficient condition of static stability:

Theorem 3.3.1*: a static equilibrium configuration **q**=**q**$_0$. of a rigid multibody system with well-defined contact normals possesses static stability if the following criteria are met:*

(i) none of the frictional contact forces is exactly at the verge of slipping in the static equilibrium state; and none of the frictionless ones is exactly at the verge of detachment (i.e. S>0 for all contacts)

(ii) the constraints of the system restrain its motion in such a way that any infinitesimal displacement of the system would cause penetration or separation at some contact; or contact slip at a frictional contact.

*(iii) the external loads are conservative or dissipative in the following sense: there exists a potential energy function P$^{(ext)}$(**q**) such that if the system moves from configuration **q**$_1$ to **q**$_2$, the work of the external forces is not bigger than P$^{(ext)}$(**q**$_1$)- P$^{(ext)}$(**q**$_2$).*

If condition (i) is not satisfied, the slightest perturbation may cause slipping or detachment, beyond which our model fails to describe the motion of the system. Condition (iii) is important because a system subject to non-dissipative loads may gain energy by the work of external loads, which may sustain and magnify internal vibrations and destabilize the equilibrium. Condition (ii) can be visualized in the following way: if frictional contacts are replaced by hinges (to prevent slipping and separation) and frictionless ones by bilateral sliders (to prevent separation), then the system must become rigid (instead of being

a mechanism). Due to the physical duality of forces and displacements, this is also equivalent to having a full-rank wrench matrix of constraining forces [89]. If condition (ii) is not satisfied, the stability of the system depends on the curvatures at the contacts as demonstrated by [89] for a single rigid body, see also Fig. 44.

3.3.3 Compliant contact model and rescaled time

We have introduced friction models and conditions of stick in Sec. 3.1. Now, the compliant contact law for stick interaction in three dimensions is presented in detail. The two objects involved in a contact interaction are marked by lower indices 1 and 2. When they establish contact, the first points of overlap on their respective boundaries (P_1 and P_2) are marked as reference points. As the contact deforms, the two reference points (attached to the two objects) move away from each other, while the direction of the contact normal $\mathbf{n}$ may also change. It is not specified here how the contact normal of a compliant contact (with some overlap between the interacting rigid objects) should be defined. There are several appropriate definitions provided that the contact normal of the original rigid system is well-defined (condition (ii)).

Let $\Delta\mathbf{r}=[\Delta n \ \ \Delta\mathbf{t}^{\mathrm{T}}]^{\mathrm{T}}$ denote the contact deformation where the scalar Δn is the normal component of the vector pointing from P_1 to P_2; $\Delta\mathbf{t}$ is a 2-vector of tangential components. The contact force $\mathbf{f}$ exerted by object number 2 on number 1 also consists of normal and tangential components: $\mathbf{f}=[\ f_{\mathrm{n}} \ \mathbf{f}_{\mathrm{t}}^{\mathrm{T}}]^{\mathrm{T}}$ where $\mathbf{f}_{\mathrm{t}}$ is a 2-vector. $\mathbf{f}$ is assumed to be the sum of an elastic (conservative), and a viscous (dissipative) term:

$$\mathbf{f} = -\operatorname{grad} \tilde{U}\left(\Delta\tilde{\mathbf{r}}\right) + \mathbf{f}_{dis}\left(\Delta\tilde{\mathbf{r}}, \Delta\tilde{\mathbf{r}}'\right) \quad (73)$$

where $\Delta\tilde{\mathbf{r}} = \varepsilon^{-1}\Delta\mathbf{r}$ is the contact deformation scaled by the compliance parameter $0<\varepsilon<<1$ ($\Delta\tilde{\mathbf{r}}$ and $\Delta\mathbf{r}$ are functions of the generalized coordinates $\mathbf{q}$);

' means derivative with respect to scaled time $\tilde{t} = \varepsilon^{-1/2}t$. The scaling factors reflect the fact that the deformations of a quasi-rigid contact are O(ε) and the internal vibrations of a quasi-rigid contact in stick state have O($\varepsilon^{1/2}$) natural time scale. The scaling enables one to characterize a quasi-rigid contact by regular functions $\tilde{U}$ and $\mathbf{f}_{\mathrm{dis}}$, which are independent of ε. $\tilde{U}\left(\mathbf{x}\right)$ is the scaled elastic energy function of the contact, which is assumed to be smooth in the range of interest. Because of the scaling factor, the elastic internal energy of the deformed contact region is $U = \varepsilon\tilde{U}\left(\Delta\tilde{\mathbf{r}}\right)$. $\tilde{U}$ can implement any nonlinear elastic response. Elastic contacts have positive stiffness, which means that the corresponding $\tilde{U}$ is strictly convex, with a positive definite Hessian. $\mathbf{f}_{\mathrm{dis}}$ is a smooth dissipative term (i.e. a force which never does positive work on the object). $\mathbf{f}_{\mathrm{dis}}$ is a function of the scaled contact deformation and its scaled rate of change; it is required that $\mathbf{f}_{\mathrm{dis}}=0$ if $\Delta\tilde{\mathbf{r}}' = 0$, hence only the elastic force components are active in immobile states of the system. The limits of stick interactions are determined by the indicator function S introduced in Sec. 3.1.

Two-dimensional frictional contacts are modelled in the same way, but in this case $\Delta\mathbf{t}$ and $\mathbf{f}_{\mathrm{t}}$ are scalars rather than 2-vectors.

Frictionless contacts can also be modeled in an analogous way. In this case, the contact deformation $\Delta\mathbf{r}(\mathbf{q})$ should consist only of the scalar $\Delta n(\mathbf{q})$ as the tangential relative motion of the two interacting objects is irrelevant; $\mathbf{f}_{\mathrm{dis}}$ and $\mathbf{f}$ also become scalars as they do not have tangential components. In the frictionless case, an indicator function S can be defined such that $S=0$ indicates contact separation. A good choice for S in the case of a frictionless contact is $S(\mathbf{f}) = \mathbf{f}$ (recall that $\mathbf{f}$ is now a scalar).

3.3.4 Potential energy of the compliant system

The contacts are enumerated by trailing upper indices in parentheses. The contact deformation vector (frictional contact) or scalar (frictionless contact) of contact $^{(i)}$ is expanded into Taylor series in $\mathbf{q}$ at $\mathbf{q}=\mathbf{q}_0$:

$$\Delta\mathbf{r}^{(i)} = \sum_{k=1}^{\infty} R_k^{(i)}(\mathbf{q}-\mathbf{q}_0) \qquad (74)$$

where $R_k^{(i)}(\mathbf{q})$ denotes an arbitrary k-th order homogeneous vector-valued (frictional contact) or scalar-valued (frictionless contact) multivariate polynomial. This expansion lacks the constant term since $\mathbf{q}=\mathbf{q}_0$ is an equilibrium configuration of the rigid system, hence the corresponding contact deformations are 0. The first order polynomial $R_1^{(i)}(\mathbf{x})$ can be expressed in the form $\mathbf{R}_1^{(i)}\mathbf{x}$ where $\mathbf{R}_1^{(i)}$ is the Jacobian matrix of the contact deformation function $\Delta\mathbf{r}^{(i)}(\mathbf{q})$ at $\mathbf{q}=\mathbf{q}_0$:

$$\Delta\mathbf{r}^{(i)} = \mathbf{R}_1^{(i)}(\mathbf{q}-\mathbf{q}_0) + \sum_{k=2}^{\infty} R_k^{(i)}(\mathbf{q}-\mathbf{q}_0) \qquad (75)$$

Notice that condition (ii) of **_Theorem 3.3.1_** is equivalent to the following property:

$$\text{rank} \begin{bmatrix} \mathbf{R}_k^{(1)} \\ \mathbf{R}_k^{(1)} \\ \vdots \\ \mathbf{R}_k^{(n)} \end{bmatrix} = m \qquad (76)$$

where n is the number of contacts and m is the degrees of freedom of the system.

If the contacts are stiff but compliant, the balancing contact forces induce $O(\varepsilon)$ contact deformations. Hence, $\mathbf{q}=\mathbf{q}_0$ ceases to be equilibrium. Instead, the equilibrium configuration $\mathbf{e}(\varepsilon)$ becomes

$$\mathbf{e}(\varepsilon) = \mathbf{q}_0 + \varepsilon\mathbf{e}_1 + O(\varepsilon^2) \qquad (77)$$

The rescaled variables $\Delta\tilde{\mathbf{r}}$ and $\tilde{U}$ have already been introduced in Sec. 3.3.2. Now we also define the rescaled generalized coordinates

$$\tilde{\mathbf{q}} = \varepsilon^{-1}(\mathbf{q}-\mathbf{q}_0) \qquad (78)$$

The rescaled generalized coordinates of the equilibrium configuration are $\tilde{\mathbf{e}}(\varepsilon) = \mathbf{e}_1 + O(\varepsilon)$.

Now, $\mathbf{q}$ and $\Delta\mathbf{r}^{(i)}$ in (75) are replaced by $\tilde{\mathbf{q}}$ and $\Delta\tilde{\mathbf{r}}^{(i)}$ and first- and higher order terms in ε are neglected:

$$\Delta\tilde{\mathbf{r}}^{(i)} = \mathbf{R}_1^{(i)}\tilde{\mathbf{q}} + O(\varepsilon) \qquad (79)$$

We can now express the elastic energy of contact $^{(i)}$ in terms of $\tilde{\mathbf{q}}$:

$$\begin{aligned} U^{(i)} &= \varepsilon\tilde{U}^{(i)}\left(\Delta\tilde{\mathbf{r}}^{(i)}\right) \\ &= \varepsilon\tilde{U}^{(i)}\left(\mathbf{R}_1^{(i)}\tilde{\mathbf{q}} + O(\varepsilon)\right) \end{aligned} \qquad (80)$$

Similarly, the potential energy of the external loads is expanded into Taylor series; $\mathbf{q}$ is replaced by $\tilde{\mathbf{q}}$; and higher-order terms in ε are discarded:

$$\begin{aligned} P^{(ext)} &= \sum_{k=0}^{\infty} P_k(\mathbf{q}-\mathbf{q}_0) \\ &= \sum_{k=0}^{\infty} \varepsilon^k P_k(\tilde{\mathbf{q}}) \\ &= p_0 + \varepsilon\mathbf{p}_1^T\tilde{\mathbf{q}} + O(\varepsilon^2) \end{aligned} \qquad (81)$$

For brevity, the zeroth-order polynomial term $P_0(\ldots)$ has been replaced by the scalar p_0 and $P_1(\mathbf{x})$ is expressed as $\mathbf{p}_1^T\mathbf{x}$ where $\mathbf{p}_1$ is the gradient of $P^{(ext)}(\mathbf{q})$ at $\mathbf{q}=\mathbf{q}_0$.

The total potential energy P of the system is the sum of $P^{(ext)}$ and $U^{(i)}$ for all i. We introduce the scaled potential energy function $\tilde{P} = \varepsilon^{-1}P$ to account for the fact that the energy stored in stiff elastic contacts is $O(\varepsilon)$. $\tilde{P}$ is expressed in terms of $\tilde{\mathbf{q}}$:

$$\tilde{P} = \varepsilon^{-1} P^{(ext)} + \varepsilon^{-1} \sum_{i=1}^{n} U^{(i)}$$

$$= \varepsilon^{-1} p_0 + \mathbf{p}_1^T \tilde{\mathbf{q}} + ... \qquad (82)$$

$$+ \sum_{i=1}^{n} \tilde{U}^{(i)} \left(\mathbf{R}_1^{(i)} \tilde{\mathbf{q}} + O(\varepsilon) \right) + O(\varepsilon)$$

We aim to study the local shape of the potential landscape $\tilde{P}$ around the equilibrium configuration $\tilde{\mathbf{q}} = \tilde{\mathbf{e}}$, where the argument of $U^{(i)}$ in (80) is close to $\mathbf{R}_1^{(i)} \tilde{\mathbf{e}}$. The Taylor expansion of the function $\tilde{U}^{(i)}$ at this point, up to second order is:

$$\tilde{U}^{(i)}(\mathbf{x}) = u_0^{(i)} + ...$$

$$\mathbf{u_1^{(i)T}} \left(\mathbf{x} - \mathbf{R}_1^{(i)} \tilde{\mathbf{e}} \right) + ...$$

$$\left(\mathbf{x} - \mathbf{R}_1^{(i)} \tilde{\mathbf{e}} \right)^T \mathbf{U}_2^{(i)} \left(\mathbf{x} - \mathbf{R}_1^{(i)} \tilde{\mathbf{e}} \right) + ... \quad (83)$$

$$O\left(\left\| \mathbf{x} - \mathbf{R}_1^{(i)} \tilde{\mathbf{e}} \right\|^3 \right)$$

where $u_0^{(i)} = \tilde{U}^{(i)}(\mathbf{R}_1^{(i)} \tilde{\mathbf{e}})$; $\mathbf{u_1}^{(i)}$ and $\mathbf{U}_2^{(i)}$ are the gradient and the Hessian of $\tilde{U}^{(i)}(\mathbf{x})$ at $\mathbf{x} = \mathbf{R}_1^{(i)} \tilde{\mathbf{e}}$. Combining (82) with (83) yields

$$\tilde{P} = \varepsilon^{-1} p_0 + \mathbf{p}_1^T \tilde{\mathbf{q}} + ...$$

$$\sum_{i=1}^{n} \left(u_0^{(i)} + \mathbf{u_1^T} \mathbf{R}_1^{(i)} (\tilde{\mathbf{q}} - \tilde{\mathbf{e}}) + \left(\mathbf{R}_1^{(i)} (\tilde{\mathbf{q}} - \tilde{\mathbf{e}}) \right)^T \mathbf{U}_2^{(i)} \left(\mathbf{R}_1^{(i)} (\tilde{\mathbf{q}} - \tilde{\mathbf{e}}) \right) \right) + ...$$

$$O\left(\left\| \tilde{\mathbf{q}} - \tilde{\mathbf{e}} \right\|^3 \right) + O(\varepsilon)$$

Ordering the right-hand side by powers of $(\tilde{\mathbf{q}} - \tilde{\mathbf{e}})$ and eliminating constant terms, which have no physical significance, lead to

$$\tilde{P} = \left(\mathbf{p}_1^T + \sum_{i=1}^{n} \mathbf{u_1^T} \mathbf{R}_1^{(i)} \right) (\tilde{\mathbf{q}} - \tilde{\mathbf{e}}) + ...$$

$$\sum_{i=1}^{n} (\tilde{\mathbf{q}} - \tilde{\mathbf{e}})^T \mathbf{R}_1^{(i)T} \mathbf{U}_2^{(i)} \mathbf{R}_1^{(i)} (\tilde{\mathbf{q}} - \tilde{\mathbf{e}}) + ... \qquad (84)$$

$$O\left(\left\| \tilde{\mathbf{q}} - \tilde{\mathbf{e}} \right\|^3 \right) + O(\varepsilon)$$

The linear term vanishes because $\tilde{\mathbf{q}} = \tilde{\mathbf{e}}$ corresponds to equilibrium. The n summed quadratic forms are nonnegative for every i because the Hessian matrix $\mathbf{U}_2^{(i)}$ is positive definite as pointed out in Sec. 3.3.3. Furthermore, condition (ii) of **Theorem 3.3.1** implies that for any $\tilde{\mathbf{q}} - \tilde{\mathbf{e}} \neq 0$ there is an i for which $\mathbf{R}_1^{(i)}(\tilde{\mathbf{q}} - \tilde{\mathbf{e}}) \neq 0$. The corresponding quadratic term in (84) is strictly positive. Hence, we conclude that the potential energy has a non-degenerate quadratic local minimum at $\tilde{\mathbf{q}} = \tilde{\mathbf{e}}$, which proves **Theorem 3.3.1**.

The local minimum (i.e. convexity) stems from the convexity of the $\tilde{U}^{(i)}$ functions. For deformable systems (finite ε), the local minimum can be reshaped by geometric nonlinearity (i.e. the nonlinear terms in (79)). However this factor is negligible in the quasi-rigid limit. Simple examples of the destabilizing effect of geometric nonlinearity include

- the 'coin-snap problem' [44]: a grasp on a rigid object may become unstable if the object is pressed too hard and the fingers are compliant
- buckling [83]: the straight configuration of a column built of stone blocks under a compressive force is unstable if the building blocks are not perfectly rigid, the column is slender and it is under strong compression (resulting in strong geometric nonlinearity).

This section is finished by the numerical analysis of a simple problem illustrating the stability of systems in the quasi-rigid limit. A model of a planar biped standing on a stair (Fig. 45.A) is investigated. The system consists of two legs connected by a hinge. The legs of the robot are allowed to cross the support surface. For simplicity, it is assumed that the hinge has unit weight and the weights of the legs are negligible. The only external forces acting at the robot are its weight and the support reactions. It is assumed that the contacts are elastic with a quadratic potential $\varepsilon^{-1} |\Delta \mathbf{r}^{(i)}|^2 / 2$ where $\Delta \mathbf{r}^{(i)}$
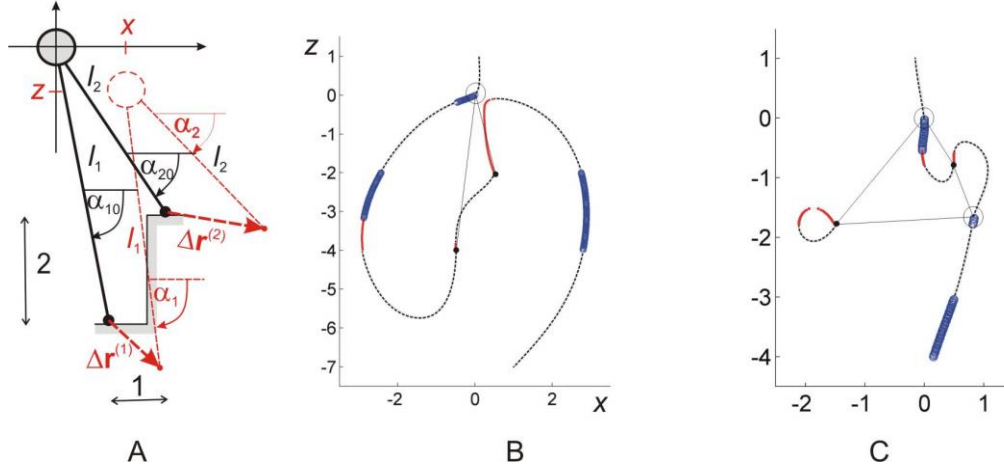
Fig. 45.A: Initial configuration (solid line) and a general configuration (dashed line) of a model of a planar biped standing on a stair. The weight of the body is 1, and the legs are weightless. B,C: *x* and *z* values corresponding to equilibria of the model system with l_1=4.03, l_2=2.06, α_{10}=-1.70, α_{20}=-1.33 (B) and with l_1=2.34, l_2=0.94, α_{10}=-2.27, α_{20}=-1.01 (C). The corresponding values of α_1, α_2 and ε are not shown. Circles and continuous curves represent stable and unstable equilibria, respectively. Dashed curves represent non-physical solutions (negative ε or tensile contact forces). The shapes of the robot in the quasi-rigid equilibrium configurations (the initial configuration in both panels and together with a second one in panel C) are shown in thin line.

$$\Delta n^{(1)} = -z + l_1(\sin \alpha_1 - \sin \alpha_{10})$$

$$\Delta t^{(1)} = x + l_1(\cos \alpha_1 - \cos \alpha_{10})$$

$$\Delta n^{(2)} = -z + l_2(\sin \alpha_2 - \sin \alpha_{20}) \quad (85)$$

$$\Delta t^{(2)} = x + l_2(\cos \alpha_2 - \cos \alpha_{20})$$

is the contact deformation vector of contact (*i*) introduced in Sec. 3.3.3. The initial configuration of the robot with zero contact deformations is plotted in solid line in Fig. 45.A. The shape of the robot is parametrized by the leg lengths l_1, l_2 and the angles α_{10}, α_{20} of the legs in the initial configuration. We also introduce a Cartesian coordinate system with its origin at the hinge of the robot in the initial configuration.

If ε is nonzero, the initial configuration corresponds to vanishing contact forces, since contact forces are induced by the penetration of the legs of the robot into the support surface. Other configurations of the moving robot (dashed line in Fig. 45.A) are represented by four generalized coordinates: *x*, *z* (position coordinates of the internal hinge) and α_1, α_2 (the angles of the two legs). The potential energy of the

system with the contacts in stick state is $z + \varepsilon^{-1}|\Delta \mathbf{r}^{(1)}|^2/2 + \varepsilon^{-1}|\Delta \mathbf{r}^{(2)}|^2/2$. The normal and tangential components of $\Delta \mathbf{r}^{(i)}$ can be expressed in terms of the parameters and the generalized coordinates as

We allow arbitrarily large tangential contact forces (infinitely large friction coefficient) but adhesive contact forces are not allowed. With a finite friction coefficient, a subset of our equilibrium solutions would be preserved.

Stationary points of the potential energy (corresponding to equilibrium) have been found numerically for various values of ε (details omitted). The stability of the equilibria has also been determined by numerical investigation of the Hessian of the potential energy. The results are depicted in Fig. 45.B,C for two different combinations of the parameters. The one shown in Fig. 45.C exhibits two quasi-rigid equilibrium configurations, one of which happens to be ambiguous. In accordance with our main result, the segments of the equilibrium paths adjacent to the quasi-rigid

equilibrium configurations are always stable.

3.3.5 Application: static indeterminacy, and optimal contact forces

The application of **Theorem 3.3.1** to a specific system requires knowledge of the contact forces because of condition (i) of the theorem. This is usually easy if the number of independent constraints equals the degrees of freedom of the system (statically determinate systems, as in the case of Fig. 38.B,D). For example, the object in Fig. 38.D consists of one rigid element, i.e. the DOF is 3. One freely rotating wheel and one blocked wheel provide 1+2=3 reaction forces, which are determined uniquely by 3 independent equilibrium equations. Finding contact forces is problematic if the number of constraints is higher than the DOF (static indeterminacy) [125] [139] as in the examples of Fig. 38.A,C. In this case, modeling the elastic deformations of the

objects (or the contacts) is necessary for the determination of the contact forces.

Robotic systems (grippers, vehicles or legged robots) often operate with (fully or partially) controlled contact forces. In this case, stabilizing a system reduces to the problem of optimizing contact forces in order to avoid contact slipping and contact separation. To illustrate this scenario, the example of a planar biped is revisited. This time, the contacts are quasi-rigid. The leg lengths (l_1, l_2) and an internal torque between the two rigid parts (T) are controlled by ideal actuators (Fig. 45.A). Our goal is to identify the region of the plane, in which the hinge can move around (by adjustment of the leg lengths) without losing static stability.

The contact normals are well-defined as contacts are vertex-edge type. Condition (iii) is also satisfied because gravity is conservative. To examine condition (ii), we express the Jacobians of the contact deformations with the aid of (85) as
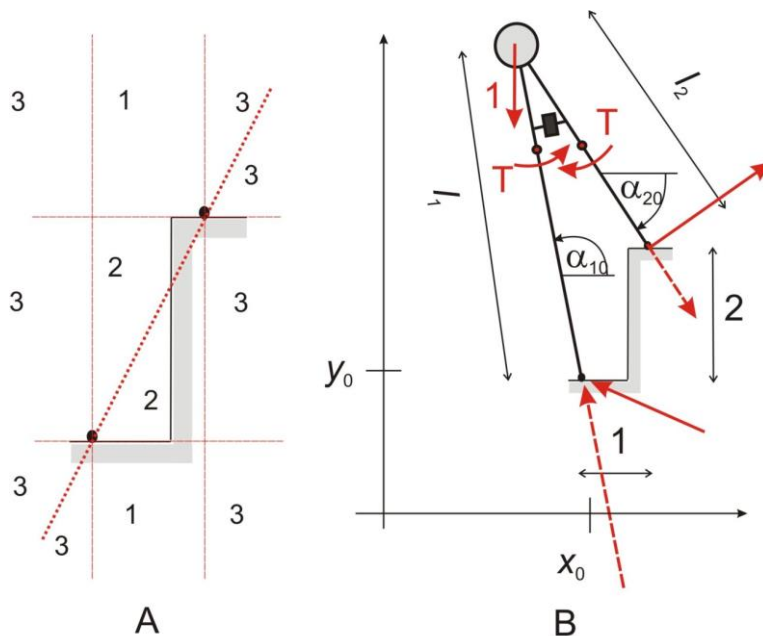

Fig. 46.A: the stability properties of the biped of Fig. 45 depend on the location of the center of mass relative to the support points. For the detailed description of labels 1, 2, 3, and 4, see text. B: Forces acting on the biped. For the specific configuration plotted in the figure, and T=0, the equilibrium equations dictate tensile support reaction at the right leg (dashed arrows). Hence the robot topples. However for appropriately chosen T and large enough friction coefficient, the toppling solution coexists with a static equilibrium. The corresponding support reactions are shown by solid arrows.

$$\mathbf{R}_1^{(1)} = \begin{bmatrix} 0 & -1 & 0 & l_1 \cos \alpha_1 \\ 1 & 0 & 0 & -l_1 \sin \alpha_1 \end{bmatrix}$$

$$\mathbf{R}_1^{(2)} = \begin{bmatrix} 0 & -1 & 0 & l_2 \cos \alpha_2 \\ 1 & 0 & 0 & -l_2 \sin \alpha_2 \end{bmatrix} \tag{86}$$

$\left[\mathbf{R}_1^{(1)T} \ \mathbf{R}_1^{(2)T} \right]^T$ is square matrix and its determinant is $l_1 l_2 \sin(\alpha_2 - \alpha_1)$. Eq. (76) is satisfied unless $\alpha_1 - \alpha_2$ is an integer multiple of π, i.e. unless the center of mass lies on the line through the two supports (dotted line in Fig. 46.A).To examine condition (i), the support reactions have to be determined using the equations of equilibrium of the system (details omitted). If $T{=}0$, the equations dictate the following support reactions: with sufficient friction, the robot is in equilibrium if the hinge is in a range marked by '1' or '4' in Fig. 46.B. Nevertheless the robot may also topple if the hinge is in range '4', hence such configurations are ambiguous equilibria. In ranges '2' or '3', the robot must topple as the equilibrium equations dictate tensile support reactions, which is impossible. By applying an appropriate torque in the hinge, these configurations can be turned into equilibria, provided that there is sufficient friction at the support point (Fig. 46.B). Assuming Coulomb friction, the minimum of the friction coefficient necessary to balance the object depends on the position of the hinge and the applied internal torque. For every configuration, there is an 'optimal' torque, minimizing the required friction coefficient. These torques and the corresponding thresholds of the friction coefficient are shown in Fig. 47. Specifically, the minimum of the friction coefficient is 0 in ranges '1' and '2'. However a friction coefficient above 0.5 is necessary to move the robot into ranges '3' and '4'. The maximum overhang of the center of mass is limited by the actual value of the friction coefficient.
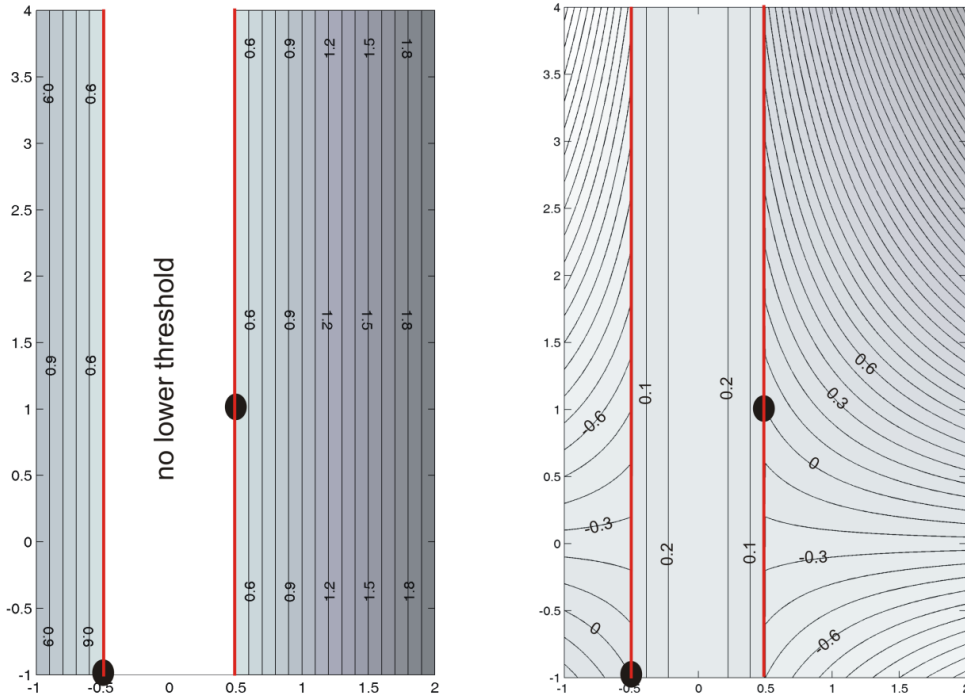

Fig. 47. Filled contour plot of the minimum of the friction coefficient (left) and the corresponding applied torque (right) for various positions of the center of mass. The support points are represented by black circles. Both functions are discontinuous at the vertical lines through the support points.

3.3.6 Conclusions

Using a general class of deformable contact models, it has been demonstrated that the frictional equilibria of a wide class of systems of rigid bodies are local minima of their potential energy. This result applies to regular as well as to ambiguous equilibria.

From the definition of static stability it is not immediately obvious how relevant it is in a dynamical systems perspective. Clearly, static stability is weaker than Lyapunov-stability, i.e. it allows divergence from the equilibrium in response to small impacts and initial displacements. With other words, dynamic vibrations in the environment are not allowed as perturbations. Nevertheless, many robotic systems operate in environments, which are practically vibration-free, this is why static stability has been successfully applied in the context of grasping, and it is useful in quasi-static locomotion. What it does guarantee is that the system remains stable in response to small variations of the external loads (see Appendix 5.6 for more details).

Rigid systems are infinitely sensitive to positioning errors, and because of this, the *Theorem 3.3.1* should be interpreted carefully. If one moves a system into an equilibrium configuration, it will not necessarily stay immobile. For example, the brick of Fig. 38.A may either stay, or it may immediately lose contact and fall off. The fate of the block depends on the initial microscopic state of the contacts (microscopic contact deformations), which is invisible to an external observer. Specifically, it does not stay immobile unless it is squeezed between the walls appropriately. At the same time, *Theorem 3.3.1* does predict that a system, which has been in the equilibrium state for some time, will stay there even if its external loads are slightly varied.

In addition to possible applications in robotics and manufacturing, the result of this work offer new insights on the mechanics of masonry structures. The safety of these structures is often analyzed with the aid of the safe theorem of plastic limit analysis [29],[82]. Nevertheless, since masonry structures are collections of discrete, quasi-rigid elements rather than plastic continua, this approach leads to controversial results [9] [45]. The main result of this section can be interpreted as a new safe theorem, which captures the discrete nature of masonry structures.

3.4 INFINITESIMAL MOTION AND THE LYAPUNOV STABILITY OF EQUILIBRIA

This section is concerned with the stability analysis of a rigid body with two point contacts in two dimensions. In particular we develop Lyapunov-stability conditions on a sloped terrain subject to arbitrary autonomous external forces.

3.4.1 Background and problem statement

Motion planning of legged robots is a complex, high level task, in which the identification of acceptable configurations in a given environment is a key component [85] [96] [78] [27]. The same issue occurs in many other tasks including other forms of robotic motion [115] [30], object manipulation [28], and robotic grasping

[119][136]. Some of these applications were already introduced in Sec. 3.3. A rigid body with two point contacts, is not only the simplest system exhibiting complex dynamic behavior induced by impacts, but also a simple mechanical model of a quasi-static planar bipedal robot. In this section, we focus on this model problem, and the object will often be referred to as a 'biped'.

We have seen in Sec. 3.1 that LS offers a high level of safety for the engineer without being very restrictive. Unfortunately, testing a configuration for LS is an open problem in contrast to most other criteria mentioned in Sec. 3.1. It is known that STRS is necessary for LS [128], and a sufficient frictional stability condition for biped planar robots based on a special impact model has been published by Or & Rimon [126]. Additionally, the author of this thesis and his coworkers have proposed a model-independent simple active control scheme to ensure LS [166]. The core of the last two results is a transition graph of contact modes in which every directed path leads to the node representing static equilibrium.

Our present goal is to make an additional step towards the understanding of LS of walking robots. Our main result is a new sufficient condition of LS by using an approach different from previous works: we introduce an energetic Lyapunov-type function U, which is bounded from below and minimized by configurations belonging to the equilibrium set of the object. We prove that U decreases in proportion to the distance travelled from the initial configuration. This function allows to restrict the set of configurations reachable by the perturbed object to an infinitesimal neighborhood of the initial point. By following this strategy, we completely avoid the difficulties of transition-graph based analysis in the case of Painlevé's paradox.

Similarly to previous authors, we linearize the kinematic equations around the initial
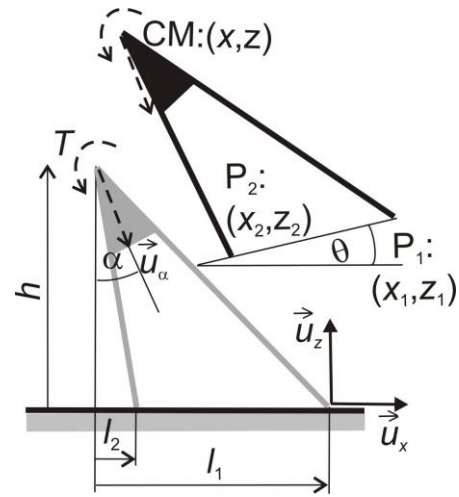

Fig. 48. Unperturbed (gray) and perturbed (black) configuration of the rigid body. The perturbation has been magnified to a macroscopic level for visibility. The external loads are plotted in dashed lines.

equilibrium such that the accelerations become constant in each contact mode. The simplified system is examined throughout Sec. 3.4. It can be proven using simple continuity arguments that te results are applicable to the original nonlinear system, nevertheless a formal proof is beyond the scope of this thesis.

While LS is clearly more restrictive than STRS, we are not aware of any example illustrating this difference. Therefore the main result is complemented by a simple example of an STRS equilibrium without LS in Sec. 3.4.4. To stress that stability against vibrations cannot be reached simply by the application of absorbers, our example is designed with perfectly plastic impacts. We also perform numerical simulations and a comparison of existing sufficient conditions of stability (Section 3.4.5).

3.4.2 Notation and preliminaries

This section establishes our basic notation and develops the linearized set of dynamical equations under general conditions. Without loss of generality, we consider a planar rigid object of unit mass and radius of inertia over a horizontal or sloped flat

terrain (Fig. 48). The locations of two point contacts relative to the center of mass are parametrized by the scalars h, l_1 and l_2. Our notation is somewhat different of the one used in Sec. 3.3. The model system considered here is also different because it is a single rigid body without an internal hinge. The coordinates of the center of mass (CM) are (x,z) in a coordinate system spanned by the unit vectors $\mathbf{u}_x$ (parallel to the terrain) and $\mathbf{u}_z$ (perpendicular to the terrain), with its origin at one of the point contacts. The rotation angle of the object relative to its initial configuration is denoted by θ. Initially, $x=-l_1$; $z=h$; $\theta=0$, which corresponds to resting on the ground. The object is subject to a constant unit force $\mathbf{u}_\alpha=[-\sin\alpha \quad \cos\alpha]^T$ (with ^{T} denoting transpose) and a torque T. The loads represent the resultant of an arbitrary system of external forces. For example, $\mathbf{u}_\alpha$ can represent gravitational effects when the object lies on a slope with angle α. The object has two frictional point contacts marked as P_1 and P_2. The initial coordinates of P_i ($i=1,2$) are $x_i=l_i\text{-}l_1$ and $z_i = 0$.

A Contact forces in static equilibrium

If the object rests in two-contact equilibrium, the normal components of the reaction forces $\mathbf{f}_i$ must be nonnegative. These can be determined from the equilibrium of moments about points P_i yielding the bounds

$$\left(l_2 \cos \alpha - h \sin \alpha + T\right)(l_2 - l_1)^{-1} \geq 0 \qquad (87)$$

$$\left(- l_2 \cos \alpha + h \sin \alpha - T\right)(l_2 - l_1)^{-1} \geq 0 \qquad (88)$$

The tangential forces are not uniquely determined by the equilibrium equations. Any pair of forces with

$$\mathbf{u}_x^T(\mathbf{f}_1 + \mathbf{f}_2) = - \sin \alpha \qquad (89)$$

ensures equilibrium.

B Kinematics of infinitesimal motion

After a dynamic perturbation, the object starts off, and the coordinates of the legs become

$$\mathbf{r}_i = \begin{bmatrix} x_i \\ z_i \end{bmatrix} = \begin{bmatrix} x + h \sin \theta + l_i \cos \theta \\ z - h \cos \theta + l_i \sin \theta \end{bmatrix}$$
$$\approx \begin{bmatrix} x + h \theta + l_i \\ z - h + l_i \theta \end{bmatrix} \qquad (90)$$

where the formula after the $\approx$ sign is a lowest order approximation valid for low velocities and configurations close to the unperturbed configuration. The velocity (v_i) and the acceleration (a_i) of P_i are

$$\mathbf{v}_i = \begin{bmatrix} \dot{x}_i \\ \dot{z}_i \end{bmatrix} \approx \begin{bmatrix} \dot{x} + h \dot{\theta} \\ \dot{z} + l_i \dot{\theta} \end{bmatrix} \qquad (91)$$

$$\mathbf{a}_i = \begin{bmatrix} \ddot{x}_i \\ \ddot{z}_i \end{bmatrix} \approx \begin{bmatrix} \ddot{x} + h \ddot{\theta} \\ \ddot{z} + l_i \ddot{\theta} \end{bmatrix} \qquad (92)$$

C Newtonian description of infinitesimal motion

It is assumed that forces and impulses at the contact point affect the motion of the objects according to rigid body theory. By using Newton or Lagrange equation, a local mass matrix $\mathbf{M}_{ij}$ can be associated with any ordered pair of contact points P_i, P_j (with possibly $i=j$). $\mathbf{M}_{ij}$ is defined by

$$\mathbf{p}_j = \mathbf{M}_{ij}\left(\mathbf{v}_i^+ - \mathbf{v}_i^-\right) \qquad (93)$$

where $\mathbf{p}_j$ is an impulse acting at P_j; $\mathbf{v}_i^-$ and $\mathbf{v}_i^+$ are pre- and postimpact velocities of P_i. This implies

$$\mathbf{M}_{ij} \approx \begin{bmatrix} 1 + h^2 & hl_j \\ hl_i & 1 + l_i l_j \end{bmatrix}^{-1} =$$
$$= \left(1 + h^2 + l_i l_j\right)^{-1} \begin{bmatrix} 1 + l_i l_j & -hl_j \\ -hl_i & 1 + h^2 \end{bmatrix} \quad (94)$$

This matrix can be used to determine the acceleration of point P_i in the presence of external forces and torques plus contact forces:

$$\mathbf{a}_i \approx \mathbf{u}_\alpha + T\left(l_i \mathbf{u}_z + h \mathbf{u}_x\right) + \sum_{j=1}^{2} \mathbf{M}_{ij}^{-1} \mathbf{f}_j \quad (95)$$

The accelerations $\mathbf{a}_i$ and the forces $\mathbf{f}_i$ can be determined by testing each contact mode in three steps as explained in Sec. 3.1.3. For example, if both contacts are in separated state (FF mode), then $\mathbf{f}_1 = \mathbf{f}_2 = 0$ and

$$\mathbf{a}_i^{(FF)} \approx \begin{bmatrix} \sin \alpha + Th \\ -\cos \alpha + Tl_i \end{bmatrix} \quad (96)$$

D Modeling impacts

Throughout this work we use the 2-parameter planar impact model of Chatterjee & Ruina [37]. This model provides a closed form reset map for the contact point velocity in the case of a single point impact at a point P_i. The model is briefly summarized below. For details, the reader should consult the original work [37].

The kinematic coefficient of normal restitution e sets the post-impact normal velocity of the contact point by

$$\dot{z}_i^+ = -e\dot{z}_i^- \quad (97)$$

where the indices $^+$ and $^-$ again refer to pre- and postimpact states.

The second parameter e_t determines to what extent the tangential velocity of the contact point is reversed.

The model predicts a 'sticking impact' with impulse

$$\mathbf{p}_{st} = (1 + e)\mathbf{p}_I + (1 + e_t)(\mathbf{p}_{II} - \mathbf{p}_I) \quad (98)$$

whenever $\mathbf{p}_{st}$ obeys Coulomb's law. In the formula, $\mathbf{p}_I$ is the impulse associated with a frictionless, perfectly plastic collision, ($\mathbf{p}_I^T \mathbf{u}_x = 0$ and $\mathbf{v}_i^{+T} \mathbf{u}_z = 0$) and $\mathbf{p}_{II}$ corresponds to a perfectly sticking, plastic impact ($\mathbf{v}_i^{+T} = 0$). These properties imply

$$\mathbf{p}_I = \frac{-\mathbf{v}_i^{-T} \mathbf{u}_z}{\mathbf{u}_z^T \mathbf{M}_{ii}^{-1} \mathbf{u}_z} \mathbf{u}_z \quad (99)$$

$$\mathbf{p}_{II} = -\mathbf{M}_{ii} \mathbf{v}_i^- \quad (100)$$

If $\mathbf{p}_{st}$ is inconsistent with Coulomb's law, a 'sliding impact' $\mathbf{p}_{sl}$ occurs. This is characterized by eq. (97) and by

$$\mathbf{u}_x^T \mathbf{p}_{sl} = \varepsilon \mu_i \mathbf{u}_z^T \mathbf{p}_{sl} \quad (101)$$

with $\varepsilon = \text{sign}\,(\mathbf{u}_x^T \mathbf{p}_{st})$. These two properties imply

$$\mathbf{p}_{sl} = \frac{-(1 + e)\mathbf{v}_i^{-T} \mathbf{u}_z}{\mathbf{u}_z^T \mathbf{M}_{ii}^{-1} \begin{bmatrix} \varepsilon \mu_i \\ 1 \end{bmatrix}} \begin{bmatrix} \varepsilon \mu_i \\ 1 \end{bmatrix} \quad (102)$$

E Energetic description of infinitesimal motion

At certain points, we consider the kinetic (E_k) and the potential (E_p) energy of the object. The latter is calculated as

$$E_p = (z - h)\cos\alpha$$
$$- (x + l_1)\sin\alpha - T\theta \quad (103)$$

The definition of Lyapunov stability in Sec. 3.1.8 makes use of 'an arbitrary vector norm'. This means that the particular choice of norm does not make any difference. In this section, we will use the state vector $\mathbf{q} = \begin{bmatrix} x_1 & z_1 & z_2 & \dot{x}_1 & \dot{z}_1 & \dot{z}_2 \end{bmatrix}^T$ such that the initial equilibrium corresponds to $\mathbf{q}_0=0$. Furthermore, we use the pseudo-norm:

$$|\mathbf{q}| = \max \left[|x_1|, |z_1|, |z_2|, \dot{x}_1^2, \dot{z}_1^2, \dot{z}_2^2 \right] \quad (104)$$

3.4.3 A sufficient stability condition

Sliding friction and impacts absorb the kinetic energy of an object in motion; nevertheless it also gains kinetic energy via the work done by the external force and torque, e.g., by the action of gravity while the object operates on a slope. Now we prove a sufficient conditions under which *the average rate of absorption exceeds energy gain* (while kinetic energy is allowed to increase temporarily).

First, notice that STRS always implies LS if $\alpha=0$ [135] because energy gain by downhill motion becomes impossible. Thus, without loss of generality, we may assume $0<\alpha<\pi/2$.

Our stability condition is

Theorem 3.4.1*: A STRS frictional equilibrium of a planar biped is LS if*

$$-\ddot{z}_i^{(FF)} = \cos \alpha - Tl_i > 0 \quad (105)$$

furthermore one of the following two sets of inequalities is satisfied:

$$\ddot{x}_1^{(FF)} = \cos \alpha + Th \geq 0 \quad (106)$$

$$\sin \alpha < (\cos \alpha - Tl_i) \cdot$$

$$\dots \cdot \frac{(1 - \nu^2)(\sqrt{(1+h^2)(1+l_i^2)} + hl_i)}{2(1+h^2+l_i^2)} \quad (107)$$

$$\sin \alpha \left(1 + l_i^2 - \mu_i hl_i\right) < (\cos \alpha - Tl_i)\frac{(1+e)\mu_i}{2} \quad (108)$$

$$\ddot{x}_1^{(FF)} \leq 0 \quad (109)$$

$$\sin \alpha < (\cos \alpha - Tl_i) \cdot$$

$$\dots \cdot \frac{(\nu^{-2} - 1)(\sqrt{(1+h^2)(1+l_i^2)} - hl_i)}{2(1+h^2+l_i^2)} \quad (110)$$

$$\sin \alpha \left((1 + l_i^2 - \mu_i hl_i)\right) < (\cos \alpha - Tl_i)\mu_i \quad (111)$$

both for i=1 and for i=2 with $\nu = \max(e, |e_T|)$

Before presenting the formal proof of ***Theorem 3.4.1***, we review its main ideas and state some lemmas.

The set of states reachable for the object is bounded by the non-penetration constraints

$$z_i \geq 0 \quad i = 1,2 \quad (112)$$

and by a trivial upper bound $E_p(t) \leq E_p(0) + E_k(0)$ of the object's potential energy. Here, $t=0$ is the time of the perturbation and $E_k(0)$ is the biped's initial kinetic energy after the perturbation at $t=0$. The bound (111) can easily be reformulated as $E_p(t) \leq \text{constant} \cdot |\mathbf{q}(0)|$

$$E_p(t) \leq \text{constant} \cdot |\mathbf{q}(0)| \quad (113)$$

due to the choice of norm (104). The (locally) linear constraints (112) and (113) correspond to three half-spaces, with an *unbounded intersection* in the three dimensional configuration space. For example, they allow unbounded downhill motion. Our basic tool of proving Lyapunov stability is to develop an additional inequality constraint such that the four constraints together have a *bounded*

intersection. We will use the Lyapunov-like function

$$U(t) = E_p(t) + E_k(t) + x_1(t)\sin\alpha \qquad (114)$$

which can be expressed in terms of E_k, x_1 and z_i using (90), (103), (114). U is constructed in such a way that the x_1 dependent terms cancel. Specifically, we obtain

$$U(t) = \frac{l_2\cos\alpha - h\sin\alpha + T}{l_2 - l_1}z_1(t) +$$
$$\ldots + \frac{-l_1\cos\alpha + h\sin\alpha - T}{l_2 - l_1}z_2(t) + \qquad (115)$$
$$\ldots + E_k(t)$$

All components of the right-hand side are nonnegative by (87), (88) and by (112). Thus, U is non-negative:

$$U(t) \geq 0 \qquad (116)$$

with equality if and only if the object is in two-contact equilibrium ($E_k{=}z_i{=}0$) anywhere on the slope.

In addition to its non-negativity, we will also prove that U exhibits a decreasing trend if the object is in motion, which will eventually lead us to the missing constraint in the form of an upper bound of $x_1(t)$. The exact meaning of the 'decreasing trend' of U depends on the sign of $\ddot{x}_1^{(FF)}$ (see (96)), which explains the presence of the two sets of inequalities (106)-(111) in the statement of **Theorem 3.4.1**. These two cases will be addressed by two slightly different lemmas below.

Lemma 3.4.2 *if (106) is true, then the conditions of* **Theorem 3.4.1** *imply the existence of a positive constant c such that*

$$\forall t_{fin} \in \tau :$$
$$\max\begin{Bmatrix} c(x_1(t_{fin}) - x_1(0)) \\ 0 \end{Bmatrix} \leq U(0) - U(t_{fin}^+) \quad (117)$$

where τ is the set of times after the initial perturbation when at least one point of the object undergoes an impact or it has sustained contact with the ground.

The $^+$ superscript in **Lemma 3.4.2** mean that we consider post-impact state at time t_{fin} if the velocity of the object is discontinuous due to an impact. In contrast, the next lemma includes $^-$ superscripts corresponding to pre-impact states

Lemma 3.4.3 *if (109) is true, the conditions of* **Theorem 3.4.1** *imply the existence of a positive constant c such that* $\forall t_{init}, t_{fin} \in \tau, t_{fin} > t_{init} \geq 0$:

$$\max\begin{Bmatrix} c(x_1(t_{fin}^-) - x_1(t_{init}^-)) \\ 0 \end{Bmatrix} \leq U(t_{init}^-) - U(t_{fin}^-)$$

$$(118)$$

The lemma will also be used with $t_{init}{=}0$. In this special situation, 0^+ and 0^- refer to pre- and post-impact states if the initial perturbation triggers an immediate impact. Nevertheless, both symbols refer to states after the perturbation.

Proof of **Lemma 3.4.2**: τ has continuous (corresponding to rolling or sliding motion), and discrete countable (bouncing motion) subsets. Accordingly, the trajectory of the object between the initial state immediately after the perturbation and t_{fin} can be divided to elementary pieces, all belonging to one of 3 types. We demonstrate that an analogue of *(117)* is true for each type of piece as explained below:

1. if t_k is an isolated elements of τ, and τ has no elements in the open interval (t_{k-1}, t_k) furthermore $x_i(t_k){>}x_i(t_{k-1})$ (free flight to the right followed by an impact) then (105)-(108) imply

$$c(x_1(t_k) - x_1(t_{k-1})) \leq$$
$$\ldots U(t_{k-1}^+) - U(t_k^+) \qquad (119)$$

The detailed proof is divided into three subcases dealing with sticking, right-sliding and left-sliding impacts (Appendix 5.7.1.A-C). In the proof, we exploit that the growth of U during an episode of free flight is proportional to $x_1(t_k)-x_1(t_{k-1})$. Nevertheless free flight with a big jump in $x_1(t)$ is necessarily followed by an impact with high contact point velocities ($\dot{x}_i, |\dot{z}_i|$) and high energy absorption ensuring negative net change of U.

2. Along trajectories with continuous contact and $\dot{x}_1 > 0$ (sliding to the right on one or 2 legs), (105), (106), (108) imply

$$\frac{dU}{dx_1} \leq -c \qquad (120)$$

see Appendix 5.7.1.D-E for proofs in the respective cases of sliding at one and at two points. The main idea of the proof is that the the growth rate of the $x_1(t)\sin\alpha$ term in U and the decay rate of E_p+E_k are both proportional to the sliding velocity of the object with negative net balance.

3. U is non-increasing during impacts, during rolling motion, during being in static equilibrium and during sliding motion to the left ($\dot{x}_1 \leq 0$). Furthermore, the net change of U during free flight to the left with $x_1(t_k) \leq x_1(t_{k-1})$ is also negative, i.e. $U(t_{k-1}^+) - U(t_k^+) \leq 0$. All these properties follow from the fact that x_1 and the total energy E_p+E_k are both non-increasing during these episodes of motion.

The three results explained above and proven in the appendices complete the proof of *Lemma 3.4.2*.

The proof of *Lemma 3.4.3* is very similar to that of *Lemma 3.4.2*. There are only a few minor differences, which are highlighted in Appendix 5.7.2. These are responsible for the difference between the sets of conditions (106)-(108) and (109)-(111).

The previous two lemmas provide us with enough information about almost all parts of the motion except for some missing bounds on contact-free motion:

Lemma 3.4.4 if the object undergoes contact-free motion between times t^* and t^{**} then there exists a constant C such that

$$U(t^{**-}) \leq CU(t^{*+}) \qquad (121)$$

$$x_1(t^{**}) - x_1(t^*) \leq CU(t^{*+}) \qquad (122)$$

The proof is presented in [174], Lemma 1. It is not repeated here.

Now we are ready for the

Proof of Theorem 3.4.1: If $\ddot{x}_1^{(FF)} \geq 0$ then (116) and *Lemma 3.4.2* together yield

$$x_1(t_{fin}) \leq x_1(0) + c^{-1}U(0^+) \qquad (123)$$

for all $t_{fin} \in \tau$. In the case of $\ddot{x}_1^{(FF)} < 0$, (116) and *Lemma 3.4.3* imply

$$x_1(t_{fin}) \leq x_1(t_{init}) + c^{-1}U(t_{init}^-) \qquad (124)$$

where $t_{init}, t_{fin} \in \tau$. If the set τ includes 0 (i.e. motion starts with an impact or sustained contact), then we may choose $t_{init}=0$, by which the bound (124) becomes essentially identical to (123). In the opposite case (i.e. if the motion starts with free flight), τ has a smallest positive element τ_{min} and we assign this value to t_{init} in (124). Furthermore, *Lemma 3.4.4* implies the bounds

$$U(\tau_{min}^-) \leq CU(0^+) \qquad (125)$$

$$x_1(\tau_{min}) - x_1(0) \leq CU(0^+) \qquad (126)$$

Altogether, (124)-(126) imply

$$x_1(t_{fin}) \le x_1(0) + CU(0^+) + c^{-1}CU(0^+) \quad (127)$$

So far we have established the upper bound (123) or (127) for x_1 whenever there is an active contact ($t_{fin} \in \tau$). Both bounds can be written in the general form

$$x_1(t_{fin}) \le \text{constant} \cdot |\mathbf{q}(0)| \quad (128)$$

This bound can be extended to episodes of contact-free motion, i.e. for $t \notin \tau$, by combining (128) with (122) of *Lemma 3.4.4*:

$$
\begin{aligned}
x_1(t) &\le x_1(t_{fin}) + CU(t_{fin}^+) \\
&\le \text{constant} \cdot |\mathbf{q}(0)| + CU(0^+) \\
&\underset{}{\le} \text{constant} \cdot |\mathbf{q}(0)| \\
&\overset{def}{=} x_{1,max}
\end{aligned}
\quad (129)
$$

Now we have four bounds represented by the inequalities (112), (113), and (129). As we prove in Appendix 5.7.3, the inequalities determine a bounded region in configuration space as long as the equilibrium conditions (87), (88) hold. If the norm of the initial perturbation was 0, then the bounds were not satisfied but by an isolated point in state space (namely $\mathbf{q}=0$). If the original perturbation is not zero but infinitesimally small, then the size of this region is linearly proportional to $|\mathbf{q}|$, implying LS.

If impacts are plastic ($e=0$ in the impact model) and (105) holds for $i=1$ and 2, then the contactless free accelerations of the legs point towards the ground, and thus impacts cannot be followed by free flight. Hence the set τ does not have isolated elements. Consequently, the corresponding conditions can be omitted and only the condition ensuring decreasing trend of U during sustained contact is needed instead. This leads to the stronger statement

Theorem 3.4.5: *a STRS frictional equilibrium of a planar biped with plastic impacts (e=0) is LS if (105) and (111) hold for i=1 and 2.*

3.4.4 An example of instability

The goal of the upcoming section is to illustrate the difference between STRS and LS through an example. We consider perfectly plastic impacts (the restitution parameters of the impact model are $e=e_t=0$) and $T=0$ (an object resting on a slope in a gravitational environment). We assume that $\mu_2 \gg 1$ (though this unrealistic assumption is not necessary ingredient) while μ_1 will be varied.

Let $0<l_1<h\tan\alpha<l_2$. This assumption implies positivity of the normal contact forces (87), (88) and there exist consistent tangential forces for any value of μ_1 by (89). Hence this configuration is a frictional equilibrium for any μ_1. According to *Theorem 3.4.5*, the object possesses LS
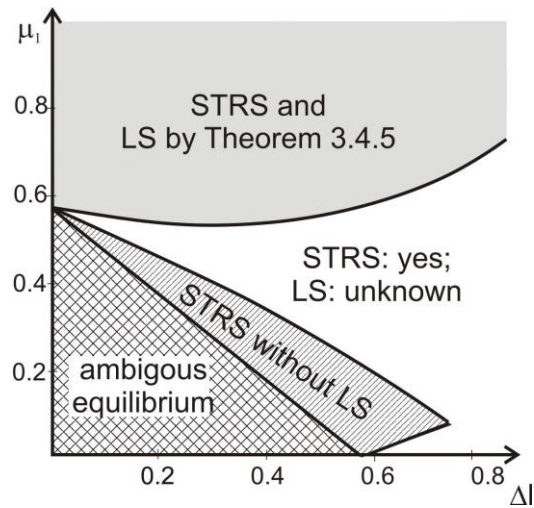

Fig. 49. Stability of the object with $T=0$, $\alpha=20°$, $h=1$, $\mu_2 \gg 1$, and plastic impacts ($e=e_t=0$). The leg positions are $l_i=h\tan\alpha+(-1)^i\Delta l$; Δl and μ_1 are varied. The label 'STRS without LS' refers to parameter values at which the divergent motion described in Section 3.4.4 occurs. The exact boundary of this region has been determined numerically.

above a threshold value of μ_1. This threshold is shown in Fig. 49 for $\alpha=20°$. Nevertheless the behavior of the object changes at lower μ_1: the equilibrium is ambiguous if $\mu_1<l_1/h$ (Fig. 49), which means that the object can undergo accelerating motion starting from the equilibrium configuration. Specifically, sliding to the right on P_1 with P_2 lifting off the ground is consistent solution as shown by the following three considerations:

• *Positive contact force at P_1*: if $\mathbf{f}_2 = 0$ and $\mathbf{f}_1 = f(-\mu_1\mathbf{u}_x + \mathbf{u}_z)$, where f is an unknown scalar, then f can be determined from $\ddot{z}_i = 0$ using (95):

$$\ddot{z}_i = -\cos\alpha + Tl_i + \mathbf{u}_z^T\mathbf{M}_{ii}^{-1}f\begin{bmatrix} -\mu_i \\ 1 \end{bmatrix} = 0 \qquad (130)$$

yielding

$$f = \frac{\cos\alpha}{1 + l_1^2 - \mu_1 h l_1} \qquad (131)$$

f is positive if $\mu_1<l_1/h$.

• *Increasing sliding velocity at P_1*: According to the previous point, $f<\cos\alpha$, hence $\mu_1 f<l_1/h\cos\alpha<\sin\alpha$, which implies acceleration of the centroid to the right: $\ddot{x}>0$. The contact force causes counterclockwise torque about the centroid if $\mu_1 \leq l_1/h$, i.e. $\ddot{\theta} > 0$.

These observations imply $\ddot{x}_1 > 0$ by (92).

• *Increasing separation at P_2*: we have $\ddot{\theta} > 0$ as pointed out above. According to (92), $\ddot{z}_2 - \ddot{z}_1 = (l_2 - l_1)\ddot{\theta}$, hence $\ddot{z}_1 = 0$ implies $\ddot{z}_2 > 0$

If μ_1 is slightly greater than l_1/h, $\ddot{z}_2$ changes sign, hence the sliding-separated motion starting from the equilibrium configuration becomes inconsistent. Other non-static modes are not consistent either (calculation omitted), i.e. the equilibrium becomes unambiguous. A velocity-perturbation of the equilibrium at $t=0$ with $v_2(0^+) = \delta u_z$ (where δ is a positive constant small enough to allow the application of linearized dynamical equations) and $v_1(0^+) = 0$ initiates microscopic motion with the following subsequent phases (see Fig. 50):

1. *Uniformly accelerating sliding motion of P_1 to the right* until the contact at P_2 hits the ground after a long time t_1 due to $\ddot{z}_2$ being slightly below 0. At this time, $\mathbf{v}_2(t_1^-) = \Delta\mathbf{u}_x - \delta\mathbf{u}_z$ with $\Delta\gg\delta$ (⁻ standing for left limit as usually).

2. *A plastic impact at P_2* with the above found pre-impact velocity. This impact is sticking if $\mu_2\gg1$ because the impulse corresponding to a sticking impact (determined from (98)) has a positive normal component and a finite
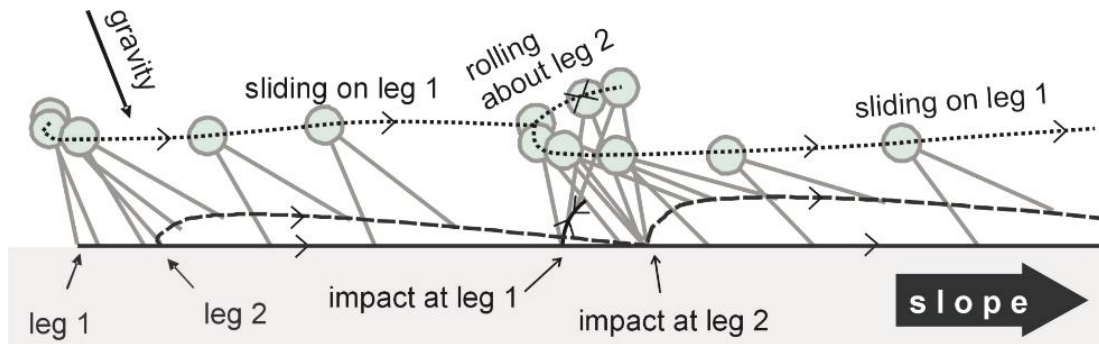

Fig. 50. Divergent motion of an object with STRS in response to an infinitesimal perturbation. Note that the slope terrain is rotated by angle α for simplicity. Continuous, dashed and dotted lines denote the respective trajectories of P_1, P_2, and the centroid.

tangential to normal ratio (calculation omitted) even for an almost tangential pre-impact velocity. Thus, $\mathbf{v}_2(t_1^+) = 0$. On the other hand, the tangential to normal ratio of the impulse exceeds l_2/h if $\Delta/\delta > l_2/h$, i.e. the impulse has a clockwise torque about the centroid thereby increasing the magnitude of the (negative) angular velocity $\dot{\theta}$. According to (91), $\dot{z}_2 - \dot{z}_1 = (l_2 - l_1)\dot{\theta}$, implying $|\dot{z}_2(t_1^+) - \dot{z}_1(t_1^+)| > |\dot{z}_2(t_1^-) - \dot{z}_1(t_1^-)|$. Since $\dot{z}_1(t_1^-) = \dot{z}_2(t_1^+) = 0$ and $\dot{z}_2(t_1^-) = \delta$, we conclude that $\dot{z}_1(t_1^+) > \delta$.

3. *Rolling motion about P_2:* it can be shown that the contact at P_2 does not slide, and $\ddot{z}_1 < 0$. This phase lasts until the contact at P_1 recovers at time t_2. At this time, $\dot{z}_1(t_2^-) = -\dot{z}_1(t_1^+) < -\delta$.

4. *A plastic impact at P_1 with zero tangential pre-impact velocity:* $\dot{x}_1(t_2^-) = 0$. According to (98), this impact is again sticking with a tangential to normal impulse ratio below l_1/h. It can be shown similarly to point 2. that $\dot{z}_2(t_2^+) > -\dot{z}_1(t_2^-) > \delta$.

After the second impact, the same cycle is repeated with an initial velocity $\dot{z}_2 > \delta$. Thus, the object undergoes exponentially growing cycles and diverges unboundedly from the unperturbed configuration. Hence the original configuration is not LS. The exact range of μ_1 leading to this kind of instability has been determined numerically (Fig. 49).

3.4.5 Comparison with previous results and simulations

The sufficient stability condition presented here is fundamentally different from the one in [126]. Our result tends to predict stability when the distance of the legs $(l_2 - l_1)$ is
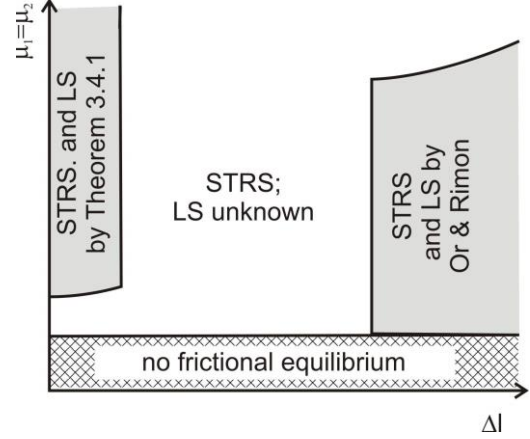

Fig. 51. Stability regions predicted by *Theorem 3.4.1* **(with e=0.1 and e_t=0) and by [126] for an object with h=1 on a slope of angle α=20° subject to gravity (T = 0).**

relatively small and the friction coefficients are high; whereas the other condition suggests the opposite. This is illustrated by an example in Fig. 51, where the positions of contact points are $l_i = h\tan\alpha + (-1)^i \Delta l$. The distance Δl and the friction coefficients at the legs ($\mu_1 = \mu_2$) are varied. Other parameter values are given in the figure caption. With these data, the object is in STRS frictional equilibrium if $\mu_i > \tan\alpha$. The Lyapunov stability regions associated with the sufficient conditions appear in opposite corners of the parameter plane. This difference might partly be attributed to the different impact models: [126] assumes frictionless impacts equivalent of the case $e_t = -1$ of the Chatterjee-Ruina model whereas we used $e_t = 0$. Our choice is more realistic, moreover ***Theorem 3.4.1*** does not predict stability at all if $e_t = -1$. Nevertheless we think that the primary reason for the different predictions is that both sufficient conditions are far from being sharp. The conservativeness of our result comes from the main idea of the proof: the motion of the object is divided to small episodes and it is required that the net change of U is negative during *every single episode*. A numerical simulation of this kind of behavior is shown in Fig. 52.A. Notice that U decreases

continuously during sliding motion (top panel of figure); it increases continuously during episodes of free flight, but this is always followed by an instantaneous jump to a lower level due to an impact. As a result, U decays rapidly to its minimum value and the object stops in agreement with our theoretical results.

We also performed numerical simulations with parameter values for which the sufficient conditions do not predict stability. Interestingly, divergent motion occurred in very few cases, which seems to confirm the conservativeness of the stability conditions. Fig. 52.B shows one of the exceptions: a steep slope (α=45°) combined with high coefficient of restitution (e=0.7) and an appropriate initial perturbation leads to

divergent 'reverse chattering' motion, in which the two legs hit the ground in alternating order. Nevertheless, the same setting with a slightly different initial perturbation initiates different motion and recovering equilibrium (Fig. 52.C). This last simulation shows the characteristics of a typical run: while the net change of U is positive during some episodes of the motion (one of these is highlighted in the figure by a dashed circle), U decreases on average, and converges to its minimum value corresponding to a new equilibrium.

3.4.6 Summary and ongoing work

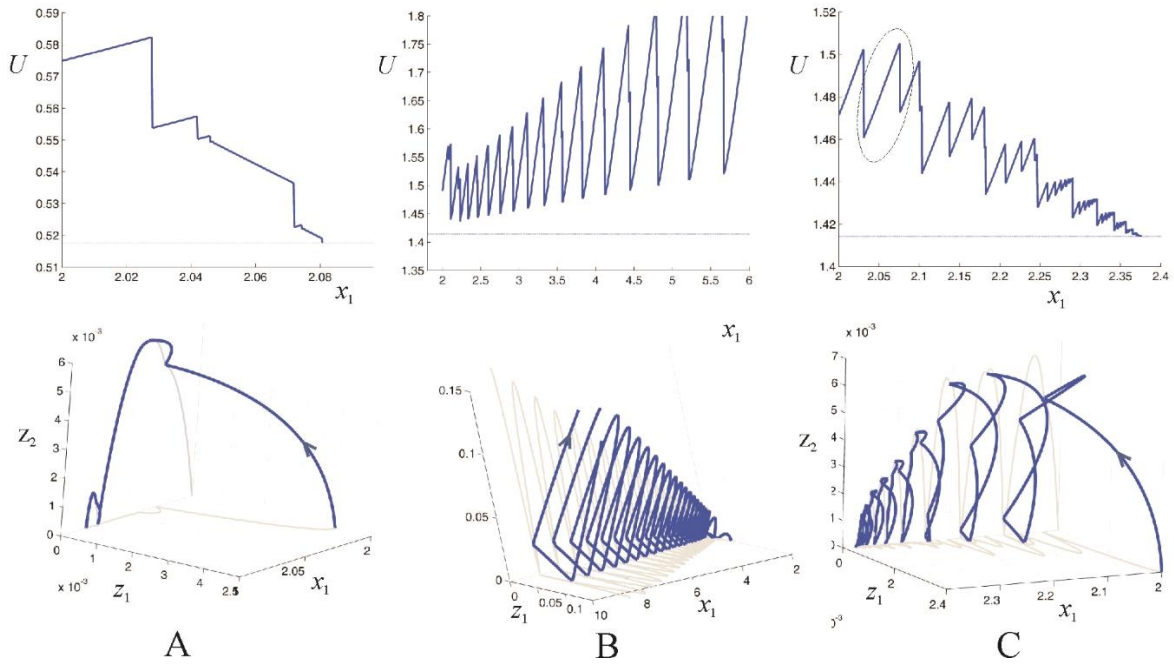We developed a sufficient condition of LS for planar objects with two contacts over a

Fig. 52. Diagram of U vs. x_1 (top) and trajectories in z_1-z_2-x_1 space (bottom) obtained by numerical simulations of the linearized equations of a biped, starting from a perturbed equilibrium. A: mild slope and low coefficient of restitution (α=15°; e=0.3, e_t=0.1; μ_1=μ_2=1.2; h=0.6; l_1=–l_2=1.2; the initial perturbation is z_1=0.04; z_2=0; $\dot{x}_1 = 0.18 \quad \dot{z}_1 = 0$; $\dot{z}_2 = 0.06$). In this case, Thm. 3.4.1 predicts stability; accordingly, U decays rapidly to its minimum value (thin line in top panel) corresponding to two-contact equilibrium. B: steeper slope and high coefficient of restitution (α=45°, e=0.7, all other data are the same as in A). Thm. 3.4.1 does not predict stability; indeed the object undergoes divergent downhill motion with U growing. C: the same as B, but with different perturbation (z_1=0.024, other data as in B). The object stops in this case. In the top panel, an episode of free flight (U increasing gradually) and a subsequent impact (sudden drop of U) are highlighted by an ellipse. The net change of U during this episode is positive, which explains why Thm. 3.4.1 does not predict stability in this situation.

flat or sloped terrain. Comparison to previous sufficient stability conditions as well as our numerical simulations suggest that the available results are far from sharp, especially if impacts are not perfectly plastic. Indeed, finding divergent motion in a numerical simulation by trial and error is rarely successful. At the same time, our analytical example of instability and experimental reproduction of divergent motion (unpublished result) indicate that the lack of stability against dynamic perturbation is a definitely existing phenomenon.

The problem discussed here naturally connects to the stability analysis of various gaits of dynamic locomotion, represented by a periodic orbit in state space rather than a fixed point as in our case [180] [67] [88]. However our problem is more involved as it is not tractable by the standard methods of linear stability analysis. On the other hand, the results of the present work are just initial steps towards the general understanding of Lyapunov stability in rigid multibody systems. Among others, the LS analysis of three dimensional rigid bodies with frictional supports appears to be completely unexplored despite its practical importance. The existing results also suffer from being model-dependent. Rigid body impact models are simple phenomenological descriptions of a complex mechanical process involving elastic vibrations, plastification, and viscous damping, so it is not surprising that their quantitative predictive power is very limited [152]. In the context of the current problem, the lack of a perfect impact model prevents one from finding exact stability boundaries. Nevertheless we believe that model-dependent theoretical investigations are useful for the understanding of the qualitative stability properties of the systems in question. At the same time, active control schemes [166] might yield more reliable stabilization in situations where high accuracy is needed.

Recently, a much sharper stability condition has been developed for systems with inelastic impacts, by the author of this thesis and by his co-author Yizhar Or [174]. Those results are not presented in this thesis.

A more general computational approach to proving LS has been published very recently by Posa & Tedrake [132]. Those authors introduced an efficient computational algorithm that utilizes convex optimization for constructing sum-of-squares Lyapunov functions for planar mechanical systems with unilateral frictional contacts under inelastic impacts. This algorithm enables determination of Lyapunov stability for equilibrium states, and even computation of conservative bounds on regions of attraction. The efficiency of this method in the case of the planar biped and related problems will be tested in the future.

CHAPTER 4:   SUMMARY

4.1 CLOSING REMARKS

IN this thesis, I presented a part of the research, which I conducted during the past decade. I discussed in detail those segments of my work, which focus on the abundance and various properties of static equilibria. Some of these problems were geometric by nature whereas others were inherently linked to the dynamics of mechanical systems.

Due to length limitations, other aspects of the my research efforts have been skipped. These include the stabilization of equilibria by feedback control [166]; the analysis of non-static contact modes and a deeper investigation of Painlevé's paradox in contact mechanics [36] [177], which are all tightly linked to the content of Chapter 3. I also skipped newer and stronger theoretical results about the Lyapunov stability of a planar rigid body, as well as experimental investigations, which were unpublished when the structure of this thesis was worked out [174]. Finally, a large body of applied research in geomorphology emanating from the development of equilibrium classes was only briefly mentioned, see for example [178].

I believe that the mechanics of rigid bodies and multibody systems is a very rich topics, and the narrowed scope that I have chosen, includes enough intriguing questions to be investigated. If nothing else, the vast number of questions, which are left open by the dissertatioon, demonstrates how much work there is to be done. We have seen that there are many seemingly simple unsolved theoretical questions about the number of equilibria, such as whether monostatic floating bodies exist; and the question of neutral floating under capillary forces etc. On the side of dynamics, verifying Lyapunov stability of equilibria in a systematic way appears to be a fundamental theoretical goal, for which we have no efficient tools at this time, and thus even the simplest model systems may pose severe difficulties.

Taking an engineer's viewpoint, we have also seen that there is a wide range of practical applications of problems related to static equilibrium. Dealing with uncertainty in a simple, efficient and reliable way is an evergreen dilemma of the engineer, when artificial systems interact with the physical world. For example, the pose statistics estimation method of Sec. 3.2 and the proposal of developing universal part feeders using round cages (Sec. 2.3) aim to be small steps towards eliminating one form of uncertainty in the process of automated industrial assembly. Stability analysis can also be interpreted as a way of dealing with unpredictable perturbing effects. A better understanding of stability properties is highly desired in the field of robotics, where the primary challenge of grasping, object manipulation and robotic locomotion is to ensure safe (stable) operation in situations where the environments and the physical models are complex and often uncertain.

4.2 SUMMARY OF MAIN RESULTS

The new results of Chapter 2 and 3 are summarized by five statements

Principal result 1 (joint work with G. Domokos). We investigated the equilibria of rigid bodies resting on a flat, horizontal surface, and

a) we proved the existence of convex, homogeneous objects, which are mono-monostatic on a horizontal surface and constructed examples of these shapes
b) we developed a parametric model of turtle shells and fitted the model parameters to the typical shapes of various turtle species. We showed that the shell shapes of some species are monostatic or almost monostatic, which allows self-righting with minimal effort on horizontal terrain.

Principal result 2. By investigating the equilibria of rigid bodies resting in a round cage in the absence of dry friction,

a) I proved that planar objects are typically either monostatic if and only if the radius of the cage is below a critical value, or they are monostatic for any cage size.
b) I developed a computational algorithm, which determines the range(s) of cage sizes, for which a planar, polygonal objects or a spatial, polyhedral object is monostatic.
c) I pointed out that the application of spherical cages in industrial part feeders offers a step towards the development of universal feeders in three dimensions.

Principal result 3: I proved the existence of rigid bodies of density ½ other than the sphere, for which floating in a liquid of density 1 in every pose corresponds to static equilibrium.

Principal result 4: With the aid of a phenomenological Markov chain model of the motion of 3-dimensional objects dropped onto a horizontal surface, I developed new simple estimators of pose statistics. By using simulations of motion over a frictionless surface as a reference, I also demonstrated that one of the new estimators outperforms previously proposed ones found in the literature.

Principal result 5: I have examined the stability properties of the equilibria of rigid bodies and multibody systems in the presence of unilateral contacts and dry friction, and

a) by considering the infinite-stiffness limit of a compliant contact model, I demonstrated that they possess static stability provided that (i) none of the contact forces is at the boundary of the associated friction cone, and (ii) if all contact are constrained to stay in stick state, then the system possesses first-order rigidity.
b) (**joint work with Joel W. Burdick and David Gontier**) we approximated the dynamics of a planar rigid body with 2 point contacts on a slope, near an equilibrium state by a piecewise linear, hybrid dynamical system, and developed a necessary condition of Lyapunov stability of the equilibrium.
c) I showed that an equilibrium may lose its Lyapunov stability via the emergence of an infinite sequence of impacts even if impacts are perfectly inelastic.

These results have been published in [53], [168], [169], [170], [171], [172], [173], [175], and [176].

CHAPTER 5:

APPENDIX

5.1 MONO-MONOSTATIC BODIES

Here we prove **Lemma 2.2.4**, **Lemma 2.2.5**, and **Lemma 2.2.6**.

5.1.1 Proof of *Lemma 2.2.4*

The poles are singular points because of the reflection-symmetry of r to the planes $\Theta=0$ and $\Theta=\pi/2$ (cf. equation (8)).

At other points, the partial derivatives of r are determined based on equations (2) and (9). The first one is:

$$\frac{\partial r}{\partial \theta} = d\,\frac{\partial a}{\partial \theta} \cdot (f_1 - f_2). \tag{132}$$

This partial derivative is zero if either

$$f_2 - f_1 = 0 \tag{133}$$

(which holds for the poles only), or

$$\frac{\partial a}{\partial \theta} = 0, \tag{134}$$

which holds if and only if $\theta=k\cdot\pi/2$. At these lines

$$r(\theta,\varphi) = 1 + d \cdot f_i(\varphi) \quad i = 1 + k \bmod 2 \tag{135}$$

(cf. equations (6) and (7)). Now, all we have to show is that the partial derivative with

respect to φ is non-zero *along these lines*. This derivative is given by

$$\frac{\partial r}{\partial \varphi} = d \cdot \frac{df_i(\varphi)}{d\varphi}, \qquad i = 1 + k \bmod 2 \tag{136}$$

which is non-zero except at the poles. Thus, there are no other singular points.

5.1.2 Proof of *Lemma 2.2.5*

The reflection symmetry of the body with respect to the $\theta=0$ and $\theta=\pi/2$ planes implies that G is on the vertical line $\varphi=\pm\pi/2$ passing through the origin O. The signed vertical distance h between O and G can be expressed as a function of the parameters c and d:

$$h(c,d) = \frac{\displaystyle\int_0^{2\pi}\int_{-\pi/2}^{\pi/2} \tfrac{1}{4} r(\varphi,\theta,c,d)^4 \cos\varphi \sin\varphi\, d\varphi\, d\theta}{V(c,d)} \tag{137}$$

where $V(c,d)$ denotes the volume of the body, and $G \equiv O$ iff $h(c,d)=0$.

Equation (137) can be transformed to.

$$h(c,d) = \frac{1}{V(c,d)} \int_0^{2\pi}\int_{-\pi/2}^{\pi/2} \tfrac{1}{4}(1 + d\Delta r(\varphi,\theta,c))^4 \cos\varphi \sin\varphi\, d\varphi\, d\theta =$$

$$= \frac{1}{V(c,d)}\left[\int_0^{2\pi}\int_{-\pi/2}^{\pi/2}\cos\varphi \sin\varphi\, d\varphi\, d\theta + d\int_0^{2\pi}\int_{-\pi/2}^{\pi/2}(\Delta r + \tfrac{3}{2}d\Delta r^2 + d^2\Delta r^3 + \tfrac{1}{4}d^3\Delta r^4)\cos\varphi \sin\varphi\, d\varphi\, d\theta \right] = \tag{138}$$

$$= \frac{1}{V(c,d)}\left[0 + d\int_0^{2\pi}\int_{-\pi/2}^{\pi/2}(\Delta r + \tfrac{3}{2}d\Delta r^2 + d^2\Delta r^3 + \tfrac{1}{4}d^3\Delta r^4)\cos\varphi \sin\varphi\, d\varphi\, d\theta \right]$$

which shows that $h(c,d)=0$ is equivalent to the condition

$$h^*(c,d) = \int_0^{2\pi} \int_{-\pi/2}^{\pi/2} (\Delta r + \tfrac{3}{2} d \Delta r^2 + d^2 \Delta r^3 + \tfrac{1}{4} d^3 \Delta r^4) \cos \varphi \sin \varphi \, d\varphi \, d\theta = 0 \qquad (139)$$

if $d>0$, moreover

$$\text{sign}\left(h(c,d)\right) = \text{sign}\left(h^*(c,d)\right) \qquad (140)$$

We remark that $h^*(c,d)$ is continuous in c and d, for $c>0$ and arbitrary d (d might be 0 as well).

Observe that

$$h^*(c,0) = \int_0^{2\pi} \int_{-\pi/2}^{\pi/2} \Delta r \cos \varphi \sin \varphi \, d\varphi \, d\theta \qquad (141)$$

is positive if c approaches infinity, because

$$\lim_{c\to\infty} \Delta r(\theta, \varphi, c) = \sin(\varphi) . \qquad (142)$$

and the product $\Delta r \cos\varphi \sin\varphi$ is nonnegative (see also Fig. 12.A).

At the same time if $c\to 0$, we have

$$\lim_{c\to +0} \Delta r(\theta, \varphi, c) = \begin{cases} 1 & \text{if} \begin{cases} -\tfrac{\pi}{2} < \varphi < 0, \theta \neq k \cdot \tfrac{\pi}{2} \\ \varphi = \tfrac{\pi}{2} \\ -\tfrac{\pi}{2} < \varphi < \tfrac{\pi}{2}, \theta = (2k+1) \cdot \tfrac{\pi}{2} \end{cases} \\ -1 & \text{if} \begin{cases} 0 < \varphi < \tfrac{\pi}{2}, \theta \neq k \cdot \tfrac{\pi}{2} \\ \varphi = -\tfrac{\pi}{2} \\ -\tfrac{\pi}{2} < \varphi < \tfrac{\pi}{2}, \theta = 2k \cdot \tfrac{\pi}{2} \end{cases} \\ \sin^2 \theta - \cos^2 \theta & \text{if} \qquad \varphi = 0 \end{cases} \qquad (143)$$

and the product $\Delta r \cos\varphi \sin\varphi$ is almost everywhere negative yielding $h^*(c,0)<0$ (cf. Fig. 12.B).

Since $h^*(c,0)$ is continuous in c, there exist positive constants $c_1<c_2$ such that $h^*(c_1,0)<0<h^*(c_2,0)$ Again, because of the continuity of $h^*(c,d)$, there exists a constant δ_0 for which $0<d<\delta_0$ implies $h^*(c_1,d)<0<h^*(c_2,d)$ (Fig. 13). So, if $0<d<\delta_0$, then there is a function $F_1(d)$ satisfying $c_1<F_1(d)<c_2$ for which $h^*(F_1(d),d)=0$ and thus $c=F_1(d)$ implies G≡O .

5.1.3 Proof of *Lemma 2.2.6*

We prepare the proof of **Lemma 2.2.6** in four parts.

In part A, a sufficient condition of local convexity is determined, based on the Hessian of the surface in a local orthogonal coordinate system. This condition can be applied everywhere, except at the poles. In part B, some functions related to r are extended to a closed domain and their boundedness is stated in **Proposition 5.1.1**. Based on these results, in part C, we prove **Proposition 5.1.2**, stating convexity at regular points (we determine a function $F_2(c)$ and show, that the surface is convex at such points if $d< F_2(c)$). Finally, it is verified in part D that the convexity requirement is fulfilled at the poles, too. This is the statement of **Proposition 5.1.3**. The three propositions together imply **Lemma 2.2.6**, which completes the proof.

A A sufficient condition for local convexity at an arbitrary point

At any surface point P with spherical coordinates φ_0, θ_0. r can be expressed as $z(x,y)$ in an x-y-z local orthogonal coordinate system, axis z passes through the origin O (see Fig. 53). A sufficient condition of local convexity is that the Hessian

$$\mathbf{H} = \begin{bmatrix} z_{xx}(c,d) & z_{xy}(c,d) \\ z_{yx}(c,d) & z_{yy}(c,d) \end{bmatrix} \tag{144}$$

of $z(x,y)$ exists and it is positive definite. Since $z_{xy}=z_{yx}$, this condition is equivalent of

$$\begin{cases} z_{xx}(c,d) > 0 \\ z_{xx}(c,d)\,z_{yy}(c,d) - z_{xy}(c,d)^2 > 0 \end{cases} \tag{145}$$

The elements of the Hessian can be expressed as functions of φ and θ. The
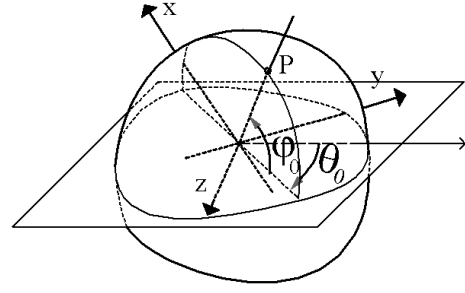
Fig. 53. Local coordinate system at point P of the surface.

following results were computed analytically for a general function of the form (2), using Maple 7. The computational details are omitted here. Lower indices in the following equations denote partial derivatives with respect to the variables in the indices.

$$z_{xx} = \frac{1}{r} - \frac{d \cdot \Delta r_{\varphi\varphi}}{r^2} + \frac{2d^2 \cdot \Delta r_\varphi^2}{r^3} \tag{146}$$

$$z_{yy} = \frac{1}{r} - \frac{d \cdot \Delta r_{\theta\theta}}{r^2 \cos^2 \varphi} + \frac{2d^2 \cdot \Delta r_\theta^2}{r^3 \cos^2 \varphi} + \frac{d \cdot \Delta r_\varphi \sin \varphi}{r^2 \cos \varphi} \tag{147}$$

$$z_{xy} = \frac{d \cdot \Delta r_{\theta\varphi}}{r^2 \cos \varphi} + \frac{d \cdot \Delta r_\theta \sin \varphi}{r^2 \cos^2 \varphi} - \frac{2d^2 \cdot \Delta r_\varphi \Delta r_\theta}{r^3 \cos^2 \varphi} \tag{148}$$

The three formulae above, substituted in equations (145) and (146) yield a sufficient condition of local convexity of the surface. It can be used anywhere but at the two poles, where the surface is not twice differentiable.

B Boundedness of some functions related to r

Here we show

Proposition 5.1.1*: There exists a positive continuous function $M(c)$ satisfying the following two conditions:*

$$\left|\Delta r_{\varphi\varphi}\left(-\pi/2, \pi/2\right)\right| < M \ . \tag{149}$$

$$\left|\frac{\Delta r_\varphi}{\cos \varphi}\right|, \left|\frac{\Delta r_\theta}{\cos^2 \varphi}\right|, \left|\Delta r_{\varphi\varphi}\right|, \left|\frac{\Delta r_{\varphi\varphi}}{\cos \varphi}\right|, \left|\frac{\Delta r_{\theta\theta}}{\cos^2 \varphi}\right| < M \qquad \text{if} \qquad |\varphi| < \pi/2 \tag{150}$$

We can trivially satisfy (149), but there is no such guarantee for the boundedness of left side of (150), since these are *continuous*

functions on open domains; observe also that the denominators $cos\varphi$ of (150)

converge to zero at the borders of the domains.

Proof of **Proposition 5.1.1**:

Let us define ext(ϕ) for a given function $\phi(\varphi,\Theta)$ with $|\varphi| < \pi/2$, as the same function on an extended, *closed* domain :

$$ext(\phi) = \begin{cases} \phi(\varphi,\Theta) & if & |\varphi| < \pi/2 \\ \lim\limits_{\varphi \to \pi/2} \phi(\varphi,\Theta) & if & \varphi = \pi/2 \\ \lim\limits_{\varphi \to -\pi/2} \phi(\varphi,\Theta) & if & \varphi = -\pi/2 \end{cases} \quad (151)$$

The following functions

$$\mathrm{ext}\left(\frac{\Delta r_\varphi}{\cos\varphi}\right), \mathrm{ext}\left(\frac{\Delta r_\theta}{\cos^2\varphi}\right), \mathrm{ext}\left(\Delta r_{\varphi\varphi}\right), \mathrm{ext}\left(\frac{\Delta r_{\varphi\theta}}{\cos\varphi}\right), \mathrm{ext}\left(\frac{\Delta r_{\theta\theta}}{\cos^2\varphi}\right) \qquad (152)$$

trivially exist and are continuous in φ and θ if $|\varphi| < \pi/2$. Simultaneously, for $|\varphi| = \pi/2$, one can determine the functions in (152) analytically, based on the definition (151) to verify the same statement.

According to our analytical computations (made with Maple 7), the corresponding limit values exist and they are continuous in θ, which imply the continuity of the extended functions (152). The results are quite lengthy, that is why only one of them is presented here:

$$\mathrm{ext}\left(\frac{\Delta r_\varphi}{\cos\varphi}\right)\Bigg|_{\varphi=+\pi/2} = \lim_{\varphi\to\pi/2}\frac{\Delta r_\varphi}{\cos\varphi} = \frac{\cos^2\theta\cdot e^{4/c}+1-\cos^2\theta}{c^2\left(e^{2/c}-2e^{1/c}+1+\cos^2\theta\cdot e^{4/c}-2\cos^2\theta\cdot e^{3/c}+2\cos^2\theta\cdot e^{1/c}-\cos^2\theta\right)} \quad (153)$$

The denominator is never zero because it equals

$$1+\cos^2\theta\cdot\left(e^{4/c}-2e^{3/c}+e^{2/c}\right)+2\cos^2\theta\cdot e^{1/c}-\cos^2\theta-2e^{1/c}+\sin^2\theta\cdot e^{2/c} > ... \qquad (154)$$

$$1+2\cos^2\theta\cdot e^{1/c}-\cos^2\theta-2e^{1/c}+\sin^2\theta\cdot e^{2/c} = \sin^2\theta\left(e^{2/c}-2e^{1/c}+1\right) > 0$$

therefore function (153) exists and it is continuous in θ.

According to the Extreme Value Theorem [22], continuous functions on compact, closed manifolds are always bounded. Thus, the maximum $M(c)$ of all the functions in (152) exists. $M(c)$ satisfies the conditions (149) and (150) and it is continuous in c.

C The function $F_2(c)$

Here we construct the function $F_2(c)$ such that whenever $d<F_2(c)$, r is convex at all regular points. In point D, we will extend this result to the poles.

Proposition 5.1.2: *If*

$$d \le F_2(c) \stackrel{def}{=} \min\left\{\frac{1}{25\,M(c)}, \frac{1}{2}\right\} \qquad (155)$$

(where M(c) is defined in **Proposition 5.1.1***) then r is convex at all regular points.*

Proof of **Proposition 5.1.2**:

By using **Proposition 5.1.1**, equation (155) and the fact that (155) implies $1/2<r<3/2$, we develop the following bounds of the elements of the Hessian (146)-(148):

$$z_{xx} \ge \frac{1}{r} - \left|\frac{d\cdot\Delta r_{\varphi\varphi}}{R^2}\right| + 0 > \frac{2}{3} - 4dM \qquad (156)$$

$$z_{yy} \ge \frac{1}{r} - \left| \frac{d \cdot \Delta r_{\theta\theta}}{r^2 \cos^2 \varphi} \right| + 0 - \left| \frac{d \cdot \Delta r_{\varphi} \sin \varphi}{r^2 \cos \varphi} \right| > \qquad (157)$$

$$> \frac{2}{3} - 4dM - 4dM \cdot \sin \varphi > \frac{2}{3} - 8dM$$

$$|z_{xy}| \le \left| \frac{d \cdot \Delta r_{\theta\varphi}}{r^2 \cos \varphi} \right| + \left| \frac{d \cdot \Delta r_{\theta} \sin \varphi}{r^2 \cos^2 \varphi} \right| + \left| \frac{2d^2 \cdot \Delta r_{\varphi} \Delta r_{\theta}}{r^3 \cos^2 \varphi} \right|$$

$$< 4dM + 4dM \sin \varphi + 16 d^2 M^2 \cdot \cos \varphi \le \qquad (158)$$

$$\le 8dM + 16 d^2 M^2$$

From inequalities (155)-(158) we conclude by:

$$z_{xx}(d) > \frac{2}{3} - 4dM \ge \frac{38}{75} > 0 \qquad (159)$$

and by

$$z_{xx}(d) z_{yy}(d) - z_{xy}(d)^2 > \dots$$

$$\left(\frac{2}{3} - 4dM \right) \left(\frac{2}{3} - 8dM \right) - \left(8dM + 16 d^2 M^2 \right)^2 \ge \dots \qquad (160)$$

$$\frac{28 \cdot 7057}{3^2 \cdot 5^8} > 0$$

ie. the conditions of convexity (145) are satisfied. The function $F_2(c)$ that we have found is continuous in c.

D Convexity at the poles.

In this part, we prove

Proposition 5.1.3: *the object is locally convex at the two poles if $d< F_2(c)$.*

Here, local convexity is demonstrated by showing a plane, which

- contains the examined pole (N or S),

- all nearby points of the surface are on the same side of the plane,
- the interior of the object is also on the same side of the plane

*Proof of **Proposition 5.1.3***:

Consider the orthogonal coordinate system of Fig. 53

with $\varphi_0 = -\pi/2$ and $\theta_0 = 0$. The plane $z=(1+d)$ contains the north pole of the surface and all other points are on the $z<1+d$ side of this plane, because

$$z(\varphi, \theta) = r(\varphi, \theta) \sin \varphi \qquad (161)$$
$$< r(\varphi, \theta) < 1 + d$$

The origin O is at $z=0$ also on the $z<1+d$ side. Thus, the surface is convex at the north pole for any value of d.

Similarly, the plane $z=-1+d$ contains the south pole and the origin O is at $z=0$ on the $z>-1+d$ side. In order to prove local convexity, we need to show

$$z(\varphi, \theta) = r(\varphi, \theta) \sin \varphi > -1 + d \qquad (162)$$

for any θ if $0<\varphi+\pi/2<<1$ and $d< F_2(c)$. The bound (162) needs a deeper investigation than (161) because r has a local minimum point at the south pole.

We start the proof of inequality (162) with the following simple identity, which is true for arbitrary positive M (see also (155)):

$$d \le \min \left\{ \frac{1}{25 M}, \frac{1}{2} \right\} < \frac{2}{3(1+M)} . \qquad (163)$$

This relation is modified in three steps, which are commented below:

$$d < \frac{2}{3(1+M)} = \frac{\frac{1}{3}(\varphi + \pi/2)^2}{\frac{1}{2}(1+M)(\varphi + \pi/2)^2} < \frac{\frac{1}{3}(\varphi + \pi/2)^2}{\frac{1}{2}(1+M)(\varphi + \pi/2)^2 - \frac{1}{4}M(\varphi + \pi/2)^4} =$$

$$\frac{1 - 1 + \frac{1}{3}(\varphi + \pi/2)^2}{1 - \left(-1 + \frac{1}{2}M(\varphi + \pi/2)^2 \right)\left(-1 + \frac{1}{2}(\varphi + \pi/2)^2 \right)} < \frac{1 + \sin \varphi}{1 - \left(-1 + \frac{1}{2}M(\varphi + \pi/2)^2 \right)\sin \varphi} < \frac{1 + \sin \varphi}{1 - \Delta R \sin \varphi}$$

$$(164)$$

The first step was obvious. In the second step we used that

$$-1 + \frac{1}{3}(\varphi + \pi/2)^2 < \sin \varphi < \tag{165}$$
$$\dots -1 + \frac{1}{2}(\varphi + \pi/2)^2$$

if $0<(\varphi+\pi/2)<<1$, which is simple to derive from the Taylor expansion of $\sin(\varphi)$ at $\varphi=-\pi/2$ up to the third-order term. The third step is a consequence of the following bound (cf. Fig. 10 and Eq. (149)):

$$\Delta r(\varphi,\theta) \le f_2(\varphi) = \Delta r(\varphi,\pi/2) =$$
$$= -1 + 0 \cdot (\varphi + \pi/2) + \frac{1}{2} r_{\varphi\varphi} (-\pi/2, \pi/2) \cdot (\varphi + \pi/2)^2 + o((\varphi + \pi/2)^3) < \tag{166}$$
$$< -1 + \frac{1}{2} M (\varphi + \pi/2)^2$$

which again holds for $0<(\varphi+\pi/2)<<1$.

Eq. (164) can be rearranged as

$$d(1 - \Delta r \sin \varphi) < 1 + \sin \varphi \tag{167}$$

Via substituting (2) into (167), we arrive to (162). Thus, the surface is convex at the south pole, too.
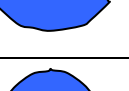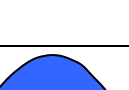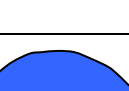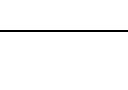
5.2 TURTLE SHELL MODEL

Measured individuals are in decreasing order based on their height/width ratio. In the last column, a second class is shown in parenthesis for individuals with parameter values very close to the boundary of two stability classes. We also measured turtles where the shell's shape has adapted to special habits (e.g. Geochelone sulcata,

digging itself into the sand, Malacochersus tornieri, squeezing the shell between rocks). Although the model could still be fitted to the shell's contour with reasonable error ($e<0.08$, see (17)), these data have been excluded from the statistics in the $[R,p]$ and $[R,k]$ parameter planes.

SERIAL #	INPUT DATA FROM MEASUREMENT			FITTED MODEL PARAMETERS			ERROR	CLASS
	species	contour of main cross section	h=height/width ratio	k	p	h	e cf. eq. (6)	
1	Geochelone elegans		0.99	-0.19	0.65	1.00	0.0006	S_3 (S_1)
2	Geochelone elegans		0.90	-0.00	1.04	0.88	0.0013	S_1

3	Stigmochelys pardalis		0.87	-0.11	0.83	0.89	0.0009	S_3 (S_1)
4	Stigmochelys pardalis		0.85	-0.27	0.63	0.85	0.0008	S_3
5	Stigmochelys pardalis		0.85	-0.14	0.63	0.85	0.0025	S_3
6	Stigmochelys pardalis		0.85	-0.32	0.49	0.85	0.0015	S_3
7	Geochelone elegans		0.85	-0.06	1.07	0.84	0.0012	S_2 (S_1)
8	Astrochelys radiata		0.84	-0.00	0.84	0.85	0.0012	S_3 (S_1)
9	Stigmochelys pardalis		0.83	-0.39	0.48	0.83	0.0012	S_3
10	Stigmochelys pardalis		0.82	-0.31	0.93	0.81	0.0007	S_2
11	Stigmochelys pardalis		0.81	-0.38	0.55	0.80	0.0014	S_3
12	Stigmochelys pardalis		0.79	-0.39	0.51	0.79	0.0007	S_3
13	Stigmochelys pardalis		0.79	-0.27	0.49	0.81	0.0010	S_3
14	Psammobates tentorius		0.79	-0.42	0.34	0.79	0.0013	S_3
15	Stigmochelys pardalis		0.79	-0.42	0.34	0.79	0.0013	S_3

16	Terrapene carolina triungis		0.78	-0.47	0.21	0.78	0.0028	S_3
17	Stigmochelys pardalis		0.78	-0.38	0.23	0.78	0.0009	S_3
18	Chelonoidis carbonaria		0.78	-0.29	0.50	0.79	0.0022	S_3
19	Testudo graeca anamurensis		0.72	-0.33	0.84	0.73	0.0013	S_2
20	Chelonoidis nigra		0.72	-0.19	0.95	0.72	0.0013	S_2
21	Chelonoidis carbonaria		0.68	-0.12	0.96	0.70	0.0023	S_2
22	Eurotestudo hermanni		0.67	-0.31	0.59	0.66	0.0009	S_3 (S_2)
23	Eurotestudo hermanni		0.65	-0.34	0.34	0.65	0.0011	S_3 (S_2)
24	Terrapene carolina bauri		0.64	-0.57	-0.06	0.65	0.0013	S_3 (S_2)
25	Trachemys scripta elegans		0.63	-0.73	-0.06	0.67	0.0032	S_3 (S_2)
26	Cuora amboinensis		0.58	-0.58	-0.29	0.63	0.0071	S_3 (S_2)
27	Rhinoclemmys pulcherrima manni		0.56	-0.55	-0.36	0.58	0.0020	S_3 (S_2)
28	Phrynops hilarii		0.45	-0.73	0.13	0.47	0.0028	S_2

29	Carettochelys insculpta		0.43	-0.61	-0.18	0.46	0.0051	S_2
30	Chelonia mydas		0.41	-0.33	-1.02	0.43	0.0050	S_3 (S_2)

5.3 PART FEEDERS

5.3.1 Planar α-edges are not bigger than a semi-circle

Assume that a circle segment e with endpoints V_1 and V_2, contains a semi-circle s with endpoints S_1 and S_2 (Fig. 54) and it is an α-edge of a planar object Ω. e does not intersect Ω but at its endpoints (which are vertices of the α-hull), thus s does not intersect Ω. Let $d>0$ denote the smallest distance between points of Ω and of s. By the definition of the α-hull, the full circle c fitted to e encloses Ω. We shift c by distance $d/2$ in a direction perpendicular to S_1S_2 such that it ceases to cover the area filled by grey color in Fig. 54. Nevertheless the distance of any point of the grey area from the closest point of s is $\leq d/2$, i.e. Ω remains covered by the shifted circle. Hence the grey area of Fig. 54 is not part of the α-hull, contradicting the initial assumption that e is an α-edge.

5.3.2 Proof of *Lemma 2.4.2*

Consider a planar object resting in a circular cage. All frictionless support reactions point towards the center O of the cage. Hence the equilibrium of moments about O is satisfied if and only if condition (i) of ***Lemma 2.4.2*** is true.

The vector sum of the support reaction(s) is vertical and points upwards. Thus, there exists a force with upward pointing vertical component among the support reaction(s). Similarly, there exists a force with non-positive, and one with non-negative horizontal component. Such forces act at the lower, the left and the right halves of the cage, respectively. Thus the contact set must contain point(s) belonging to each of these three parts. At the same time, the contact set is either a single point or an α-edge not bigger than a semi-circle (Appendix A). These properties of the α-edge imply that condition (ii) is necessary. To show that condition (ii) is also sufficient, note that (1) *the endpoints of the contact set are vertices of the α-hull, which are actual contact points between the object and the cage*; and (2) *the endpoints of a contact set containing P are in the lower left and lower right quarters of the cage, respectively.* Observations (1), (2) imply that the weight of the object can be balanced by frictionless contact forces at the endpoints of the contact set, or by a single one if the contact set is a single point. Hence the object is in
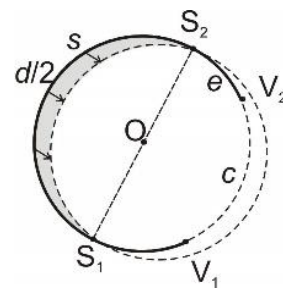
Fig. 54. Illustration of Appendix 5.3.1.

equilibrium. Finally, the condition (iii) of stability is proved in [160] §586.

5.4 FLOATING OBJECTS .

This section contains some technical details of the proof of Lemma 2.5.2.

5.4.1 Deviation of a_{ij} from its trivial value

a_{ij} is given by (36) as a partial derivative of G_i, which is defined by an improper integral in(31). We define a new function

$$Q(\alpha,\phi,Y_j(\alpha)) \overset{def}{=} \begin{cases} Z(\alpha,\phi,Y_j(\alpha))^2 \left(1-\dfrac{\alpha}{\phi}\right)^{-1} & if \quad \alpha < \phi \\ \lim_{\beta \to \phi^-} Q(\beta,\phi,Y_j(\beta)) & if \quad \alpha = \phi \end{cases} \qquad (168)$$

where $\beta \to \phi^-$ means a left limit of β. Eq. (168) will prove useful later, see Appendix 5.4.3. This definition is motivated by the square-root type singularity of Z at $\alpha=\phi$,

which implies that Q is bounded and strictly positive. With the new function and equations (24)-(26),(31) we obtain

$$G_i(\alpha,\chi,Y_j(\alpha)) = \int_\alpha^\chi (\chi-\phi)^{-1/2} \left(1-\frac{\alpha}{\phi}\right)^{1/2} \sqrt{Q(\alpha,\phi,Y_j(\alpha))}(Y_j(\alpha)-b(\phi))^i d\phi \qquad (169)$$

The variable ϕ of integration is changed to $\Gamma=(\chi-\phi)^{1/2}\cdot(\chi-\alpha)^{-1/2}$:

$$G_i(\alpha,\chi,Y_j(\alpha)) = 2(\chi-\alpha)\int_0^1 \left(\chi+\alpha\frac{\Gamma^2}{1-\Gamma^2}\right)^{-1/2} Q^{1/2}\left(\alpha,\chi-\Gamma^2(\chi-\alpha),Y_j(\alpha)\right)\left(Y_j(\alpha)-b\left(\chi-\Gamma^2(\chi-\alpha)\right)\right)^i d\Gamma \qquad (170)$$

This form of G_i is a *proper integral*, and also free of terms diverging to infinity at $\alpha=\chi$. a_{ij} can now be calculated from (36) and (170) by using the Leibniz rule, then by plugging $\alpha=\chi$, and finally by evaluating a simple integral:

$$a_{ij}(\chi,Y_j(\chi)) =$$

$$\dots \frac{\pi}{2}\chi^{-1/2}Q^{1/2}\left(\chi,\chi,Y_j(\chi)\right)\left(Y_j(\chi)-b(\chi)\right)^i \qquad (171)$$

The formula above contains $Q(\chi,\chi,Y_j(\chi))$, which can be expressed as a function of $X()$:

$$Q(\chi,\chi,Y_j(\chi))$$

$$= \lim_{\alpha \to \chi^-} \frac{X^2(\alpha,Y_j(\alpha)) - X^2(\chi,Y_j(\alpha))}{1-\alpha/\chi}$$

$$= -\chi \lim_{\alpha \to \chi} \frac{X^2(\chi,Y_j(\alpha)) - X_j^2(\alpha,Y_j(\alpha))}{\chi-\alpha} \qquad (172)$$

$$= -\chi \frac{\partial}{\partial \chi}X^2(\chi,Y_j(\alpha))\bigg|_{\alpha=\chi}$$

We plug this equation into (171) and use (21) to express a_{ij} explicitly as a function of Y_j:

$$a_{ij}\left(\chi, Y_j(\chi)\right) = \frac{\pi}{\sqrt{2}} \left(-\chi \left. \frac{\partial X^2(\chi, Y_j(\alpha))}{\partial \chi} \right|_{\alpha=\chi} \right)^{1/2} \left(Y_j(\chi) - b(\chi)\right)^i =$$

$$= \frac{\pi}{2} \sqrt{ -\frac{\partial}{\partial \chi} \left[\left(\tilde{a}(\chi)\chi + Y_j(\alpha) - b(\chi)\right)^2 \left(\chi^{-2} - 1\right) \right] \bigg|_{\alpha=\chi}} \cdot \left(Y_j(\chi) - b(\chi)\right)^i$$

(173)

Eq. (40) and point (ii) of **Lemma 2.5.2** can be expressed as: $Y_j(\chi) \in (-1)^{j+1}\chi \pm \varepsilon \exp(k\chi)$ and $\tilde{a}(\chi), b(\chi), \tilde{a}'(\chi), b'(\chi) \in \pm\varepsilon \in \pm\varepsilon\exp(k\chi)$. Plugging these into (173) together with the inequality $\chi \geq \alpha_1$; replacing higher order terms in ε by a small constant time ε; and noting that the term under the square-root sign has a strictly positive lower bound lead to the final expression

$$a_{ij}\left(\chi, Y_j(\chi)\right) \in \dots$$

$$(-1)^{i(j+1)} \frac{\pi}{\sqrt{2}} \chi^{i-1/2} \pm k_1 \varepsilon e^{k\chi}$$

(174)

with some positive constant k_1 not specified for brevity. This is the result we had to prove.

5.4.2 A lower bound of detA

An approximation of a_{ij} with $*\varepsilon\exp(k\chi)$ uncertainty has been given by (174). This formula yields

$$\det \mathbf{A} = \dots$$

$$a_{11}a_{22} - a_{12}a_{21} \in \pi^2\chi^2 \pm *\varepsilon \exp(k\chi)$$

(175)

Since $\chi > \alpha_1$, we have found a positive lower bound of det$\mathbf{A}$.

5.4.3 The second derivative of G_i

This section is devoted to the proof of equation (41). The second derivative of G_i is calculated from (170) by successive applications of the Leibniz rule. The result

(calculated by Maple software and not shown) can be written in the form

$$\frac{\partial^2 G_i(\alpha, \chi, Y_j(\alpha))}{\partial \chi^2} = \int_0^1 \sum_k \left(W_{1k} \cdot W_{2k} \cdot \dots\right) d\Gamma$$

(176)

where W_{lk} are functions of $i, j, \alpha, \chi, \Gamma, Y_j(\alpha)$, $a()$ and $b()$. Specifically, they include constants and eight non-constant terms listed below:

1: $\left(\chi + \alpha \dfrac{\Gamma^2}{1 - \Gamma^2}\right)^{-1/2}$

2: $Y_j(\alpha) - b\left(\chi - \Gamma^2(\chi - \alpha)\right)$

3: $b'\left(\chi - \Gamma^2(\chi - \alpha)\right)$

4: $b''\left(\chi - \Gamma^2(\chi - \alpha)\right)$

5: $Q(\alpha, \phi, Y_j(\alpha))^{1/2}$, where $\phi = \chi - \Gamma^2(\chi - \alpha)$

6: $Q(\alpha, \phi, Y_j(\alpha))^{-1/2}$, where $\phi = \chi - \Gamma^2(\chi - \alpha)$

7: $\left(1 - \Gamma^2\right) \left. \dfrac{\partial Q(\alpha, \phi, Y_j(\alpha))}{\partial \phi} \right|_{\phi = \chi - \Gamma^2(\chi - \alpha)}$

8: $\left(1 - \Gamma^2\right)^2 \left. \dfrac{\partial^2 Q(\alpha, \phi, Y_j(\alpha))}{\partial \phi^2} \right|_{\phi = \chi - \Gamma^2(\chi - \alpha)}$

As we show below, each term has a bounded absolute value, and its deviation from its trivial value is at most $constant \cdot \varepsilon\exp(k\alpha)$.

Term 1 is not bigger than $\chi^{-1/2}$, hence it is bounded from above by the constant $\alpha_1^{-1/2}$; this term is not affected by perturbations of

the water envelope, since it does not depend on any of the functions Y_j a or b.

Term 2 takes the form

$$Y_j(\alpha) - b\big(\chi - \Gamma^2(\chi - \alpha)\big)...$$

$$\in (-1)^{j+1}\alpha \pm \varepsilon e^{k\alpha} \pm \varepsilon$$

$$\in (-1)^{j+1}\alpha \pm 2\varepsilon e^{k\alpha}$$

Term 3 and 4 are $\in 0 \pm \varepsilon \in 0 \pm \varepsilon e^{k\alpha}$

Term 5 and 6: it is enough to show that $Q(...)$ itself has an absolute value bounded from above *and below* by positive bounds, and that it is affected by at most a constant times $\varepsilon\exp(k\alpha)$ by the perturbation. By using (21), (22) and (168), expanding the nominator and ordering its terms into pairs (marked by square brackets), Q can be expressed as

$$Q(\alpha,\phi,Y_j(\alpha)) = \frac{(\tilde{a}(\alpha) + (Y_j(\alpha) - b(\alpha))\alpha^{-1})^2 (1 - \alpha^2) - (\tilde{a}(\phi) + (Y_j(\alpha) - b(\phi))\phi^{-1})^2 (1 - \phi^2)}{1 - \alpha/\phi} = ...$$

$$= \phi \frac{\big[\tilde{a}(\alpha)^2 - \tilde{a}(\phi)^2\big] - \big[\alpha^2\tilde{a}(\alpha)^2 - \phi^2\tilde{a}(\phi)^2\big] + Y_i^2(\alpha)\big[\alpha^{-2} - \phi^{-2}\big] + etc.}{\phi - \alpha} = ...$$

$$= \frac{\left[\overbrace{(\tilde{a}(\alpha) - \tilde{a}(\phi))}^{\in \pm\varepsilon(\phi-\alpha)}\overbrace{(\tilde{a}(\alpha) + \tilde{a}(\phi))}^{\in \pm 2\varepsilon} \right]\phi - \left[\overbrace{(\alpha\tilde{a}(\alpha) - \phi\tilde{a}(\phi))}^{\in \pm 2\varepsilon(\phi-\alpha)}\overbrace{(\alpha\tilde{a}(\alpha) + \phi\tilde{a}(\phi))}^{\in \pm 2\varepsilon} \right]\phi + \left[\overbrace{\phi Y_j^2(\alpha)\overbrace{(\alpha^{-2} - \phi^{-2})}}^{\in\left(1+\frac{\alpha}{\phi}\right)(\phi-\alpha)\pm\varepsilon e^{k\alpha}\, 2\alpha_1^{-3}(\phi-\alpha)} \right] + etc.\ ...}{\phi - \alpha}$$

Only a few terms of the nominator are shown. Each square bracket in the nominator can be expressed as $*\cdot(\phi\text{-}\alpha)$ in order to cancel the denominator. This step is straightforward in some cases, but less so in others. For example, in the case of the first two square brackets, we use that $|\tilde{a}(\alpha)|, |\tilde{a}'(\alpha)| < \varepsilon$; at the third one, we exploit that $Y_j(\alpha)=(-1)^{j+1}\alpha$ if $\alpha\leq\alpha 1$ and that (40) holds and $\alpha^{-2}-\phi^{-2}\in\pm 2\alpha_1^{-3}(\phi\text{-}\alpha)$ if $\alpha>\alpha_1$. This calculation boils down to

$$Q(\alpha,\phi,Y_j(\alpha))\in 1+\alpha/\phi \pm *\cdot\varepsilon\exp(k\alpha). \quad (177)$$

Term 7: The trivial value of Q is given by (177). This is used to determine the trivial value of term 7, which is bounded because

$$\left(1 - \Gamma^2\right)\frac{\partial Q(\alpha,\phi,Y_j(\alpha))}{\partial\phi}\bigg|_{\phi=\chi-\Gamma^2(\chi-\alpha)}$$

$$= \frac{\phi - \alpha}{\chi - \alpha}\cdot\left(-\frac{\alpha}{\phi^2}\right) \qquad (178)$$

$$= \begin{cases} \frac{\phi - \alpha}{\chi - \alpha}\frac{\alpha}{\phi}\phi^{-1} \leq 1\cdot 1\cdot\left(\frac{\alpha_1}{2}\right)^{-1} & if\ \alpha \geq \chi/2 \\ \frac{\phi - \alpha}{\phi}\frac{\alpha}{\phi}(\chi - \alpha)^{-1} \leq 1\cdot 1\cdot\left(\frac{\alpha_1}{2}\right)^{-1} & \leq if\ \alpha \leq \chi/2 \end{cases}$$

The deviation of term 7 from its trivial value can be obtained analogously to the calculations of term 5 and 6 by exploiting that the first *and second* derivatives of $\tilde{a}$ and b are $\in\pm\varepsilon$. These are not shown for brevity.

Term 8: the trivial value can be investigated using a formula similar to (178):

$$\left(1 - \Gamma^2\right)^2 \cdot \left.\frac{\partial Q\left(\alpha, \phi, Y_j(\alpha)\right)}{\partial \phi}\right|_{\phi = \chi - \Gamma^2(\chi - \alpha)}$$

$$= \left(\frac{\phi - \alpha}{\chi - \alpha}\right)^2 \frac{2\alpha}{\phi^3}$$

$$= \begin{cases} 2\left(\dfrac{\phi - \alpha}{\chi - \alpha}\right)^2 \dfrac{\alpha}{\phi}\phi^{-2} \leq 2 \cdot 1 \cdot 1 \cdot \left(\dfrac{\alpha_1}{2}\right)^{-2} & \text{if } \alpha \geq \chi/2 \\[3ex] 2\left(\dfrac{\phi - \alpha}{\phi}\right)^2 \dfrac{\alpha}{\phi}(\chi - \alpha)^{-2} \leq 2 \cdot 1 \cdot 1 \cdot \left(\dfrac{\alpha_1}{2}\right)^{-2} & \text{if } \alpha \leq \chi/2 \end{cases}$$

As before, explicit bounds of the nontrivial value are not shown. They can be obtained by exploiting that the derivatives of $\widetilde{a}$ and b up to third order are $\in 0 \pm \varepsilon$.

Both of these properties are inherited by the second derivative of G_i according to eq. (176). This final step leads us to (41).

5.5 POSE STATISTICS

5.5.1 Dynamic simulation

The estimators of Sec. 3.2 were tested against a dataset on pose statistics generated by numerical simulation. $n=100$ drop tests have been simulated with each of 1057 random polyhedra (see point A, below). Frictionless impacts were assumed with the restitution coefficient first set to $\rho=0.2$. Then, the tests were repeated with $\rho=0.5$ and 0.8. The simulations yield 3 datasets each consisting of N simulated probabilities, where $N=6665$ is the total number of stable poses summed for the 1057 objects. The polyhedra of the dataset had 2 to 21 stable poses and the associated probabilities are in the range 0-0.75. There were no monostatic objects in the dataset.

The details of the object generation and the dynamic simulation are given below. The algorithm has been implemented under MATLAB R2010b. The run time of a single drop test on a PC (CPU: Intel Core2 2.5 GHz; OS: Microsoft Windows 7) is in the range of 0.2-5 sec. The execution time is low if the coefficient of restitution for impacts is low or if the stable facets are large.

A Random shapes

Convex, random polyhedra are generated by the following algorithm:

- Random points are generated in 3-space. Each coordinate of each point is drawn from a normal distribution with mean 0 and variance 1; the number of points is $4+\xi$, where ξ is a random number from a geometric distribution with parameter 0.1.
- The convex hull of the points (found by any standard method) provides the surface of the object. This is a convex polyhedron with triangular faces. In the actual dataset the number of vertices is in the range 4-23; the number of faces is between 4 and 42. The mass, the location of the center of mass, and the moment of inertia tensor of the object are calculated by assuming constant unit mass-density inside the polyhedron.
- The object is resized to set the maximum of the distance function $r(\mathbf{u})$ to 1.
- To include objects representing inhomogeneous and/or concave parts, the center of mass is shifted by random numbers d_i ($i=1,2,3$) along the eigenvectors of the moment of inertia tensor. The variables d_i are drawn from uniform distributions over the intervals $(-q_i, q_i)$ where q_i are the corresponding radii of gyration of the object (i.e. q_i^2 are the eigenvalues of the moment of inertia tensor divided by the mass of the object).

B State variables of the objects and initial conditions

The motion of the objects is described in a Cartesian reference frame with axes *x-y-z*. The *z* axis points vertically upwards. The support surface is the *z*=0 horizontal plane. The dynamic state of a rigid body is determined by the vertical coordinate $z_O(t)$ of its center of mass and its time derivative $\dot{z}_o(t)$; a 3 by 3 rotation matrix **R** representing its orientation; and its 3 by 1 angular velocity vector $\boldsymbol{\omega}$. The horizontal dynamics of O is trivial because all external forces acting on the object are vertical. Initially (*t*=0), the object is high above the surface relative to its size ($z_O(0)$=20). The initial orientation is chosen randomly with uniform distribution using an algorithm from [5]; the initial velocity and angular velocity are zero.

C Continuous dynamics

The moving polyhedron is in one of the following contact modes: free fall, sliding on a vertex, sliding on an edge (i.e. 2 vertices), and sliding or resting on a face (i.e. 3 vertices). Accordingly, it is assumed that the ground exerts nonnegative, vertical contact forces to *k*=0, 1, 2, or 3 vertices of the object, which are in contact with the ground. More than 3 contact points are also possible if an object has coplanar triangular faces, but this scenario does not occur for shapes obtained by taking the convex hull of generic random points. The Newton-Euler equations and *k* contact constraints are used to determine the *k* contact forces together with the resulting acceleration and angular acceleration of the object. This way, the continuous motion of the object is determined by integrating a system of first order, ordinary differential equation in the variables z_O and $\dot{z}_o = v_o$, **R**, $\boldsymbol{\omega}$, see point D below for details.

The integration of the ODE is interrupted whenever an impact between the object and the surface is detected (see point E below), or whenever one of the contact forces becomes negative.

D Equations of motion

The ODE describing the continuous motion of the object consists of the following parts:

Newton's law: $\dot{v}_o = -g + m^{-1}\sum_{j=1}^{k} N_j$ (179)

Euler's equations of motion: (180)
$$\dot{\boldsymbol{\omega}} = -\mathbf{I}^{-1}\left(\Omega\mathbf{I}\boldsymbol{\omega} + \sum_{j=1}^{k} N_j \mathbf{r}_j \times \mathbf{u}_z \right)$$

kinematic identity: $\dot{z}_o = v_o$ (181)

kinematic identity: $\dot{\mathbf{R}} = \mathbf{R}\Omega$ (182)

where *g* is the constant of gravity; *m* is the mass of the object and **I** denotes its moment of inertia tensor in local coordinates; N_j are the contact forces, *k* is the number of sliding contacts, and $\mathbf{r}_j$ stand for the position vectors of the corresponding vertices in local coordinates; $\mathbf{u}_z$ is an upward pointing vertical unit vector. Ω is the matrix corresponding to the $\boldsymbol{\omega}\times$ cross product operation (i.e. $\Omega\mathbf{x}=\boldsymbol{\omega}\times\mathbf{x}$ for any **x**); Ω contains 0's and the elements of $\boldsymbol{\omega}$.

The contact forces N_j are determined from the non-penetration constraints $z_O+\mathbf{u}_z^T\mathbf{R}\mathbf{r}_j$=0. Substitution of (181), (182) into the second time derivative of this constraint yields

$$\dot{v}_o + \mathbf{u}_z^T \mathbf{R}\left(\Omega\Omega + \dot{\Omega}\right)\mathbf{r}_j = 0 \qquad (183)$$

Substituting (179), (180) into (183) yields a system of linear algebraic equations for the contact forces.

E Modeling impacts

Single-vertex impacts are assumed to be frictionless (i.e. impact momenta are

vertical) with Newtonian coefficient of restitution ρ. The impact impulse and the post-impact velocity of the object are determined uniquely by the linear and angular momentum laws and the coefficient of restitution. Simultaneous impacts at several vertices are not determined uniquely by these laws. We treat them as sequences of single-vertex impacts. In each step, the vertex with the highest velocity pointing towards the underlying surface is assumed to undergo an impact. The impact sequence ends if none of the vertices moves towards the underlying surface or if a Zeno point is detected (see point F below).

The modelling of simultaneous impacts is not possible without ad hoc rules such as the one described above [143]. As we have explained earlier, it is one of the basic assumptions of this work that pose statistics are not sensitive to this type of modelling error.

F   Detecting Zeno points

An approaching Zeno point is indicated by an impact event, at which the pre-impact vertical velocities of all vertices that are very close to the ground (the threshold 10^{-9} is used in the simulation), are either positive (moving upwards) or very close to zero (threshold: -10^{-5}) and the set of 'slowly moving vertices' with velocity very close to zero is nonempty. If this situation is detected, we apply appropriately chosen instantaneous, vertical impulses at the set of slowly moving vertices, in order to change their vertical velocities to 0. The necessary impulses are determined uniquely by the linear and angular momentum laws. This impulse is an approximate replacement for the infinitely many small impacts leading to the Zeno point. After the impulse, the contact mode of the object switches to sliding on these vertices.

G   Termination

The simulation is completed if a face of the object establishes contact with the surface. The object conserves its 0 initial angular momentum about the z axis, hence face-contact implies immobility.

5.5.2   Algorithm of the MEAE estimator

The MEAE estimator works in the following steps:

1: the stable faces are found by testing every face one by one. For specific formulas, see [94] [168]. Those nodes of the splitting graph, which are labelled by a single stable pose are drawn.

2: the saddle points of r are found by testing every edge one by one. The edges with saddle points are $l_1, l_2, \ldots, l_H$ and the critical values of r are $r_1 \le r_2, \le \ldots \le r_H$.

3: The distance of every edge (including those without saddle points) from the center of mass is determined.

4: The following steps are repeated for every critical value r_i, $i=1,2,\ldots,H$.

4A: a connectivity graph of faces is generated by testing every edge one by one. Two faces are connected if they share an edge, which is closer to the center of mass than r_i.

4B: the connected components of the connectivity graph are found using a breadth-first traverse.

4C: if the two faces adjacent to edge l_i are in different components (Γ_{ia} and Γ_{ib}) of the connectivity graph, then a splitting event of the reachable set occurs at the examined saddle point. Accordingly, two edges and a node are added to the splitting graph. If not, then the steps 4D-E are skipped.

4D: for each facet in the components Γ_{ia} and Γ_{ib}, the centroid solid angles of the areas over which $r(\mathbf{u}) < r_i$, are determined. The centroid solid angles are summed within

each component to obtain $\Omega(\Gamma_{ia})$ and $\Omega(\Gamma_{ib})$.

4E: The transition probabilities associated with the splitting event are determined using (69).

5: the probabilities found in step 4F are propagated down the complete splitting graph to obtain the estimation.

A polyhedron with v vertices has O(v) edges and facets. Hence, the computational complexity of all steps is at most O(v). For almost all shapes, the number of stable poses and saddle points are only O(1), i.e. step 4 is repeated O(1) times. In sum, the complexity of the estimator is O(v).

5.6 LOCAL DYNAMICS AND STATIC STABILITY

This appendix shows that the local minimum of the potential energy implies stability against small variations of the loads, as long as the external loads and the contact dynamics are conservative or dissipative. This an extension of the classical LeJeune Dirichlet theorem [91]. Perturbations are small in the following sense:

Definition 5.6.1: *the norm of a system of conservative or dissipative external forces (in the sense of condition (iii) of Sec. 3.3.2) is the supremum of* $\left\|\mathrm{grad}\ P(\mathbf{q})\right\|$ *where P(**q**) is the corresponding potential over the configuration space.*

The exact statement and its proof are given below.

Theorem 5.6.2: *if a system of rigid bodies is in equilibrium and conditions (i)-(iii) of **Theorem 3.3.1** are satisfied, then for any scalar* δ *there is another scalar* φ *such that after any instantaneous variation of the external loads of norm not exceeding* φ*, the configuration **q**(t) of the system satisfies* $||\boldsymbol{q}(t)\text{-}\boldsymbol{q}_0||<\delta$ *for all t.*

Before presenting the proof, the following notations are introduced: let E_k and $\tilde{E}_k = \varepsilon^{-1} E_k$ denote the unscaled and scaled kinetic energies of the system; let the scalar M denote a 'characteristic mass' of the system such that the kinetic energy of the

system is $E(\mathbf{q}, \dot{\mathbf{q}}) > M \mid \dot{\mathbf{q}} \mid^2$ for any $\mathbf{q}$ and $\dot{\mathbf{q}}$. Then, $\tilde{E} > M \mid \mathbf{q}' \mid^2$ where ' denotes derivative with respect to rescaled time $\tilde{t} = \varepsilon^{-1/2} t$

*Proof of **Theorem 5.6.2**:* the contact functions $S^{(i)}$ are assumed to be continuous in their input variables $\mathbf{f}^{(i)}$, which are themselves smooth functions of their own input variables $\tilde{\mathbf{q}}$, $\tilde{\mathbf{q}}'$. Furthermore, all contact functions take strictly positive values in the initial equilibrium state by assumption (i) of Sec. 3.3.2. Together these statements imply that there exists a small scalar δ such that if

$$\left\|\tilde{\mathbf{q}} - \tilde{\mathbf{e}}\right\| < \delta \qquad (184)$$

and

$$\left\|\tilde{\mathbf{q}}'\right\| < \delta \qquad (185)$$

then all contact functions remain positive. The system can move anywhere inside this region of the state space without contact slip or separation.

It has been shown in Sec. 3.3.4 that $\tilde{P}(\tilde{\mathbf{q}})$ has a minimum at $\tilde{\mathbf{q}} = \tilde{\mathbf{e}}$ and the minimum value of the function is 0. Minima of smooth functions are surrounded by a foliation of level sets, forming topological balls. Hence, given an arbitrary positive scalar δ, there

exists a small, positive scalar δ_1 such that the level set $\tilde{P} = \delta_1$ in the configuration space is a topological ball enclosing $\tilde{\mathbf{q}} = \tilde{\mathbf{e}}$, furthermore all points of the enclosing ball satisfy $|\tilde{\mathbf{q}} - \tilde{\mathbf{e}}| < \delta$. This ball is denoted by Λ. Within this ball, (184) is satisfied. We use Λ as a cage bounding those configurations, which are reachable by the system after the perturbation.

A perturbation of the external loads corresponds to a small perturbation $\hat{\mathbf{p}}_1$ of $\mathbf{p}_1$ in (84). If the norm of the perturbation is smaller than δ_1/δ, then by definition, $|\hat{\mathbf{p}}_1| < \delta_1/\delta$, implying $|\hat{\mathbf{p}}_1^T \tilde{\mathbf{q}}| < \delta_1$ $\|\hat{\mathbf{p}}_1^T \tilde{\mathbf{q}}\| < \delta_1$ for all $|\tilde{\mathbf{q}} - \tilde{\mathbf{e}}| < \delta$. Hence, $\tilde{P}$ remains positive everywhere on Λ, i.e. the ball Λ is an unreachable energy barrier for the perturbed system (as long as the contacts remain in stick state). If the norm of the perturbation is also smaller than $m\delta_1^2/\delta$, then the lowest value of $\tilde{P}$ within Λ is not

less than $-m\delta_1^2$, i.e. the rescaled kinetic energy $\tilde{E}$ of the system moving inside Λ may not exceed $m\delta_1^2$; and thus (185) is satisfied.

In summary, we have found, that for perturbations of norm smaller than min[δ_1/δ, $m\delta_1^2/\delta$], the system stays within distance δ to its initial configuration, and all contacts remain in stick mode.

The threshold found above is independent of ε, i.e. the sensitivity of the system to perturbations does not blow up in the limit $\varepsilon \to 0$. In contrast, stability against dynamic perturbations does vanish in the quasi-rigid limit. Dynamic perturbations may increase the total energy of the system by a small amount (by adding some initial velocity or displacement). At the same time a given variation of the unscaled energy corresponds to increasingly large variation of the rescaled potential energy $\tilde{P}$ as ε goes to zero. Hence, static stability does not imply LS.

5.7 LYAPUNOV STABILITY

5.7.1 Details of the proof of *Lemma 3.4.2*

A Free-flight followed by a sticking impact

Recall that we restrict our attention to the case $x_1(t_k) > x_1(t_{k-1})$ and $\ddot{x}_1^{(FF)} > 0$ (see(106)). During free flight, the total energy is constant, hence

$$U(t_k^-) - U(t_{k-1}^+) = \\ \dots \sin \alpha \left(x_1(t_k) - x_1(t_{k-1}) \right) \tag{186}$$

Furthermore, the acceleration $\ddot{z}_i$ of leg i is constant as given by (95), thus the duration of the free flight phase is

$$t_k - t_{k-1} \leq \frac{2 | \dot{z}_i(t_k^-) |}{\cos \alpha - Tl_i} \tag{187}$$

The right-hand side is positive by (105). The bound (187) is sharp iff leg i lifts off from the ground at time t_{k-1}. The positive horizontal acceleration of P_i ($\ddot{x}_1 > 0$) yields

$$\dot{x}_i(t_k^-) \geq \frac{x(t_k) - x(t_{k-1})}{t_k - t_{k-1}} (> 0) \tag{188}$$

During impacts, x_1 and E_p do not change thus U is affected solely by the absorption of kinetic energy. The latter equals the variation of the so-called *contact energy* $E_i = \frac{1}{2}\mathbf{v}_i^T \mathbf{M}_{ii} \mathbf{v}_i$ associated with the impacting point P_i. For details see [102]. Furthermore, it can be shown for sticking impacts that changing both restitution parameters e and e_t to $\nu = \max(e, |e_T|)$ yields a lower bound of the energy absorption (proof omitted for brevity). In this case, the velocity vector of the contact point changes by a factor $-\nu$ during the impact yielding

$$U(t_k^-) - U(t_k^+) \geq \ldots$$
$$\geq (1 - \nu^2)\frac{1}{2}\mathbf{v}_i^T(t_k^-)\mathbf{M}_{ii}\mathbf{v}_i(t_k^-)$$
$$\geq \frac{(1 - \nu^2)\left(\sqrt{(1 + h^2)(1 + l_i^2)} + hl_i\right)}{1 + h^2 + l_i^2} \cdot \ldots \quad (189)$$
$$\ldots \cdot |\dot{x}_i(t_k^-)\dot{z}_i(t_k^-)|$$

where we have used (94), the identity $a^2 + b^2 \geq 2|ab|$, as well as $\dot{z}_i(t_k^-) \leq 0$ and $\dot{x}_i(t_k^-) \geq 0$ (by (188)).

By expressing $|\dot{z}_i|$ from (187) and by using (188), we can transform inequality (189) into

$$U(t_k^-) - U(t_k^+) \geq \left(x(t_k) - x(t_{k-1})\right) \cdot \ldots$$
$$\ldots \cdot \frac{(1 - \nu^2)\left(\sqrt{(1 + h^2)(1 + l_i^2)} + hl_i\right)}{1 + h^2 + l_i^2} \cdot \ldots \quad (190)$$
$$\ldots \cdot \frac{\cos \alpha - Tl_i}{2}$$

Altogether, by adding the inequalities (186) and (190), we obtain (118) with

$$c = -\sin \alpha + $$
$$\ldots + \frac{(1 - \nu^2)\left(\sqrt{(1 + h^2)(1 + l_i^2)} + hl_i\right)}{1 + h^2 + l_i^2} \cdot \ldots \quad (191)$$
$$\ldots \cdot \frac{\cos \alpha - Tl_i}{2}$$

where $c > 0$ iff (107) is satisfied.

B Free-flight followed by a right sliding ($\varepsilon = -1$) impact

Similarly to the previous point, the variation of U during the impact is calculated as the variation of the contact energy. Using (93) we obtain

$$U(t_k^-) - U(t_k^+) = \ldots$$
$$= -\mathbf{v}_i^T(t_k^-)\mathbf{p} - \frac{1}{2}\mathbf{p}^T\mathbf{M}_{ii}^{-1}\mathbf{p} \quad (192)$$

The impact momentum $\mathbf{p}$ is determined from (94) and (102):

$$\mathbf{p} = \frac{-(1 + e)\dot{z}_i(t_k^-)}{-\mu_i hl_i + 1 + l_i^2}\begin{bmatrix} -\mu_i \\ 1 \end{bmatrix}$$
$$\overset{def}{=} \beta |\dot{z}_i(t_k^-)|\begin{bmatrix} -\mu_i \\ 1 \end{bmatrix} \quad (193)$$

if $1 + l_i^2 - \mu_i hl_i < 0$ then β is negative, which is unphysical. In this case, a sliding impact is impossible, and further investigation of this case is unnecessary. In the opposite case, (192) and (193) yield

$$U(t_k^-) - U(t_k^+) = \dot{x}_i(t_k^-)|\dot{z}_i(t_k^-)| \cdot \ldots$$
$$\ldots \cdot \beta\left(\mu_i + \gamma \frac{|\dot{z}_i(t_k^-)|}{\dot{x}_i(t_k^-)}\right) \quad (194)$$

with

$$\gamma = -1 + \frac{\beta}{2}\left((h\mu_i - l_i)^2 + (1 + \mu_i^2)\right) \quad (195)$$

γ may be positive or negative. These two cases are investigated separately, below.

If $\gamma \geq 0$, then we have

$$U(t_k^-) - U(t_k^+) \geq \dots$$
$$\dots \dot{x}_i(t_k^-) \mid \dot{z}_i(t_k^-) \mid \beta \mu_i \qquad (196)$$

because $\dot{x}_i(t_k^-) > 0$ by (188). The bound (196) is used analogously to (189) in the case of a sticking impact to arrive to (118) with

$$c = -\sin\alpha + \frac{(\cos\alpha - Tl_i)\mu_i(1+e)}{2(1+l_i^2 - \mu_i hl_i)} \qquad (197)$$

where $c > 0$ under the condition (108).

If $\gamma < 0$, then we have $U(t_k^+) - U(t_k^-) > 0$ for high values of $\frac{|\dot{z}_i(t_k^-)|}{\dot{x}_i(t_k^-)}$, which would mean energy gain during impact. Thus, in reality, the impact must become sticking above a certain threshold of $\frac{|\dot{z}_i(t_k^-)|}{\dot{x}_i(t_k^-)}$. As the transition point to sticking impact corresponds to the worst case scenario, i.e. minimal energy absorption, one can use the bound developed for sticking impacts and conclude in the same way as in that case.

C Free-flight followed by a left sliding ($\varepsilon=1$) impact

While a left-sliding impact is rare if $\dot{x}_i(t_k^-) > 0$, it is possible for certain geometrical settings and low friction. Thus, this case also needs to be considered. Through steps analogous to the previous point, one arrives to the expression (194) with the quantity μ_i replaced by $-\mu_i$. In particular the right-hand side contains $-\mu_i + \gamma \frac{|\dot{z}_i(t_k^-)|}{\dot{x}_i(t_k^-)}$. If $\gamma \leq 0$, this term is always negative, i.e. the formula predicts energy gain, indicating that a left-sliding impact is not possible. For $\gamma > 0$, we have energy absorption for high values of $\frac{|\dot{z}_i(t_k^-)|}{\dot{x}_i(t_k^-)}$, and left-sliding impacts might only occur above a certain threshold. The worst case scenario

(minimum energy absorption) again corresponds to the transition point to sticking impact, and the reasoning of that case is again applicable.

D Sliding in the positive direction on one leg

If the object slides to the right on leg i (i.e. $z_i=0$, $\dot{x}_i > 0$), while the other one is separated from the ground, then the contact force at leg i is is

$$\mathbf{f}_i = \frac{\cos\alpha - Tl_i}{1 + l_i^2 - \mu_i hl_i} \begin{bmatrix} -\mu_i \\ 1 \end{bmatrix}$$
$$\overset{def}{=} f \begin{bmatrix} -\mu_i \\ 1 \end{bmatrix} \qquad (198)$$

see the explanation of the analogous equation (131). f is negative if $1 + l_i^2 - \mu_i hl_i < 0$, implying that this case is unphysical and need not be investigated. Otherwise, we take the time derivative of (114)

$$\dot{U}(t) = \dot{E}_p + \dot{E}_k + \dot{x}_i \sin\alpha \qquad (199)$$

$\dot{E}_p + \dot{E}_k$ can be calculated as the (negative) power of the friction force, i.e. $-\mu_1 f \dot{x}_i$. Thus,

$$\dot{U} = \left(\sin\alpha - \mu_i \frac{\cos\alpha - Tl_i}{1 + l_i^2 - \mu_i hl_i}\right)\dot{x}_i \qquad (200)$$

This formula is rearranged to obtain (118) with

$$c = -\sin\alpha + \mu_i \frac{\cos\alpha - Tl_i}{1 + l_i^2 - \mu_i hl_i} \qquad (201)$$

The positiveness of c is equivalent of the condition

$$\sin\alpha\left(1 + l_i^2 - \mu_i hl_i\right) < \mu_i\left(\cos\alpha - Tl_i\right) \qquad (202)$$

which follows from the more restrictive condition (108).

The friction coefficients are high enough to keep the object balanced before the initial perturbation; hence if sliding motion of the same object is possible, then it is deccelerating. Furthermore, the variation of E_p and the work of the frictional forces are both proportional to the displacement of the object; thus the same proportionality applies to the variation of E_k. In summary, $\partial E_k / \partial x_1 = -c$ where c is a positive constant. If both legs are in contact with the ground, then by (114), $U - E_k$ = constant, implying (119).

5.7.2 Differences between the proof of *Lemma 3.4.3* and that of *Lemma 3.4.2*.

As we have seen, the proof of **Lemma 3.4.2** consists of three parts (with several subcases)

1. the net change of U during an episode of free flight to the right and during the impact immediately after this episode is negative and proportional to the distance travelled to the right
2. *U* decreases continuously during sustained sliding motion to the right in proportion to the distance travelled
3. *U* does not increase during motion to the left

The arguments used to demonstrate points 2 and 3 remain valid in the case of **Lemma 3.4.3**. Point 1 has to be changed because (188) is no more true. Instead, (109) implies

$$\dot{x}_i(t_{k-1}^+) \geq \frac{x(t_k) - x(t_{k-1})}{t_k - t_{k-1}} \qquad (203)$$

in this case. By using the new inequality, one can demonstrate that the the net change of U during an episode of free flight to the right and during the impact immediately *before this episode* (rather than after this episode) is negative. This difference is responsible for the upper indices $^-$ instead of $^+$ in the statement of **Lemma 3.4.3**. The steps of the proof are the same as in the case of **Lemma 3.4.3**, but we arrive to the condition (110) instead of (107) and to the condition

$$\sin \alpha \left(1 + l_i^2 - \mu_i h l_i\right) < (\cos \alpha - T l_i) \frac{(1+e)\mu_i}{2e} \qquad (204)$$

instead of (108). (204) is less restrictive then the condition (202) necessary for decreasing U during sustained sliding motion, hence a copy of (202) emerges in the statement of **Theorem 3.4.1** as condition (111).

5.7.3 Boundedness of the feasible region of inequalities (112), (113), (129)

(113) can be expressed in terms of z_i and x_1 using (90), (103) as

$$\frac{l_2 \cos \alpha - h \sin \alpha + T}{l_2 - l_1} z_1 + \ldots$$

$$\ldots \frac{-l_1 \cos \alpha + h \sin \alpha - T}{l_2 - l_1} z_2 - \ldots \qquad (205)$$

$$\ldots \sin \alpha x_1 \leq \text{constant} \cdot |\mathbf{q}(0)|$$

The coefficients of z_i are positive by the equilibrium conditions (87) and (88). Hence (205) takes the form $C_1 z_1 + C_2 z_2 - C_3 x_1 \leq C_0$ with $C_1, C_2, C_3 > 0$. By adding $C_3 x_{1,\max}$ to the left side (where $x_{1,\max}$ is defined by (129)) we obtain

$$C_1 z_1 + C_2 z_2 + C_3 \left(x_{1,\max} - x_1 \right) \le \text{constant} \ \cdot | \mathbf{q}(0) |$$

According to (112) and (129), this is equivalent of

$$C_1 \left| z_1 \right| + C_2 \left| z_2 \right| + C_3 \left| x_{1,\max} - x_1 \right|$$
$$\le \text{constant} \ \cdot | \mathbf{q}(0) |$$

(206)

i.e. the feasible region in 3D *configuration space* is bounded and its size is proportional to |**q**(0)|. The feasible region in the six-dimensional *state space* is also bounded an proportional in size to |**q**(0)|, which can be shown easily by using the trivial energy bound $E_k(t) \le E_p(0) + E_k(0) - E_p(t)$.

REFERENCES

[1] Akella, S., Mason, M. T., 1999, Using partial sensor information to orient parts, *Int. J. Robot. Res*. 18, 963-997.

[2] Ames A. D., H. Zheng, R. D. Gregg, and S. Sastry, Is there life after Zeno? Taking executions past the breaking (Zeno) point, in *Proc. Amer. Control Conf.,* pp. 6, 2006.

[3] Arnold, V.I., *Ordinary Differential Equations*, 10th printing, MIT Press, 1998.

[4] Arnold, V.I: Personal communication to G. Domokos.

[5] Arvo J., Fast random rotation matrices, in David Kirk, *Graphics Gems III*, San Diego: Academic Press Professional, pp. 117–120, ISBN 978-0-12-409671-4, 1992.

[6] Ashe, V. M., 1970, The righting reflex in turtles: A description and comparison. *Psychon. Sci*. 20, 150-152.

[7] Ashmore, G. M., Janzen, F., 2003, Phenotypic variation in smooth softshell turtles (Apalone mutica) from eggs incubated in constant versus fluctuating temperatures. *Oecologia* 134, 182-188.

[8] Auerbach H., 1938, Sur un probleme de M. Ulam concernant l'équilibre des corps flottants, *Studia Math* 7, 121-142.

[9] Bagi, K., 2014, When Heyman's Safe Theorem of rigid block systems fails: Non-Heymanian collapse modes of masonry structures, *Int. J. Solids Struct.* 51, pp. 2696-2705.

[10] Balkcom D. and J. Trinkle, 2002, Computing wrench cones for planar rigid body contact tasks, *Int. J. Robot. Res*. 21, 1053–1066.

[11] Bass D. W., 1980, Stability of icebergs. *Annals of Glaciology* 1, 43-47.

[12] Benson, R. B., Domokos, G., Várkonyi, P. L., Reisz, R. R., 2011, Shell geometry and habitat determination in extinct and extant turtles (Reptilia: Testudinata). *Paleobiology,* 37(04), 547-562.

[13] Berger, E. J., 2002, Friction modeling for dynamic system simulation. Applied Mechanics Reviews 55.6, 535-577.

[14] Berger M., Gostiaux B, *Differential geometry: Manifolds, curves and surfaces.* Springer, New York, 1988.

[15] Berkowitz D. R., and J. Canny, Designing parts feeders using dynamic simulation, in *Proc. IEEE ICRA*, 1127-1132, 1996.

[16] Bernardo, M., Budd, C., Champneys, A. R., & Kowalczyk, P., Piecewise-smooth dynamical systems: theory and applications (Vol. 163). Springer Science & Business Media, 2008.

[17] Berretty, R. P., Goldberg, K., Overmars, M. H. and Van der Stappen, A. F., 2001, Trap design for vibratory bowl feeders, *Int. J. Robot. Res.* 20, 891-908.

[18] Berretty, R. P., Overmars, M. H. , Van der Stappen, A. F., 2002, Orienting polyhedral parts by pushing, *Comput. Geom.* 21, 21-38.

[19] Berretty, R. P., Overmars, M. H. and van der Stappen, A. F., On fence design and the complexity of push plans for orienting parts, in *Proc. 13th Ann. ACM Symp. Comput. Geom.*, pp. 21-29., 1997.

[20] Bicchi, A., 1995, On the closure properties of robotic grasping, *Int. J. Robot. Res*. 14, 319-334.

[21] Bicchi, A., and Kumar, V., Robotic grasping and contact: A review, *Proc. IEEE ICRA*, 348 – 353, 2000.

[22] Böhringer, K.-F, Donald, B. R., Kavraki, L. and Lamiraux, F., 2000, Part orientation with one or two stable equilibria using programmable vector fields, *IEEE Trans. Robot. Autom.* 16, 157-170.

[23] Bonnet, X. et al., 2001, Sexual dimorphism in steppe tortoises (Testudo horsfieldii): influence of the environment and sexual selection on body shape and mobility. *Biol. J. Linn. Soc.*, 72, 357–372.

[24] Bonnet, X., Delmas, V., El-Mouden, H., Slimani, T., Sterijovski, B., & Kuchling, G., 2010, Is sexual body shape dimorphism consistent in aquatic and terrestrial chelonians?. *Zoology* 113, 213-220.

[25] Boothroyd G. and C. Ho , 1977, Natural resting aspects of parts for automatic handling, *J. Eng. for Industry* 99, 314-317.

[26] Boothroyd G., A. H. Redford, C. R. Poli, and L. E. Murch, 1972, Statistical distribution of natural resting aspects of parts for automatic handling, *Manuf. Eng. Trans.* 1, 93-105.

[27] Bouyarmane K. , A. Escande, F. Lamiraux, and A. Kheddar, Potential field guide for humanoid multicontacts acyclic motion planning, in *Proc. IEEE ICRA*, 1165-1170, 2009.

[28] Bouyarmane K., A. Escande, F. Lamiraux, and A. Kheddar, Stable transport of assemblies: Pushing stacked parts, in *Proc. IEEE IROS*, 3180-3185, 2003.

[29] Bower, A. F, *Applied mechanics of solids*. Taylor and Francis, ISBN: 978-1439802472, 2011.

[30] Bretl T., 2006, Motion planning of multi-limbed robots subject to equilibrium constraints: The free-climbing robot problem, *Int. J. Robot. Res*. 25, 317-342.

[31] Brogliato, B. *Nonsmooth dynamics: models, dynamics and Control*, 3rd ed., Springer, New York, 2016.

[32] Bretl T. and S. Lall, 2008, Testing static equilibrium for legged robots, *IEEE Trans. Robot.* 24, 794–807.

[33] Burger J., Carruth-Hinchey C., Ondroff J., McMahon M., Gibbons J. W., Gochfeld M., 1998, Effects of lead on behavior, growth, and survival of hatchling slider turtles. *J. Toxicol. Environ. Health A*. 55, 495-502.

[34] Carlisle B., Goldberg K., Rao A., and Wiegley J., A pivoting gripper for feeding industrial parts, in *Proc. IEEE ICRA*, 1650-1655, 1994.

[35] Carr A. F., *Handbook of turtles. The Turtles of the United States, Canada, and Baja California*, Ithaca, NY: Cornell University Press, 1952.

[36] Champneys, A. R., Várkonyi, P. L., 2016, The Painlevé paradox in contact mechanics, *IMA Journal of Applied Mathematics* 81, 538-588 .

[37] Chatterjee A. and A. Ruina, 1998, A new algebraic rigid body collision law based on impulse space considerations, *ASME J. Appl. Mech.* 65, 939–951.

[38] Cheong, J. S., Van der Stappen, A. F., Goldberg, K. Y., Overmars M. H., and Rimon, E., 2007, Immobilizing hinged polygons, *Int. J. Computational Geometry and Applications,* 17 45–70.

[39] Chiari, Y., Hyseni, C., Fritts, T. H., Glaberman, S., Marquez, C., Gibbs, J. P., Caccone, A., 2009, Morphometrics parallel genetics in a newly discovered and endangered taxon of Galápagos tortoise. *PLoS One,* 4, e6272.

[40] Chua P. S. K and M. L. Tay, 1998, Modelling the natural resting aspect of small regular shaped parts, *J. Manuf. Sci. Eng*. 120, 540-546.

[41] Claude, J., Paradis, E., Tong, H., Auffray J-C., 2003, A geometric morphometric assessment of the effects of environment and cladogenesis on the evolution of the turtle shell. *Biol. J. Linn. Soc*. 79, 485-501.

[42] Coddington Earl A., Levinson N., *Theory of Ordinary Differential Equations*, McGraw-Hill, New York, 1955.

[43] Conway, J.H. and Guy, R., 1969, Stability of Polyhedra, *SIAM Rev.* 11, 78-82.

[44] Cutkosky, M. R., *Robotic grasping and fine manipulation*, Kluwer, Boston. ISBN: 978-1-4684-6893-9, 1985.

[45] D'Ayala, D. F., and Tomasoni, E., The structural behavior of masonry vaults: Limit state analysis with finite friction.

Proc. 6th Int. Conf. Structural Analysis of Historic Construction, D'Ayala and Fodde, eds., 47-61, 2008.

[46] Dawson, R. and Finbow, W., 1999, What shape is a loaded die? *Mathematical Intelligencer* 22, 32-37.

[47] Dawson, R., 1985, Monostatic Simplexes, *Amer. Math. Monthly* 92, 541-646.

[48] Domokos G., Lángi Zs., Szabó T., 2015, A topological classification of convex bodies. *Geometriae Dedicata* 182, 95-116.

[49] Domokos G., Papadopulos J., Ruina A., 1994, Static equilibria of planar, rigid bodies: is there anything new? *J. Elasticity* 36, 59-66.

[50] Domokos, G., 2006, My lunch with Arnold. *Math. Intelligencer* 28(4), 31-33.

[51] Domokos, G., Sipos, A. Á., Szabó, T., 2012, The mechanics of rocking stones: equilibria on separated scales. *Mathematical Geosciences* 44, 71-89.

[52] Domokos, G., Sipos, A., Szabó, T., Várkonyi, P., 2010, Pebbles, shapes, and equilibria. *Mathematical Geosciences*, 42, 29-47.

[53] Domokos, G., Várkonyi, P. L., 2008, Geometry and self-righting of turtles. *Proc. Royal Society of London B: Biological Sciences* 275(1630), 11-17.

[54] Edelsbrunner, H., Mücke, E. P., 1994, Three-dimensional alpha shapes. *ACM Trans. Graphics* 13, 43-72.

[55] Elnitsky, M. A., Claussen, D. L., 2006, The effects of temperature and inter-individual variation on the locomotor performance of juvenile turtles. *J. Comp. Physiol. B* 176, 497–504.

[56] Erdmann M., Mason, M. T., Vaněček, G. Jr., 1993, Mechanical parts orienting: The case of a polyhedron on a table, *Algorithmica* 10, 226-247.

[57] Erdős P. , G. Schibler, R. C. Herndon, 1992, Floating equilibrium of symmetrical objects and the breaking of symmetry. Part 1: Prisms. *American Journal of Physics* 60, 335-345.

[58] Erdős P., G. Schibler, R. C. Herndon, 1992, Floating equilibrium of symmetrical objects and the breaking of symmetry. Part 2: The cube, the octahedron, and the tetrahedron. *American Journal of Physics* 60, 345-356.

[59] Faisal, A. A., Matheson, T., 2001, Coordinated righting behavior in locusts. *J. Exp. Biol.* 204, 637-648.

[60] Falconer K. J., 1983, Applications of a Result on Spherical Integration to the Theory of Convex Sets, *Amer. Math. Monthly*, 90: 690-693.

[61] Farkas, M., *Periodic Motions*, Springer, New York, 1994.

[62] Finn R., Sloss M., 2009, Floating Bodies in Neutral Equilibrium, *J. Math. Fluid Mech.* 11, 459–463.

[63] Finn R., 2009, Floating Bodies Subject to Capillary Attractions, *J. Math. Fluid Mech.* 11, 443–458.

[64] Frantsevich, L. I., Mokrushov, P. A., 1980, Turning and Righting in Geotrupes (Coleoptera, Scarabaeidae). *J. Comp. Physiol.* 136, 279-289.

[65] Frantsevich, L., 2004, Righting kinematics in beetles (Insecta: Coleoptera). *Arthropod Struct. & Dev.* 33, 221-236.

[66] Freedberg, S., Stumpf, A. L., Ewert, M. A., Nelson, C. E., 2004, Developmental environment has long-lasting effects on behavioral performance in two turtles with environmental sex determination *Evol. Ecol. Research*, 6, 739-747.

[67] Garcia M. , A. Chatterjee, A. Ruina, and M. Coleman, 1998, The simplest walking model: Stability, complexity, and scaling, J. Biomech. Eng. 120, 281–288.

[68] Gilbert E. N., 1991, How things float. *Amer. Math. Monthly* 98, 201–216.

[69] Goemans O. C. and A. F. van der Stappen, 2008, On the design of traps for feeding 3D parts on vibratory tracks, *Robotica* 26, 537-550.

[70] Goemans O. C., K. Goldberg, and A.F. van der Stappen. Blades: a new class of geometric primitives for feeding 3D parts on vibratory tracks *Proc. IEEE ICRA*, 1730-1736, 2006.

[71] Goldberg K., B. V. Mirtich, Y. Zhuang, J. Craig, B. R. Carlisle, and J. Canny, 1999, Part pose statistics: estimators and experiments, *IEEE Trans. Robot. Autom.* 15, 849-857.

[72] Golubović, A, Tomović, L., and Ivanović, A., 2015, Geometry of self righting: the case of Hermann's tortoises. *Zoologischer Anzeiger-A Journal of Comparative Zoology* 254, 99-105.

[73] Golubović, A., Bonnet, X., Djordjević, S., Djurakic, M., Tomović, L., 2013, Variations in righting behavior across Hermann's tortoise populations. *Journal of Zoology*, 291, 69-75.

[74] Gopalakrishnan, K., and Goldberg, K., 2005, D-space and deform closure grasps of deformable parts. *Int. J. Robot. Res*. 24, 899-910.

[75] Greenfield A., Rizzi, A. A., Choset, H., Dynamic ambiguities in frictional rigid-body systems with application to climbing via bracing, *Proc. IEEE ICRA,* 1959–1964, 2005.

[76] Gutkin E., Addendum to: Capillary floating and the billiard ball problem, arXiv preprint arXiv:1206.2272, 2012.

[77] Gutkin E., 2012, Capillary floating and the billiard ball problem. *J. Math. Fluid Mech.* 14, 363-382.

[78] Hauser K. Bretl, T., Latombe, J.-C., Harada, K., Wilcox, B., 2008, Motion planning for legged robots on varied terrain, *Int. J. Robot. Res*. 27, 1325–1349.

[79] Heppes, A., 1967, A double-tipping tetrahedron, *SIAM Rev*. 9, 599-600.

[80] Hervé, B., Sinou, J. J., Mahé, H., Jezequel, L., 2008, Analysis of squeal noise and mode coupling instabilities including damping and gyroscopic effects. *European Journal of Mechanics-A/Solids* 27, 141-160.

[81] Heslot, F., et al.,1994, Creep, stick-slip, and dry-friction dynamics: Experiments and a heuristic model. *Physical review E* 49.6, 4973.

[82] Heyman, J., 1966, The Stone Skeleton, *Int. J. Solids Struct*., 2, 249-279.

[83] Hibbeler, R. C., Structural Analysis, 7th Ed., Prentice Hall. ISBN: 9789810680077, 2009.

[84] Highfield, A. C., 1989, Notes on dietary constituents for herbivorous terrestrial chelonian and their effects on growth and development. *ASRA (UK) J.* 3, 7–20.

[85] Hirai K. , M. Hirose, Y. Haikawa, and T. Takenaka, The development of honda humanoid robot, *Proc. IEEE ICRA*, 1321– 1326, 1998.

[86] Hitakawa, H., 1988, Advanced parts orientation system has wide application, *Assembly Autom.* 8, 147-150.

[87] Hoffmann, N., Fischer, M., Allgaier, R., Gaul, L., 2002, A minimal model for studying properties of the mode-coupling type instability in friction induced oscillations. *Mechanics Research Communications* 29, 197-205.

[88] Holmes P. , R. J. Full, D. E. Koditschek, and J. Guckenheimer, 2006, The dynamics of legged locomotion: Models, analyses, and challenges, *SIAM Review* 48, 207–304.

[89] Howard, W. S., and Kumar, V., 1996, On the stability of grasped objects, *IEEE Trans. Robot. Autom.* 12, 904-917.

[90] https://achtungberlin.de/archiv/ab_2010/514.html

[91] Neimark, J. I., Fufaev, N. A.,*Dynamics of Nonholonomic Systems,* American Mathematical Society, 1972.

[92] Jellett, J. H. *A Treatise on the Theory of Friction*. Hodges, Foster, and Company, 1872.

[93] Jen, F., Shoham, M., and Longman, R. W, 1996, Liapunov stability of force-controlled grasps with a multi-fingered hand, *Int. J. Robot. Res*. 15, 137-154.

[94] Kriegman D. J., 1997, Let them fall where they may: Capture regions of curved objects and polyhedral. *Int. J. Robot. Res.* 16, 448-472.

[95] Kriegman, David J. Computing stable poses of piecewise smooth objects, *IEEE Workshop on Directions in Automated CAD-Based Vision*, 66-75, 1991.

[96] Kuffner J. , K. Nishiwaki, S. Kagami, M. Inaba, and H. Inoue, Motion planning for humanoid robots under obstacle and dynamic balance constraints, in *Proc. IEEE ICRA*, 692–698, 2001.

[97] Kumar, V. C., and I. M. Hutchings, 2004, Reduction of the sliding friction of metals by the application of longitudinal or transverse ultrasonic vibration, *Tribology International* 37, 833-840.

[98] Le Xuan Anh, *Dynamics of Mechanical Systems with Coulomb Friction (Foundations of Engineering Mechanics).* Springer, New York, 2003.

[99] Lee S. S. G., B. K. A. Ngoi, L. E. N. Lim, and S. W. Lye, 1997, Determining the probabilities of the natural resting aspects of parts from their geometries, *Assembly Autom.* 17, pp. 137–42.

[100] Leine, R. I., van de Wouw, N., 2008, Stability properties of equilibrium sets of non-linear mechanical systems with dry friction and impact. *Nonlinear Dynamics* 51, 551-583.

[101] Lynch K. M. , M. Northrop, and P. Pan, 2002, Stable limit sets in a dynamic parts feeder, *IEEE Trans. Robot. Autom.* 18, 608-615, 2002.

[102] Malik, S. C., *Mathematical analysis*, 2nd ed., Wiley, New York., 1992.

[103] Mann, G. K. H., O'Riain M. J., Hofmeyr, M. D., 2006, Shaping up to fight: sexual selection influences body shape and size in the fighting tortoise (Chersina angulata). *J. Zoology* 269, 373–379.

[104] Mason M. T., *Mechanics of Robotic Manipulation*, 1st. ed. MIT Press, 2001.

[105] Mason, R., Rimon, E. and Burdick, J., Stable poses of 3-dimensional objects, *Proc. IEEE ICRA*, 391-398, 1997.

[106] Mauldin R. D. , *The Scottish Book, Mathematics from the Scottish Café*, Birkhauser, Boston, 1981.

[107] Mazonka O., Solid Angle of Conical Surfaces, Polyhedral Cones, and Intersecting Spherical Caps. arXiv preprint, arXiv: 1205.1396, 2012.

[108] Megiddo, N., 1983, Linear-time algorithms for linear programming in R3 and related problems, *SIAM J. Comput.* 12, 759-775.

[109] Miller K. S. and Ross B. , *An Introduction to the Fractional Calculus and Fractional Differential Equations*. John Wiley & Sons 1993.

[110] Moll, M. and Erdmann, M. A., 2002, Manipulation of pose distributions, *Int. J. Robot. Res.* 21, 277-292.

[111] Montana, D. J., 1992, Contact stability for two-fingered grasps, *IEEE Trans. Robot. Autom.* 8, 421-430.

[112] Montejano L., 1974, On a problem of Ulam concerning a characterization of the sphere, *Studies in Appl. Math.* LIII: 243-248.

[113] Mulgaonkar, Y., Kientz, T., Whitzer, M., Kumar, V.. Design and Fabrication of Safe, Light-Weight, Flying Robots. In *ASME 2015 International Design Engineering Technical Conferences and Computers and Information in Engineering Conference* V05BT08A021. American Society of Mechanical Engineers, 2015.

[114] Myers, E. M., Janzen, F. J., Adams, D. C., Tucker, J. K., 2006, Quantitative genetics of plastron shape in slider turtles (Trachemys scripta). *Evolution.* 60, 563-572.

[115] Neubauer W., A spider-like robot that climbs vertically in ducts or pipes, in *Proc. IEEE IROS*, 1994.

[116] Ngoi B. K. A. , L. E. N. Lim, and S. S. G. Lee, 1998, Analyzing the Probabilities of Natural Resting for a Component With a Virtual Resting Face, *J. Manuf. Sci. Eng.* 120, 468-471.

[117] Ngoi B. K. A. and L. E. N. Lim, 1996, Analysing the Natural Resting Aspect of a Component for Automated Assembly using the Energy Envelope Method, *Int. J. Adv. Manuf. Technol.* 12, 132-136.

[118] Ngoi B. K. A., L. E. N. Lim, and J. T. Lee, 1997, Analysis of natural resting aspects of parts in a vibratory bowl feeder-Validation of drop test *Int. J. Adv. Manuf. Technol.* 13, 300-310.

[119] Nguyen V.-D., Constructing force-closure grasps, in *Proc. IEEE ICRA*, 1368– 1373, 1986.

[120] Nguyen, V. D., 1989, Constructing stable grasps, *Int. J. Robot. Res.* 8, 26-37.

[121] Nguyen, V.D., 1988, Constructing force-closure grasps. *Int. J. Robot. Res.* 7, 3-16.

[122] Nordmark, A., Dankowicz, H., Champneys, A., 2011, Friction-induced reverse chatter in rigid-body mechanisms with impacts, *IMA J. Appl. Math.* 76, 85-119.

[123] Nowacki, H., Archimedes and ship stability. In: *Passenger ship design, construction, operation and safety* : Euroconference; Knossos Royal Village, Anissaras, Crete, Greece, October 15-17, 2001, 335-360 (2002). Ed: Kaklis, P.D. National Technical Univ. of Athens, Department of Naval Architecture and Marine Engineering, Athens.

[124] Nye J. F. and Potter J. R., 1980, The use of catastrophe theory to analyze the stability and toppling of icebergs. *Annals of Glaciology* 1, 49-54.

[125] Omata, T., and Nagata, K., 2000, Rigid body analysis of the indeterminate grasp force in power grasps, *IEEE Trans. Robot. Autom.* 16, 46-54.

[126] Or Y. and E. Rimon, On the hybrid dynamics of planar mechanisms supported by frictional contacts. ii: Stability of two-contact rigid body postures, in *Proc. IEEE ICRA*, 1219–1224, 2008.

[127] Or, Y., 2014, Painlevé's Paradox and Dynamic Jamming in Simple Models of Passive Dynamic Walking, *Regul. Chaotic Dyn.*, 19, 64-80.

[128] Or, Y., and Rimon, E., On the hybrid dynamics of planar mechanisms supported by frictional contacts. i: Necessary stability conditions, *Proc. IEEE ICRA*, 1213–1218, 2008.

[129] Painlevé, P., 1895, Sur les lois du frottement du glissement, *C. R. Acad. Sci. (Paris)* 121, 112–115.

[130] Pak, I., Lectures on discrete and polyhedral geometry. Preliminary version available at author's web page.

[131] Pang, J.-S., and Trinkle, J. C., 2000, Stability characterizations of rigid body contact problems with coulomb friction, *Zeitschrift für Angewandte Math. und Mech.* 80, 643–663.

[132] Posa, M., Tobenkin, M., Tedrake, R., 2016, Stability Analysis and Control of Rigid-Body Systems with Impacts and Friction. *IEEE Trans. Autom. Contr.* 61, 1423-1437.

[133] Pritchard P. C. H., 1979, *Encyclopedia of Turtles*, Neptune New Jersey: T.F.H. Publications.

[134] Raphael E., di Meglio J-M., Berger M., and Calabi E., 1992, Convex particles at interfaces, *J. Phys. I France* 2: 571-579.

[135] Rimon E. , R. Mason, J. W. Burdick, and Y. Or, 2008, A general stance stability test based on stratified morse theory with application to quasistatic locomotion planning, *IEEE Trans. Robot.* 24, 626–641, 2008.

[136] Rimon E. and J. W. Burdick, On force and form closure for multiple finger grasps, in *Proc. IEEE ICRA*, 1795-1800, 1996.

[137] Rimon, E., personal communication

[138] Rimon, E., and Burdick, J. W., 1998, Mobility of bodies in contact. I. A 2nd-order mobility index for multiple-finger grasps, *IEEE Trans. Robot. Autom.* 14, 696-708.

[139] Rimon, E., Burdick, J. W., Omata, T., 2006, A polyhedral bound on the indeterminate contact forces in planar, quasi-static fixturing and grasping arrangements, *IEEE Trans. Robot.* 240-255.

[140] Rivera, A. R. V., Rivera, G., Blob, R. W, 2004, Kinematics of the righting response in inverted turtles *J. Morphology*, 260**,** 322.

[141] Rivera, G., Stayton, C. T., 2011, Finite element modeling of shell shape in the freshwater turtle Pseudemys concinna reveals a trade-off between mechanical strength and hydrodynamic efficiency. *Journal of morphology* 272, 1192-1203.

[142] Rivera, G., Stayton, C. T., 2013, Effects of asymmetry on the strength of the chelonian shell: A comparison of three species. *Journal of morphology*, 274, 901-908.

[143] Rodriguez A., and A. Bowling, 2012, Solution to indeterminate multipoint impact with frictional contact using constraints, *Multibody Syst. Dyn.* 28, 313-330.

[144] Rouault, J., Blanc, C. P., 1978, Notes on the reptiles of Tunisia. V. Biometric characteristics of Mauremys caspica leprosa (Schweigger, 1812), in French. *Arch. Inst. Pasteur Tunis.* 55(3):337-57.

[145] Schneider R., 1970, Functional equations connected with rotations and their geometrical applications, *L'enseignement math*. 16, 297-305.

[146] Shapiro, A., Rimon, E., and Ohev-Zion, A., 2013, On the mechanics of natural compliance in frictional contacts and its effect on grasp stiffness and stability, *Int. J. Robot. Res*. 32, 425-445.

[147] Slaboch B. J., and P. A. Voglewede, 2012, Underactuated Part Alignment System for Industrial Assembly Applications, *J. Mechanisms Robot*. 5, 011006.

[148] Song P., J. C. Trinkle, V. Kumar, and J. S. Pang, Design of part feeding and assembly processes with dynamics, in *Proc. IEEE ICRA*, 39-44, 2004.

[149] Squyres, S, et al., 2004, The Opportunity Rover's Athena science investigation at Meridiani Planum, Mars, *Science*, 306, 1698-1703.

[150] Stancher, G., Clara, E., Regolin, L., Vallortigara, G., 2006, Lateralized righting behavior in the tortoise (Testudo hermanni) *Behavioral Brain Res*. 173, 315–319.

[151] Stayton, C. T., 2011, Biomechanics on the half shell: functional performance influences patterns of morphological variation in the emydid turtle carapace. *Zoology*, 114, 213-223.

[152] Stewart, D. E., 2000, Rigid-Body Dynamics with Friction and Impact, *SIAM Rev*. 42, 3–39.

[153] Steyermark A. C., Spotila, J. R., 2001, Maternal identity and egg incubation temperature effects on snapping turtle (Chelydra serpentina) righting response. *Copeia* 4,1050–1057.

[154] Stojadinović, D., Milošević, Đ., Crnobrnja-Isailović, J., 2013, Righting time versus shell size and shape dimorphism in adult Hermann's tortoises: Field observations meet theoretical predictions. *Animal Biology* 63, 381-396.

[155] Storck, H., Littmann, W., Wallaschek, J., Mracek, 2002, The effect of friction reduction in presence of ultrasonic vibrations and its relevance to travelling wave ultrasonic motors, *Ultrasonics* 40, 379-383.

[156] Sudsang, A. and Kavraki, L. E., A geometric approach to designing a programmable force field with a unique stable equilibrium for parts in the plane, in *Proc. IEEE ICRA*, 1079-1085, 2001.

[157] Sudsang, A. and Kavraki, L., Part orientation with a force field: Orienting multiple shapes using a single field, in *Proc. IEEE IROS* 208-213, 2001.

[158] Suresh M., K. A. Jagadeesh, and P. A. Varthanan, 2013, Determining the natural resting orientation of a part using drop test and theoretical methods, *J. Manuf. Syst*. 32, 220–227,.

[159] Terasaki H. and Hasegawa T., 1998, Motion planning of intelligent manipulation by a parallel two-fingered gripper equipped with a simple rotating mechanism, *IEEE Trans. Robot. Autom*. 14, 207-219.

[160] Thomson, W. (Lord Kelvin), Tait. P. G., *Elements of natural philosophy*, Cambridge University Press, 2010.

[161] Thonnagith, P., Pipattanasomporn, P., Niparnan, N., Sudsang, A. New combination of programmable force fields for fast planar part manipulation with guaranteed unique configuration, in *Proc. IEEE ROBIO*, 2197-2202, 2009.

[162] Trinkle, J. C.; Farahat, A. O., Stiller, P. F., Second-order stability cells of a frictionless rigid body grasped by rigid fingers, *Proc. IEEE ICRA*, 2815-2821, 1994.

[163] Udhayakumar S., P.V. Mohanram, P. Keerthi Anand, R. Srinivasan, 2013, Determining the most probable natural resting orientation of sector shaped parts *Assembly Autom*. 33, 29 – 37.

[164] Uhrin A. V., Slade C. L., Holmquist, J. G., 2005, Self Righting in the Free-Living Coral Manicina areolata (Cnidaria: Scleractinia): Morphological Constraints. *Caribbean J. Sci*. 41, 277-282.

[165] Van Oosterom A., and J. Strackee, 1983, The solid angle of a plane triangle. *IEEE Trans. Biomed. Eng.*, BME-30, 125-126.

[166] Várkonyi P. L. , D. Gontier, and J. W. Burdick, Stabilization of rigid bodies with frictional supports against dynamic perturbations, in *Proc. IEEE INES*, 281–286, 2011.

[167] Várkonyi P. L., 2009, Floating body problems in two dimensions. *Studies in Applied Mathematics* 122, 195-218.

[168] Várkonyi P.L., The secret of gambling with irregular dice: estimating the face statistics of polyhedra, *extended abstract at the European Workshop on Comp. Geom. (EuroCG)*, Ein-Gedi, Israel, March 3-5, 2014.

[169] Várkonyi, P. L., 2013, Neutrally floating objects of density 1/2 in three dimensions. *Studies in Applied Mathematics* 130, 295-315.

[170] Várkonyi, P. L., Domokos, G., 2006, Static equilibria of rigid bodies: dice, pebbles and the Poincaré-Hopf Theorem *J. Nonlinear Sci*. 16, 255-281.

[171] Várkonyi, P. L., Gontier, D., and Burdick, J. W., On the Lyapunov stability of quasistatic planar biped robots, *Proc. IEEE ICRA*, 63-70., 2012.

[172] Várkonyi, P. L., 2016, Sensorless part feeding with round cages in two and three dimensions. *Robotics and Automation Letters* 1, 724–731.

[173] Várkonyi, P.L., Domokos, G., 2006, Mono-monostatic bodies: the answer to Arnold's question. *Math. Intelligencer* 28(4), 34-38.

[174] Várkonyi, P. L., Or, Y., 2016, Lyapunov stability of a rigid body with two frictional contacts. arXiv preprint arXiv:1603.09672.

[175] Várkonyi, P. L., 2015, On the Stability of Rigid Multibody Systems With Applications to Robotic Grasping and Locomotion. *ASME J. Mechanisms and Robotics* 7, 041012.

[176] Várkonyi, P. L., 2014, Estimating part pose statistics with application to industrial parts feeding and shape design: new metrics, algorithms, simulation experiments and datasets. *IEEE Trans. Aut. Sci. Eng*. 11, 658-667.

[177] Várkonyi P. L., 2016, Dynamics of mechanical systems with two sliding contacts: new facets of Painlevé's paradox, *Archive of Applied Mechanics*, in press.

[178] Domokos, G., Sipos, A., Szabó, T., & Várkonyi, P., 2010, Pebbles, shapes, and equilibria. *Mathematical Geosciences* 42, 29-47.

[179] Vose, T. H., Umbanhowar, P. and Lynch, K. M., 2012, Sliding manipulation of rigid bodies on a controlled 6-DoF plate, *Int. J. Robot. Res*. 31, 819-838.

[180] Vukobratovic M. , A. A. Frank, and D. Juricic, 1970, On the stability of biped locomotion, *IEEE Trans. Biomed. Eng.*, BME-17, 25 – 36.

[181] Wassersug R., Izumi-Kurotani, A., 1992, The behavioral reactions of a snake and a turtle to abrupt decreases in gravity. *Zoolog. Sci*. 10, 505-509.

[182] Wegner F, Floating Bodies of Equilibrium in 2D, the Tire Track Problem and Electrons in a Parabolic Magnetic Field. arXiv preprint arXiv:physics/0701241v3, 2007.

[183] Wegner F., Floating Bodies of Equilibrium in Three Dimensions. The central symmetric case. arXiv preprint arXiv:0803.1043, 2008.

[184] Wegner F., Floating bodies of equilibrium at density 1/2 in arbitrary dimensions. arXiv preprint arXiv:0902.3538, 2009.

[185] Wegner F., 2003, Floating Bodies of Equilibrium. *Studies in Applied Mathematics* 111, 167-183.

[186] Welzl, E., Smallest enclosing disks (balls and ellipsoids), in *New Results and New Trends in Computer Science, Lecture Notes in Computer Science 555*, Maurer, H., Ed., Springer-Verlag, pp. 359–370, 1991.

[187] Wiegley J., A. Rao, and K. Goldberg, Computing a statistical distribu-tion of stable poses for a polyhedron, in *Proc. 30th Annu. Allerton Conf. Commun., Contr., Comput., Univ. Illinois, Urbana-Champaign*, Oct. 1992.

[188] Wiegley J., K. Goldberg, M. Peshkin, and M. Brokowski, 1997, A complete algorithm for designing passive fences to orient parts, *Assembly Autom*. 17, 129-136.

[189] Wiesner, C. S., Iben, C., 2003, Influence of environmental humidity and dietary protein on pyramidal growth of

carapaces in African spurred tortoises (Geochelone sulcata) *J. Anim. Phys. and Anim. Nutr.* 87, 66.

[190] Wikipedia/Dice: http://en.wikipedia.org/wiki/Dice

[191] Willemsen, R. E., Hailey, A., 2003, Sexual dimorphism of body size and shell shape in European tortoises *J. Zool., Lond.* 260, 353–365.

[192] Yamada, T., and Yamamoto, H., Grasp stability analysis of multiple objects including contact surface geometry in 3D, *Proc. IEEE ICMA*, 36-43, 2013.

[193] Zhang J., K. H. Johansson, J. Lygeros, and S. Sastry, 2001, Zeno hybrid systems, *Int. J. Robust Nonlin. Control* 11, 435-451.

[194] Zhang M. T. , K. Goldberg, G. Smith, R. P. Beretty, and M. Overmars, 2001, Pin design for part feeding, *Robotica* 19, 695-702.

[195] Zumel, N. B., Erdmann, M. A., Nonprehensile manipulation for orienting parts in the plane, *Proc. IEEE ICRA*, 2433-2439, 1997.